PMR 5251

Assessment of Mechanical Behavior of Materials using Machine Learning Approach

Profa.Dra. Izabel Fernanda Machado and

Profa. Dra. Larissa Driemeier

Profa. Izabel Machado - machadoi@usp.br

Profa. Larissa Driemeier - driemeie@usp.br

Multiscale modeling

Multiscale modeling refers to a style of modeling in which multiple models at different scales are used simultaneously to describe a system.

The different models usually focus on different scales of resolution.

They sometimes originate from physical laws of different nature, for example, one from continuum mechanics and one from molecular dynamics. In this case, one speaks of multi-physics modeling even though the terminology might not be fully accurate.

http://www.scholarpedia.org/article/Multiscale_modeling

Multiscale modeling

The need for multiscale modeling comes usually from the fact that the available macroscale models are not accurate enough, and the microscale models are not efficient enough and/or offer too much information.

By combining both viewpoints, one hopes to arrive at a reasonable compromise between accuracy and efficiency.

http://www.scholarpedia.org/article/Multiscale_modeling

Multiscale modeling

The subject of multiscale modeling consists of three closely related components:
multiscale analysis,
multiscale models and
multiscale algorithms.

Multiscale analysis tools allow us to understand the relation between models at different scales of resolutions.

Multiscale models allow us to formulate models that couple together models at different scales.

Multiscale algorithms allow us to use multiscale ideas to design computational algorithms.

http://www.scholarpedia.org/article/Multiscale_modeling

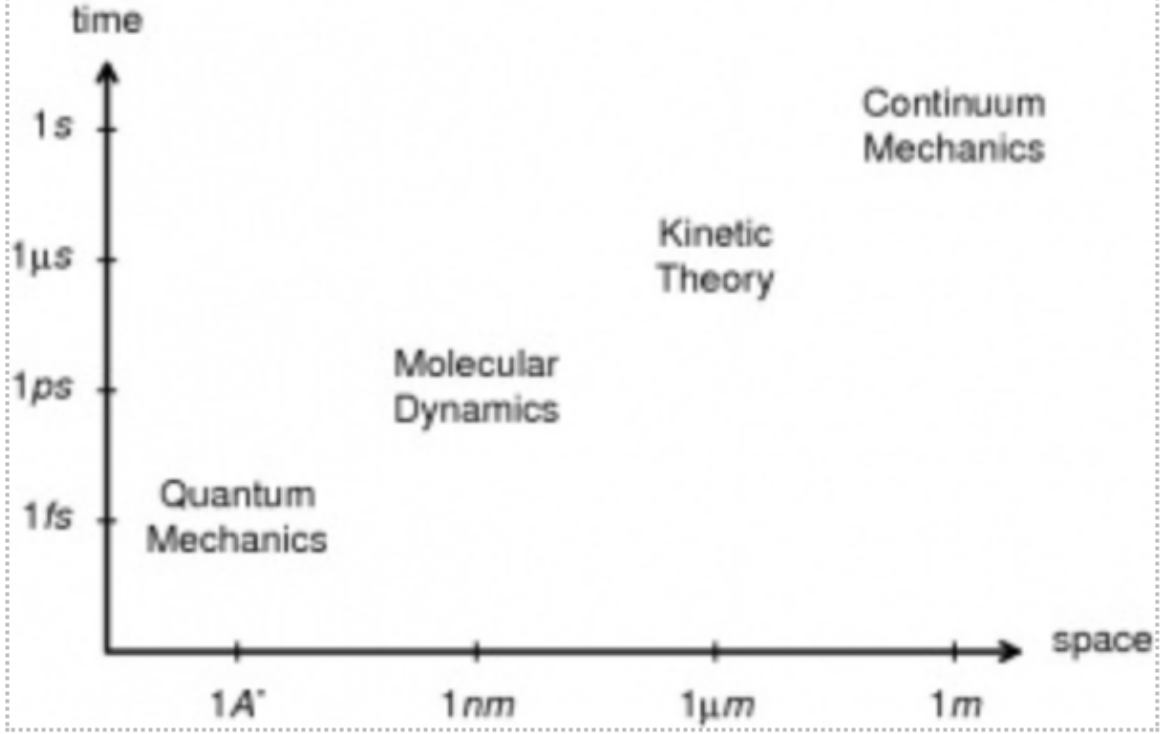

Figure 1: Illustration of the multi-physics hierarchy. It should be noted that this diagram is slightly misleading: Quantum mechanics is valid not just at the microscale, it also applies at the macroscale -- only that much simpler models are already quite sufficient at the macroscale.

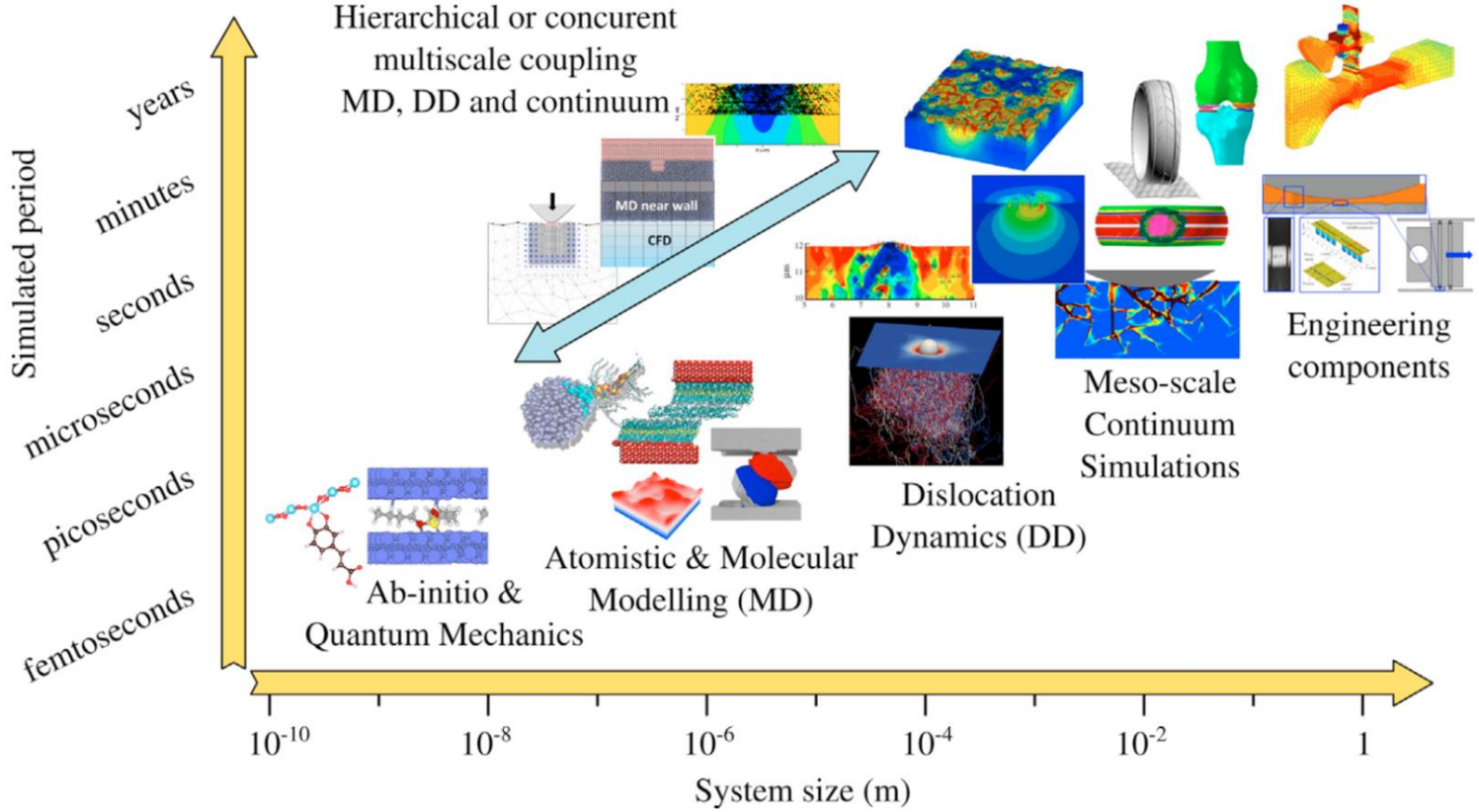

Fig. 1. A time-vs. length-scales map of models developed in tribology highlighting the intrinsic link between multiscale/physics that needs to be captured to provide predictive tools for engineering applications. Illustrations from simulations performed by the authors.

https://doi.org/10.1016/j.triboint.2018.02.005

Wear and friction

da Vinci's three notable observations that preceded the development of the laws of friction were uncovered: **(1) Friction is independent of apparent contact area, (2) the resistance of friction is directly proportional to applied load, and (3) friction has a consistent value of μ= 0.25.**

Experiments, performed roughly 500 years later, reproduced Leonardo da Vinci's findings of friction coefficients with wood of l = 0.25, but only under condi- tions of roughly cut and brusquely squared samples of dry wood that were handled and sullied by hand in a fashion typical of wood working but inconsistent with the modern laboratory practice.

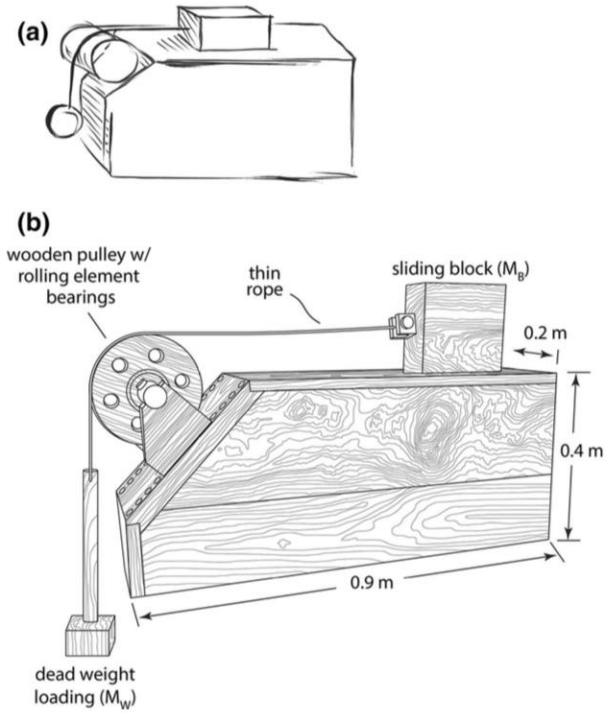

Fig. 1 a A digital tracing of Leonardo da Vinci's experimental schematic taken from an illuminated digital photograph by the British Library of Arundel 263 from Leonardo da Vinci's *Codex Arundel* (dating between 1480 and 1518), f. 40 V as displayed in bifolium with f. 41, but reproduced here without accompanying notes and diagrams [12]. **b** A detailed illustration of the wooden recreation of the experiment described in the *Codex Arundel*, including notes on the hardware, and the associated dimensions. The entire assembly was made from wood (Maple for all planar surfaces), with the exception of a pair of rolling element bearings and a precision steel shaft that were inserted and hidden within the wooden pulley assembly. See Online Resource 1 for more details

Tribol Lett (2014) 56:509–515 DOI 10.1007/s11249-014-0428-7

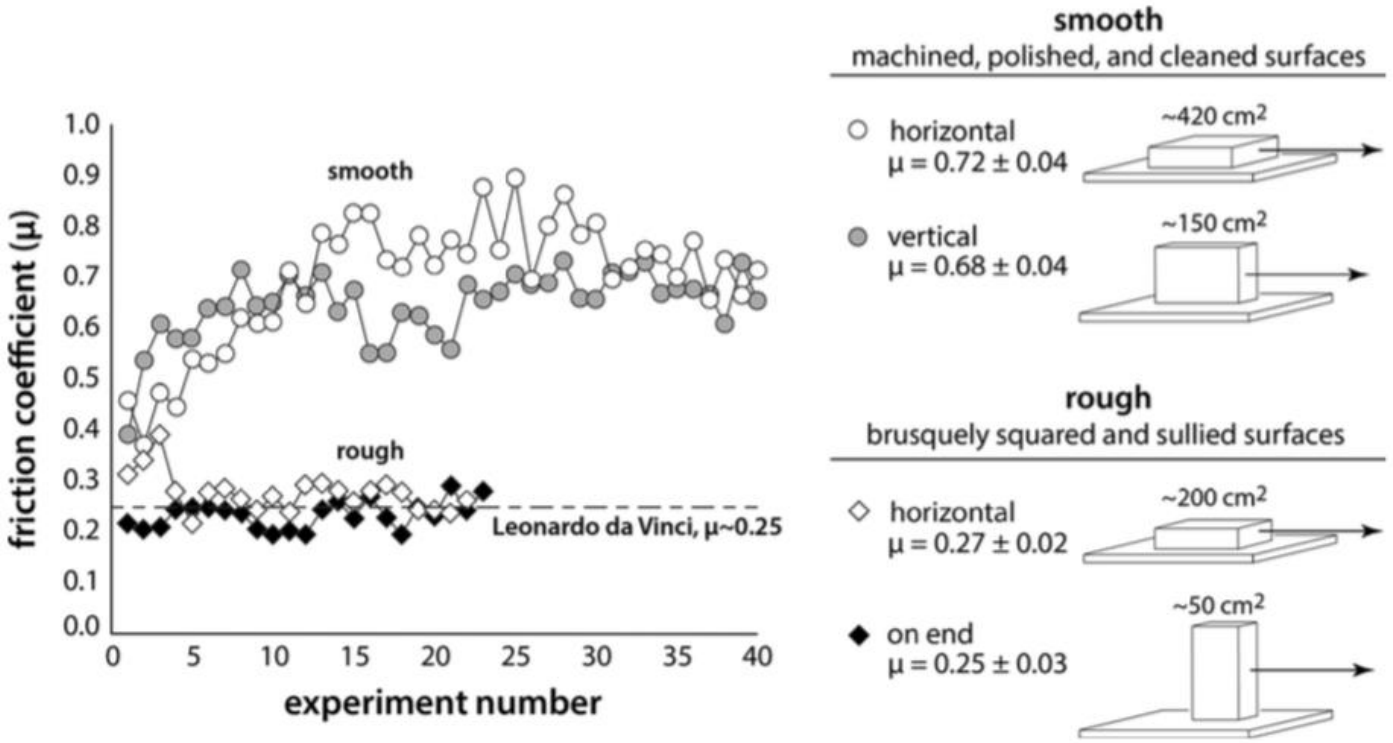

Fig. 2 Experiments performed on the block of African Padauk in both a horizontal (*open circle*) and vertical (*gray circle*) configuration with the sliding direction aligned with the grain. Additional experiments were performed in the horizontal (*open diamond*) and on end (*black diamond*) configuration using a block of roughly squared Bubinga wood ($M_B \sim 2.1$ kg) with sullied surfaces in the sense that the sliding surfaces were not polished, sanded, or cleaned with anything other than a casual wipe of the hand. See Online Resources 2 and 5 for more details

Tribol Lett (2014) 56:509–515 DOI 10.1007/s11249-014-0428-7

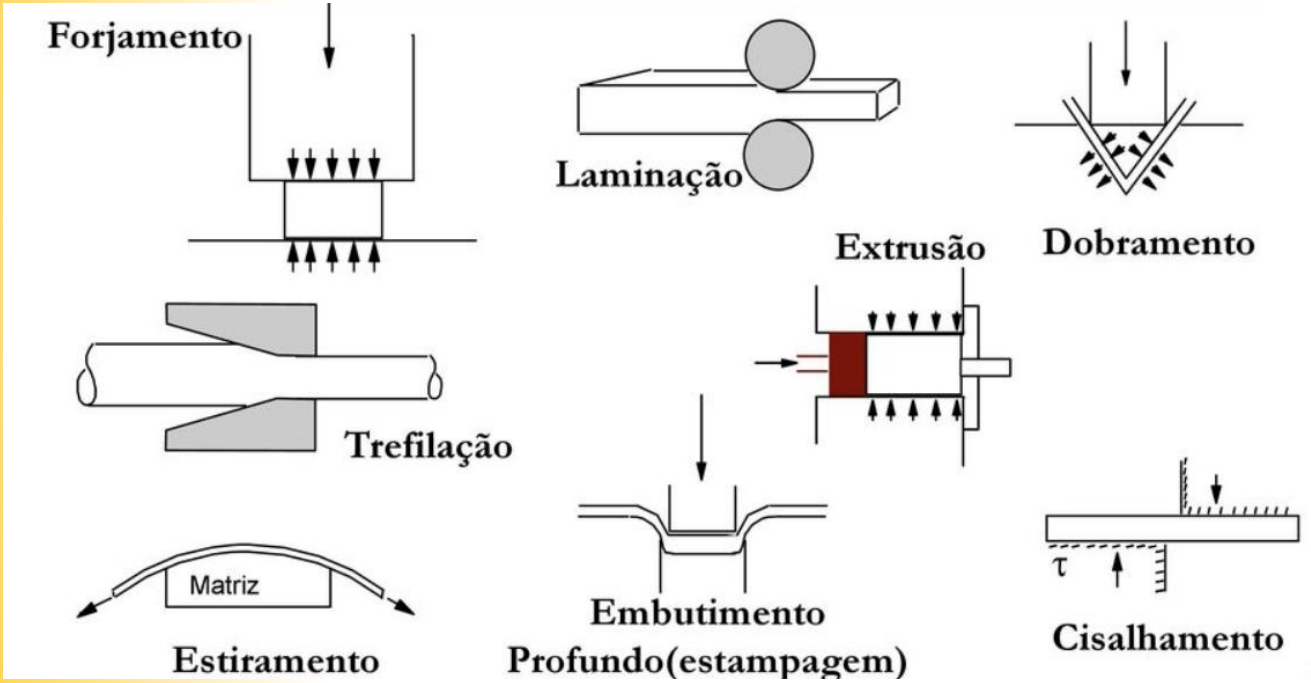
Forjamento
Laminação
Extrusão
Dobramento
Trefilação
Matriz
Estiramento
Embutimento
Profundo(estampagem)
τ
Cisalhamento

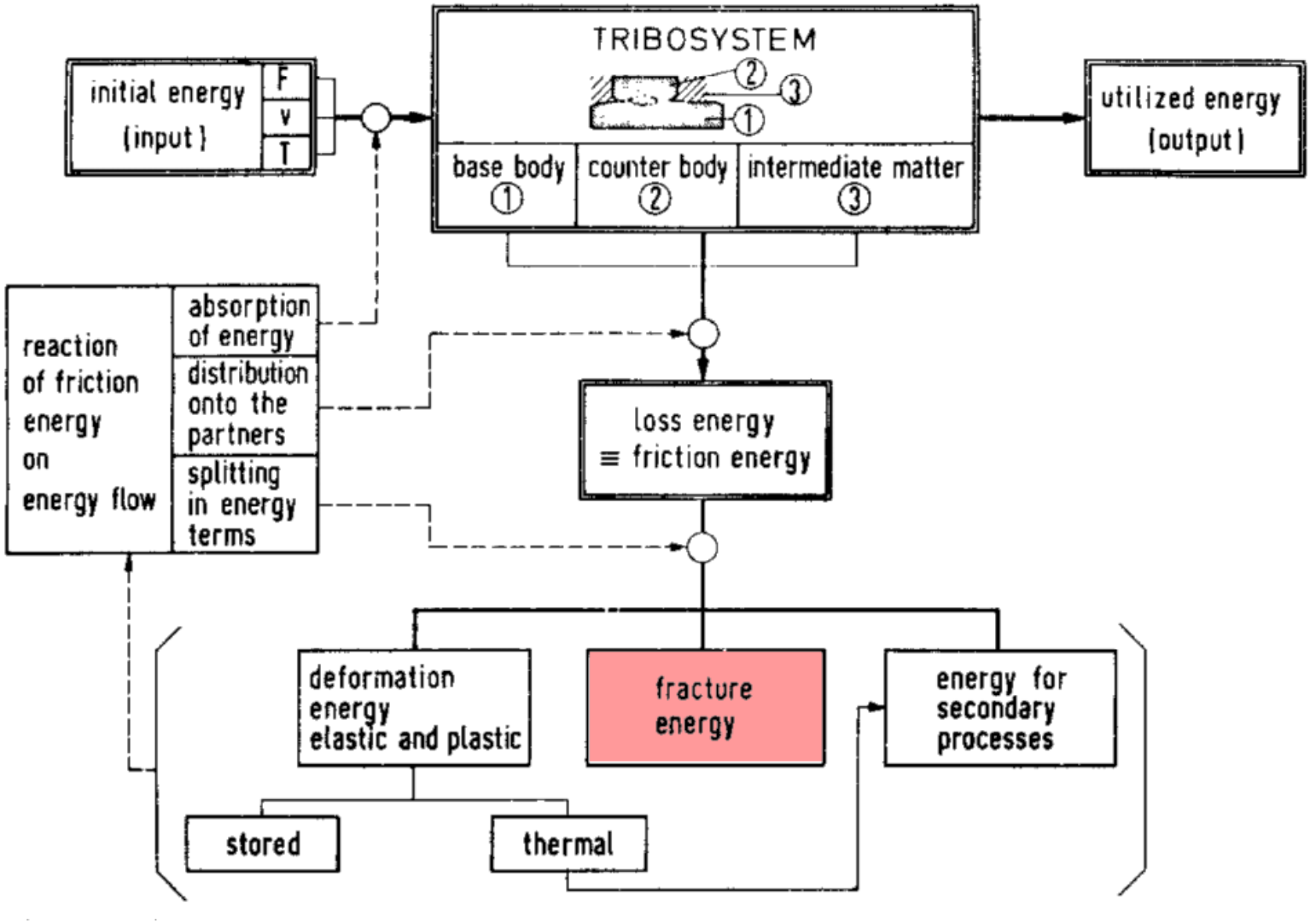

(UETZ; FÖHL, 1978)

Analytical methods

Contact mechanics

Starting from the mechanics of nominally smooth contact problems, the Hertzian theory, which solves the problem of two non-conformal elastic bodies being subjected to frictionless contact

$$\frac{1}{E^*} = \frac{(1-\nu_1^2)}{E_1} + \frac{(1-\nu_2^2)}{E_2} \qquad (2.16)$$

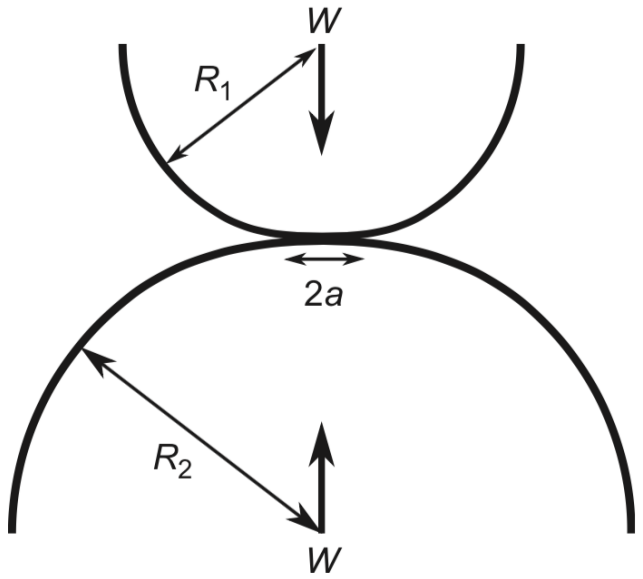

Fig. 2.8 Elastic deformation of a Hertzian point contact between two spherical surfaces under normal load W to form a contact circle with radius a

https://doi.org/10.1016/j.triboint.2018.02.005

Contact

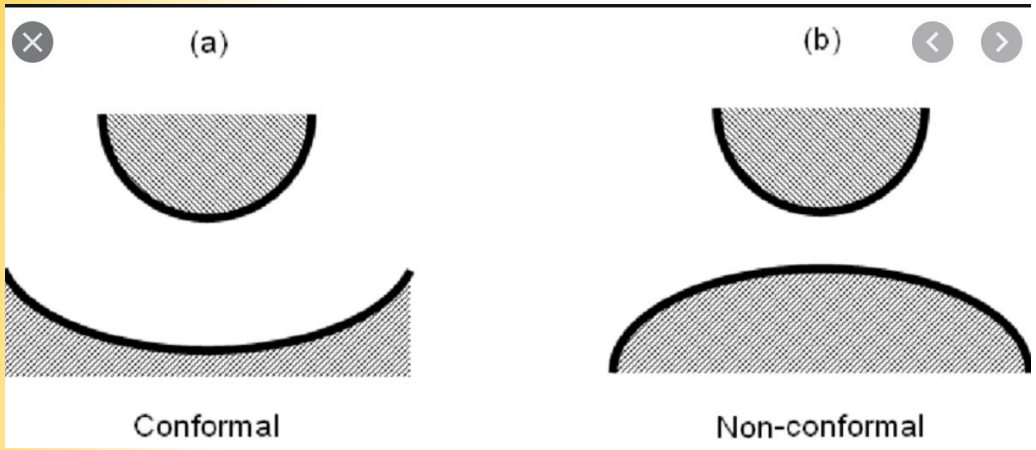
(a)
(b)
Conformal
Non-conformal

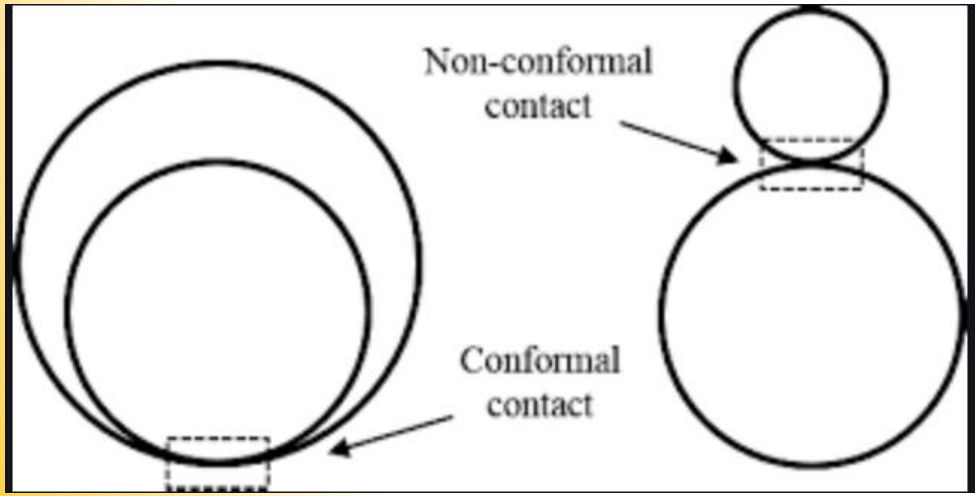
Non-conformal contact
Conformal contact

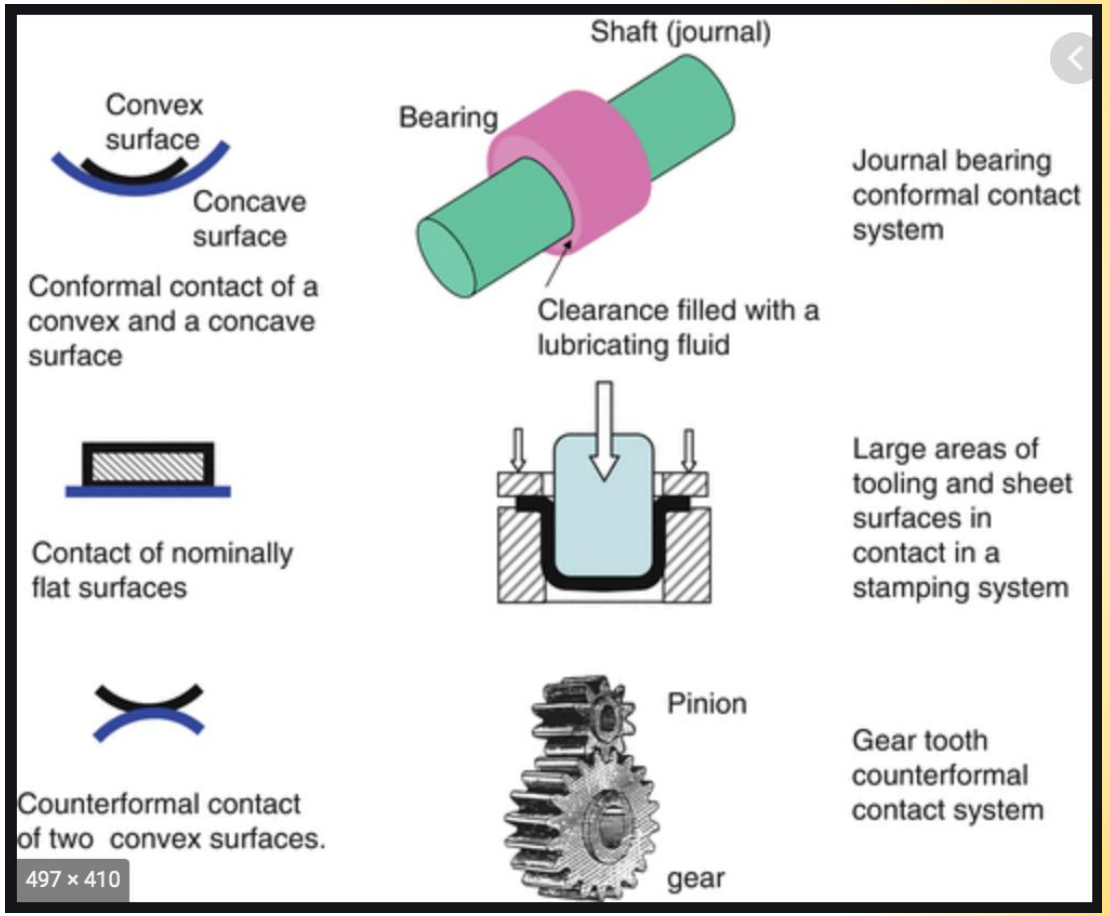
Shaft (journal)
Convex surface
Concave surface
Bearing
Journal bearing conformal contact system
Conformal contact of a convex and a concave surface
Clearance filled with a lubricating fluid
Contact of nominally flat surfaces
Large areas of tooling and sheet surfaces in contact in a stamping system
Pinion
Gear tooth counterformal contact system
Counterformal contact of two convex surfaces.
gear
497 × 410

Figura 2.2 - Tipos de movimentos relativos entre dois corpos. (a) Deslizamento; (b) Rolamento; (c) Giro

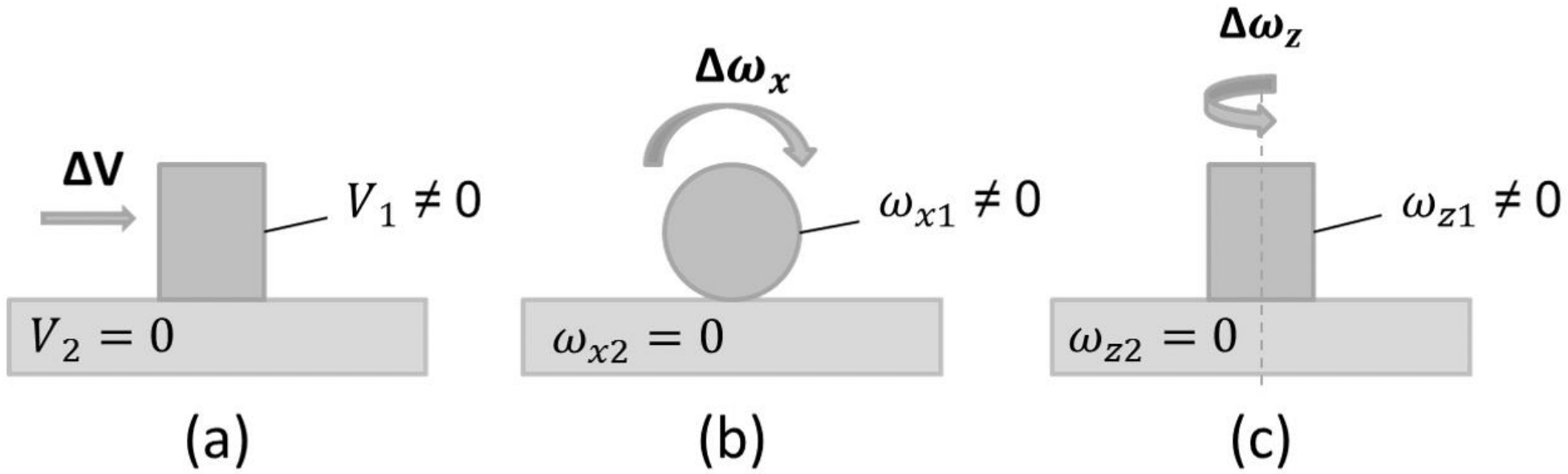

Fonte: O autor

https://doi.org/10.1016/j.triboint.2018.02.005

Figura 2.3 - Direções dos movimentos relativos para um par engrenado. (a) Início do engrenamento; (b) Engrenamento sob diâmetro primitivo; (c) Fim do engrenamento

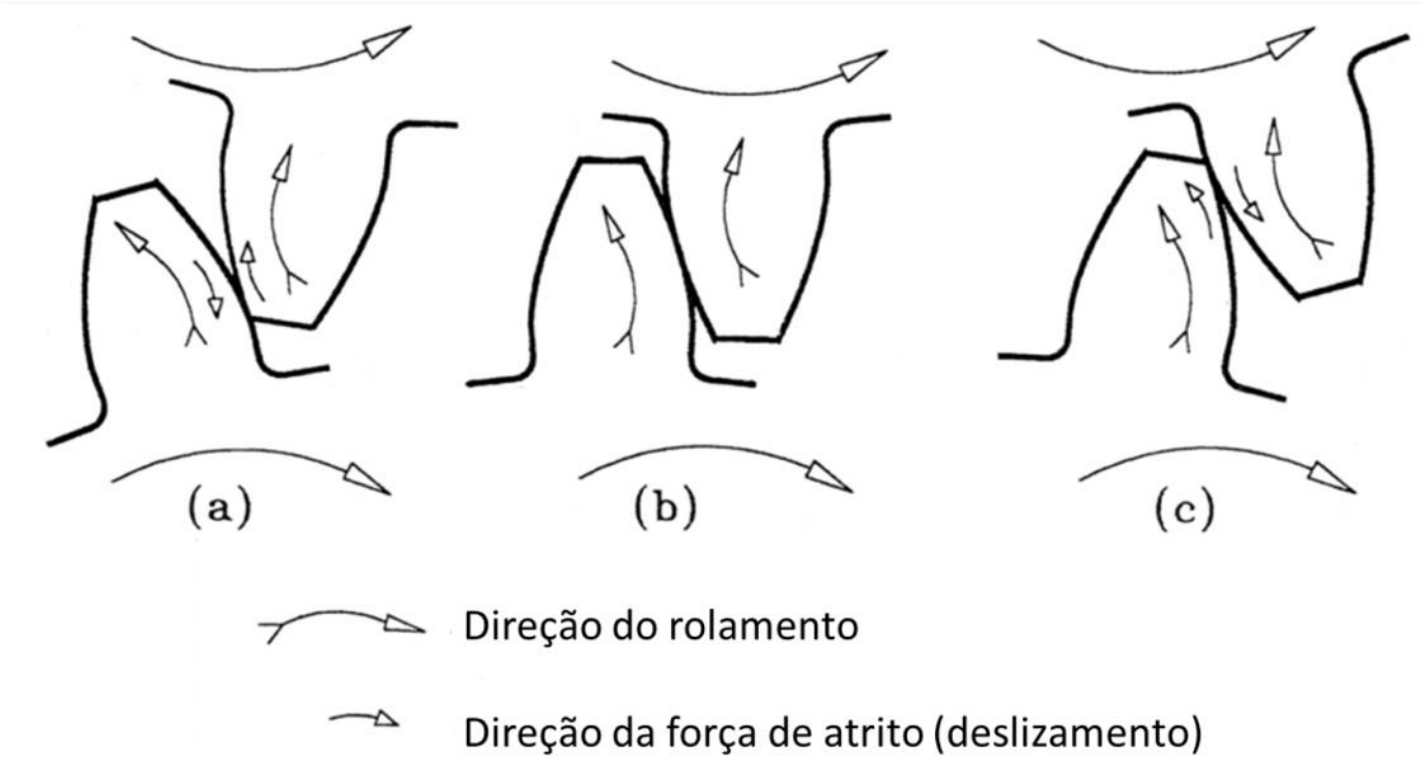

Fonte: Walton e Goodwin (1998)

Statistical theories of multiple asperity contact

Surface topography and surfaces in contact 27

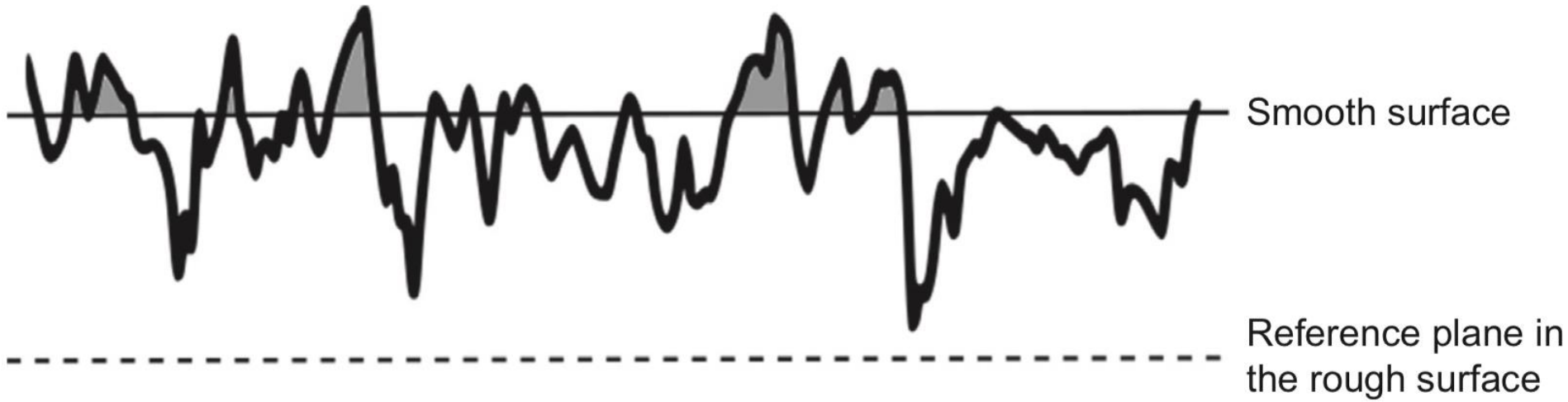

Fig. 2.10 Model for contact between a rough surface and a smooth rigid plane illustrating the assumptions made by Greenwood and Williamson

Statistical theories of multiple asperity contact

The GW and subsequent multi-asperity models are based on the following assumptions: 1) the effective rough surface (a superposition of two rough profiles or surfaces) can be represented by an ensemble of asperities (surface summits), characterized by the vertical coordinate of the tip and its curvature(s); 2) these characteristics are known in the statistical sense, for example, via the probability density of the asperities' vertical position; 3) the relation between penetration, force and the contact area follows the Hertzian theory of contact; 4) the asperities of the effective rough surfaces coming into contact are separated in the plane by distances at which their mutual influence can be neglected. In the original GW, all asperities are approximated as parabolic with the same curvature radius, and an arbi- trary height distribution is assumed, contrary to numerous references in the literature erroneously stating that the GW model is based on Gaussian distribution of asperity heights: both Gaussian and exponential tails are
considered in the original paper.

https://doi.org/10.1016/j.triboint.2018.02.005

The theory of Greenwood and Williamson was derived for purely elastic contact, but it does allow the onset of plastic flow at asperities to be predicted. It is found that the proportion of asperity contacts at which plastic flow has occurred depends on the value of a plasticity index, ψ, given by

$$\psi = \frac{E^*}{H}\left(\frac{\sigma^*}{r}\right)^{1/2}$$

where H is the indentation hardness of the softer surface (a measure of the plastic flow stress of the asperities) and $(\sigma^*/r)^{1/2}$ is the standard deviation of the distribution of asperity heights. The quantity is approximately equal to the average slope of the asperities, which can be estimated from profilometric data.

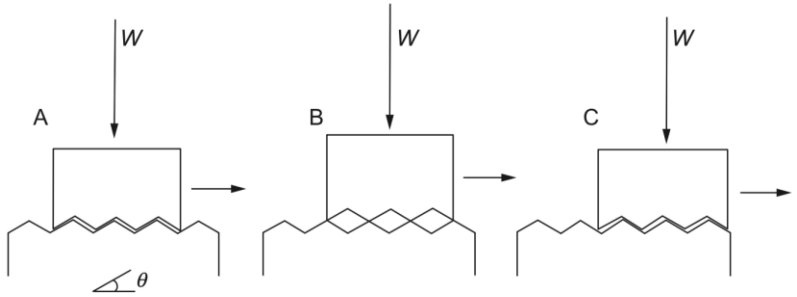

Fig. 3.4 A schematic diagram illustrating the principles behind the Coulomb model for sliding friction. The surface roughness is assumed to have a sawtooth geometry. As sliding occurs from position A to B work is done against the normal load *W*. The normal load then does an equal amount of work as the surfaces move from B to C

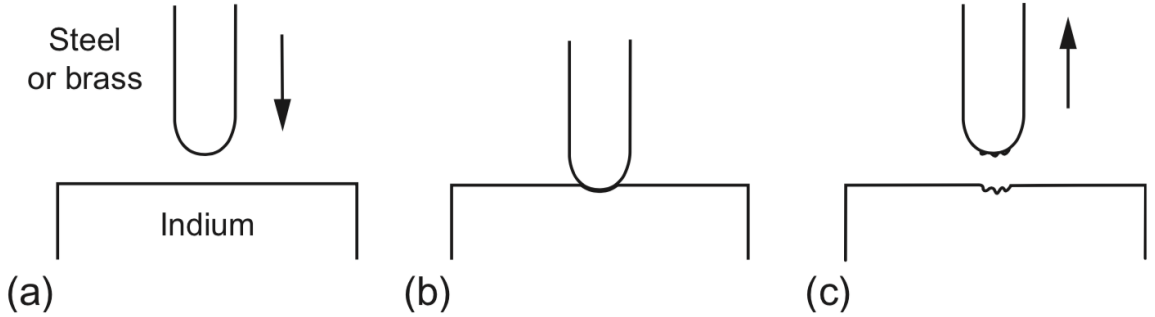

Fig. 3.5 An experiment to illustrate adhesion between metals. A clean steel or brass rod is pressed with a slight twisting motion on to the freshly-scraped surface of an indium block. Appreciable force is needed to detach the rod from the block, and fragments of indium adhere to the steel surface

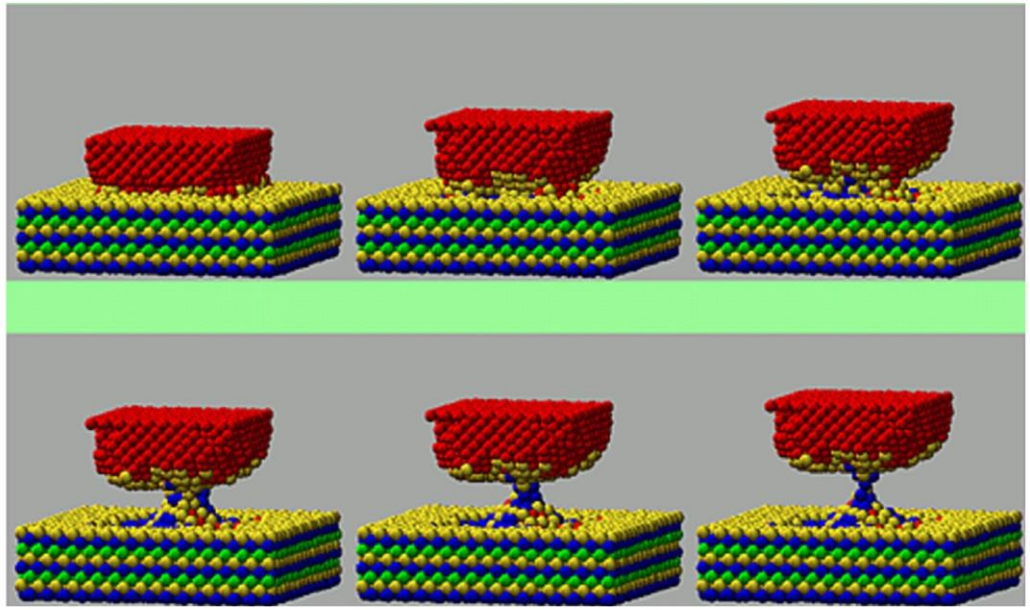

Fig. 3.6 Atomic configurations predicted by theoretical modelling of the contact between a nickel indenter (upper body) and an initially plane gold surface. No consideration is given in the model to adsorbed or reacted oxygen atoms, so that the system modelled corresponds to the contact of atomically clean metals in a perfect vacuum. The images from top left to bottom right show adhesion of gold atoms to the indenter, and progressive formation of a 'neck' of gold atoms drawn out as the indenter is raised from the surface (from Landman, U., Luedtke, W.D., Ringer, E.M., 1992. Wear 153, 3–30)

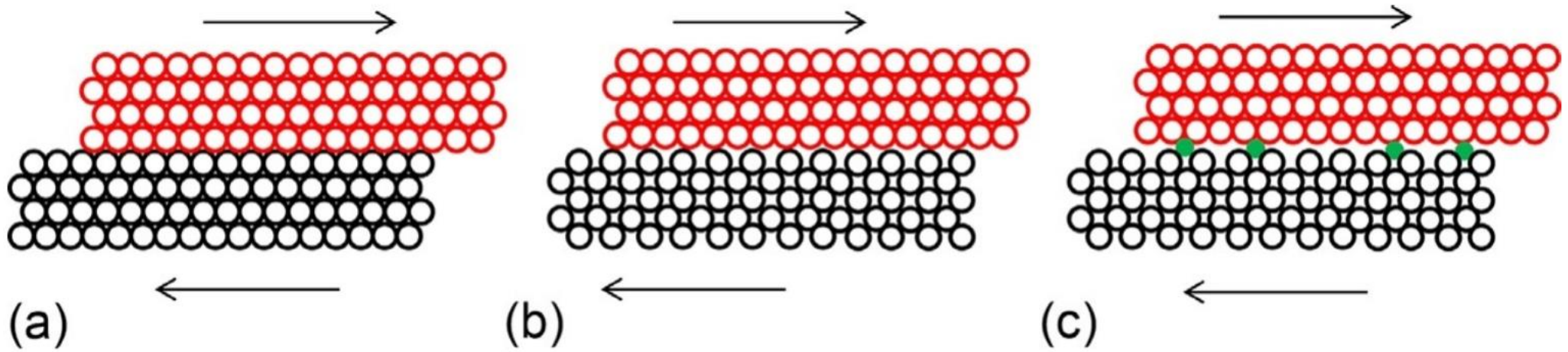

Fig. 3.10 Schematic diagrams showing (a) two crystalline solids sliding over each other with perfect lattice matching (a *commensurate* contact); (b) two crystalline solids with different spacing of surface atoms (an *incommensurate* contact); and (c) an incommensurate contact with contaminant atoms at the interface

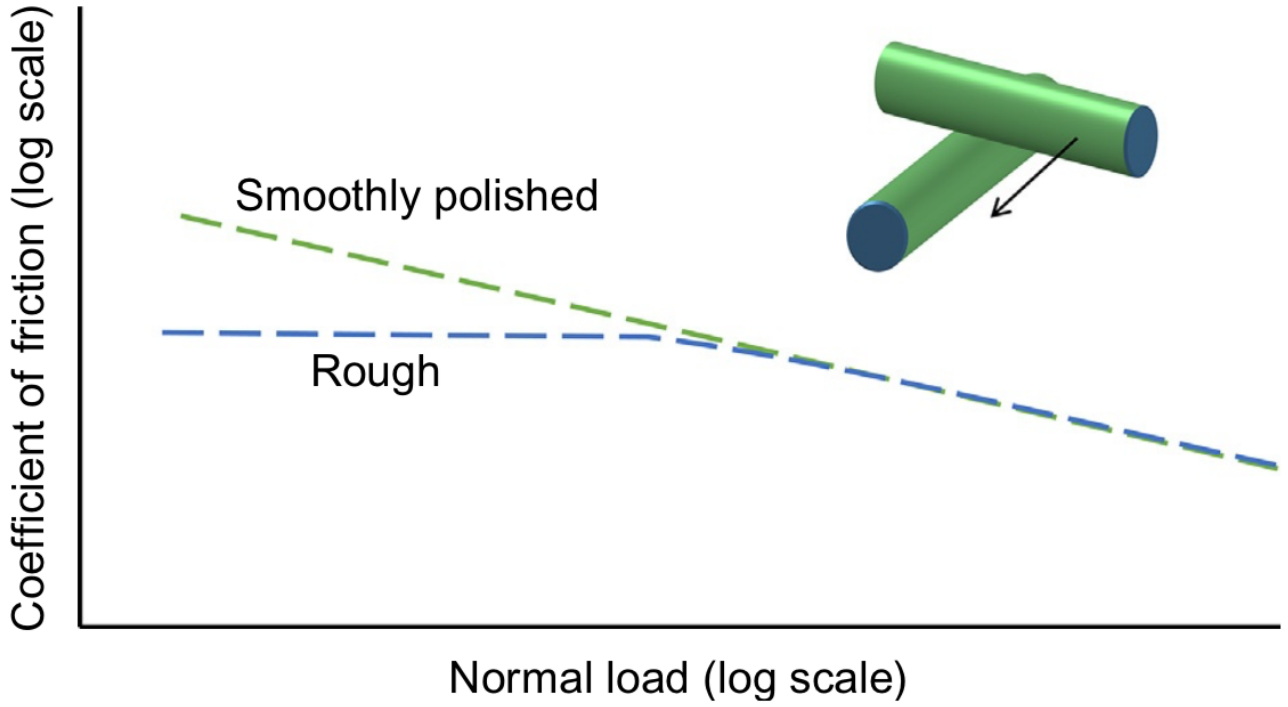

Fig. 3.31 Schematic diagram showing how the coefficient of friction varies with normal load for sliding of crossed cylinders of a glassy polymer with different surface roughness (Sketch showing behaviour reported for PMMA by Archard, J.F., 1957. Proc. Roy. Soc. Lond. A243, 190)

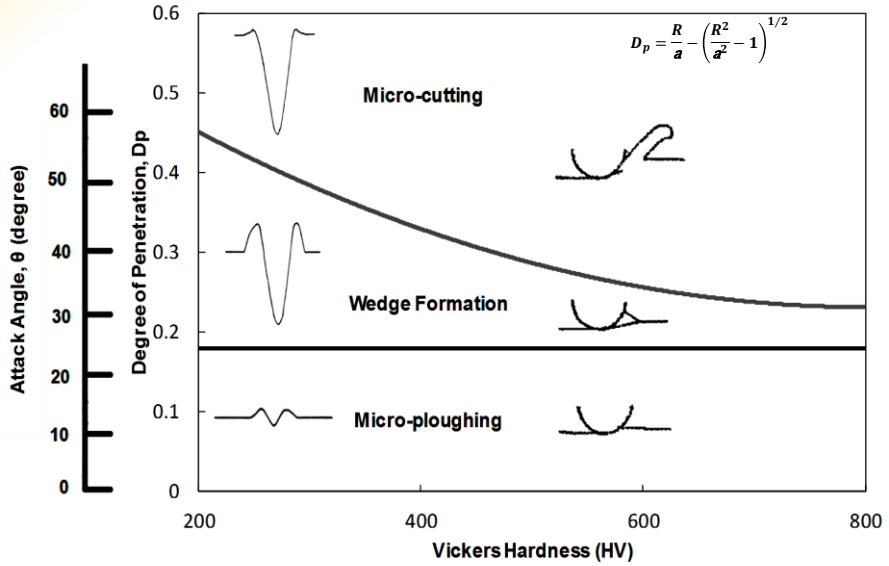

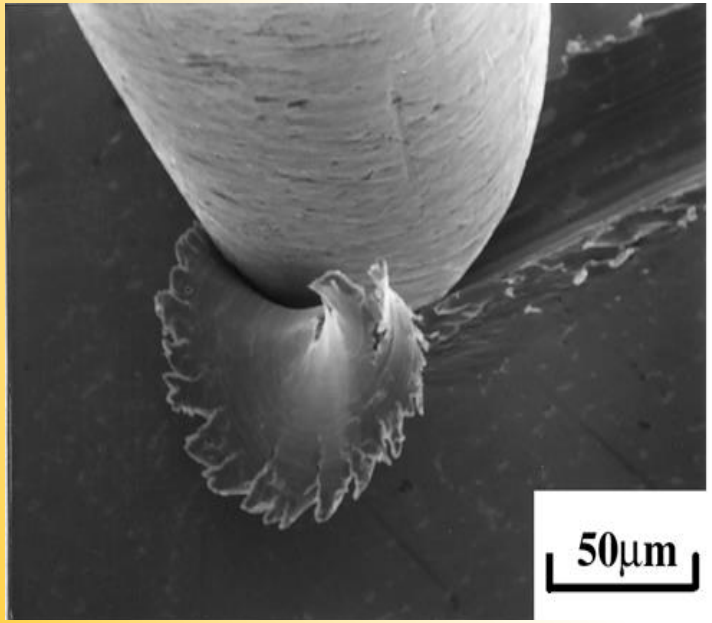

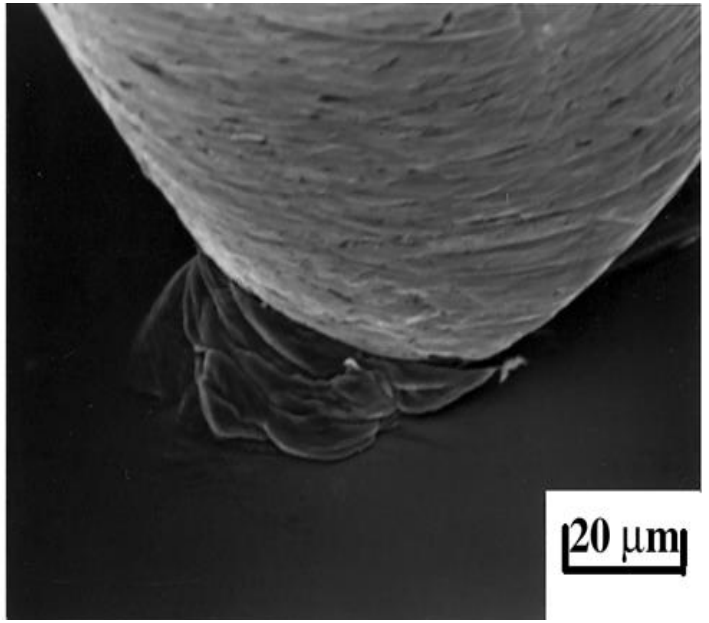

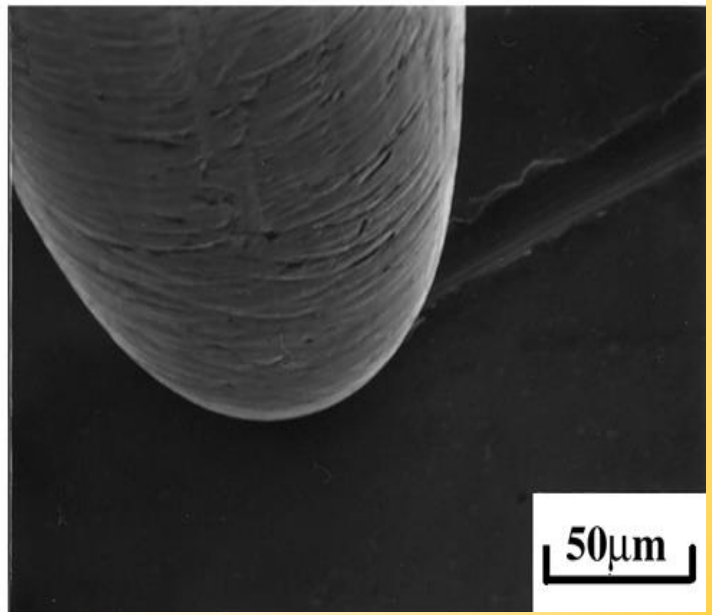

Hokkirigawa; Kato (1988)

Analytical methods

Contact mechanics

Starting from the mechanics of nominally smooth contact problems, the Hertzian theory, which solves the problem of two non-conformal elastic bodies being subjected to frictionless contact

$$\frac{1}{E^*} = \frac{\left(1-\nu_1^2\right)}{E_1} + \frac{\left(1-\nu_2^2\right)}{E_2} \qquad (2.16)$$

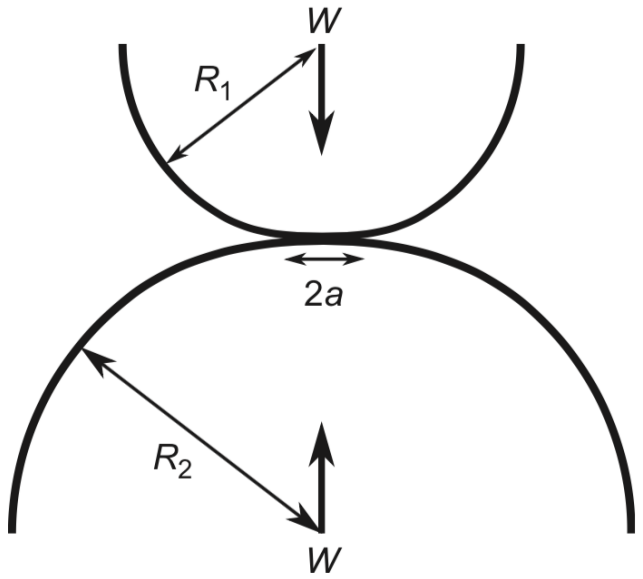

Fig. 2.8 Elastic deformation of a Hertzian point contact between two spherical surfaces under normal load W to form a contact circle with radius a

https://doi.org/10.1016/j.triboint.2018.02.005

Below the surface, tractional loads result in an increase in the value of the maximum shear stress, and a movement of the position of the maximum shear stress off the axis of normal loading and closer to the surface as shown in Fig. 2.9 for a line contact, which compares the stress distributions (a) with normal loading only and (b) with additional traction.

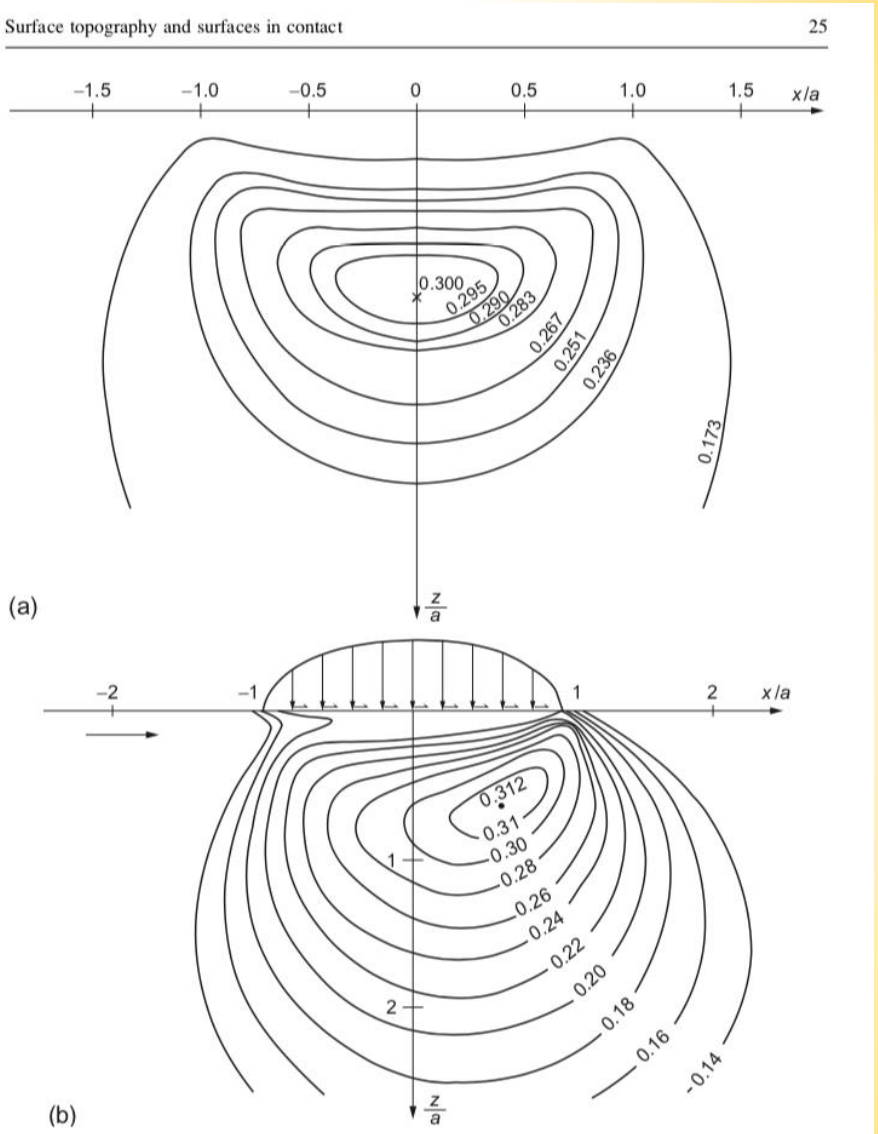

Fig. 2.9 Contours of principal shear stress in Hertzian line contacts: (a) under normal loading alone; and (b) in sliding with a coefficient of friction of 0.2. (after Johnson, K.L., 1985. Contact Mechanics. Cambridge University Press)

Figura 2.7 - Tensão de cisalhamento τ e tensão de cisalhamento ortogonal τ_{zx}, ao longo da profundidade z, para o caso de esfera sobre plano, segundo as eqs. (20) e (30)

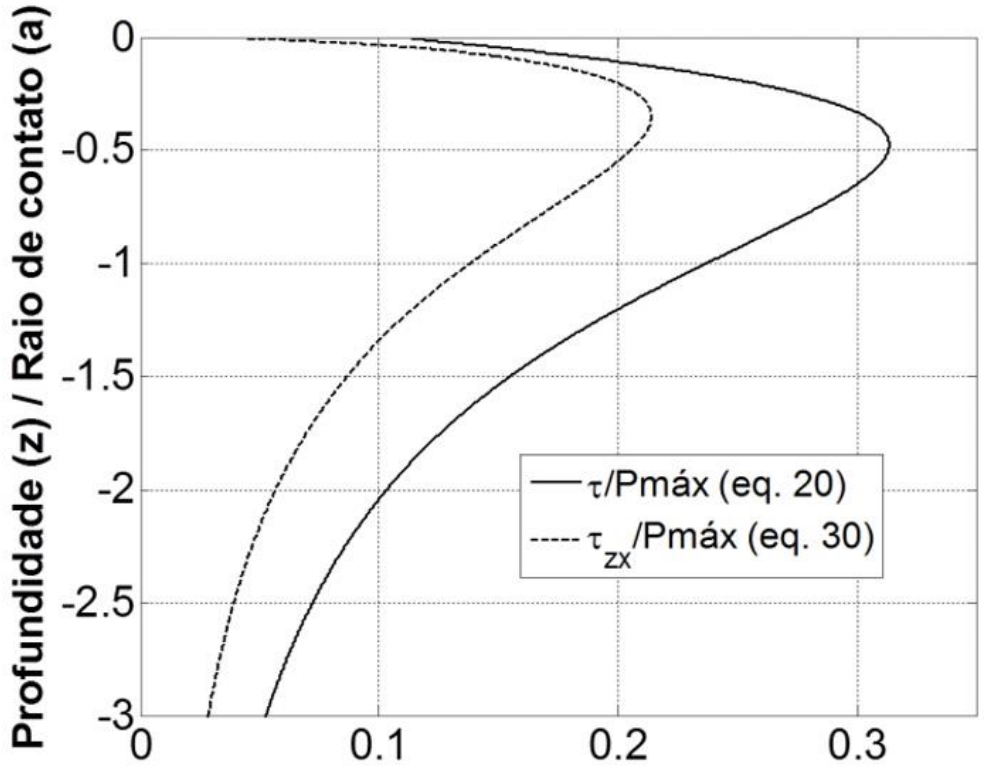

EFFICIENCY and DURABILITY

Local determination of lubrication - Tooth gear

Experimental tests: Mechanical losses due to friction in lubricated contact

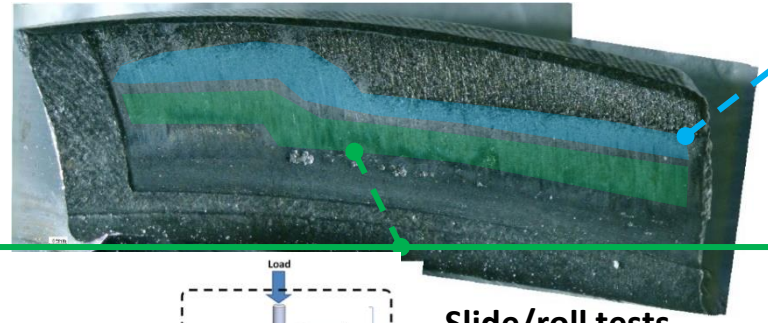

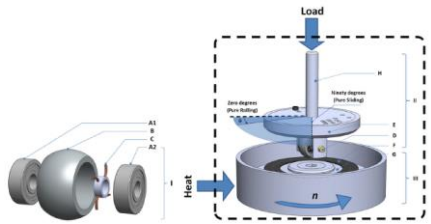

Slide/roll tests

Slide-to-roll apparatus – Friction measurements

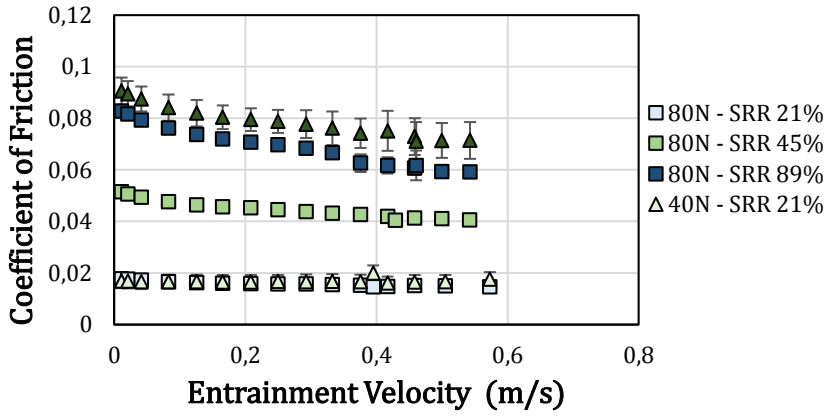

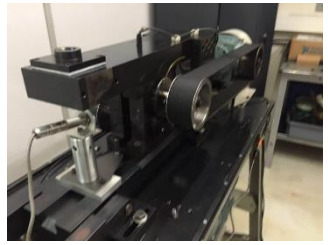

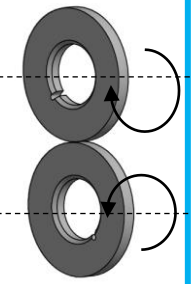

Slide/roll tests

Twin-disc – Surface damage

Good correlation between gear damage and speciments damage

Gear worn surface

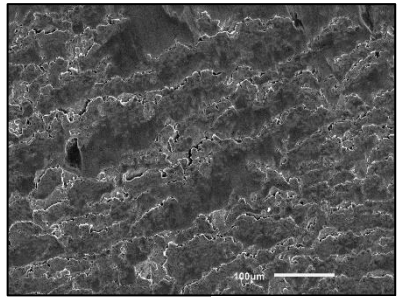

Twin-disc-test 10% SRR

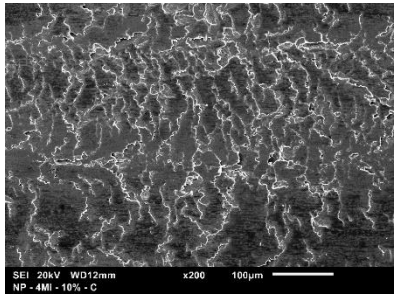

Plastic deformation

Figura 2.20 - Comparação dimensional entre *pitting* e *spalling*; 'a' representa o raio da área circular de contato de Hertz

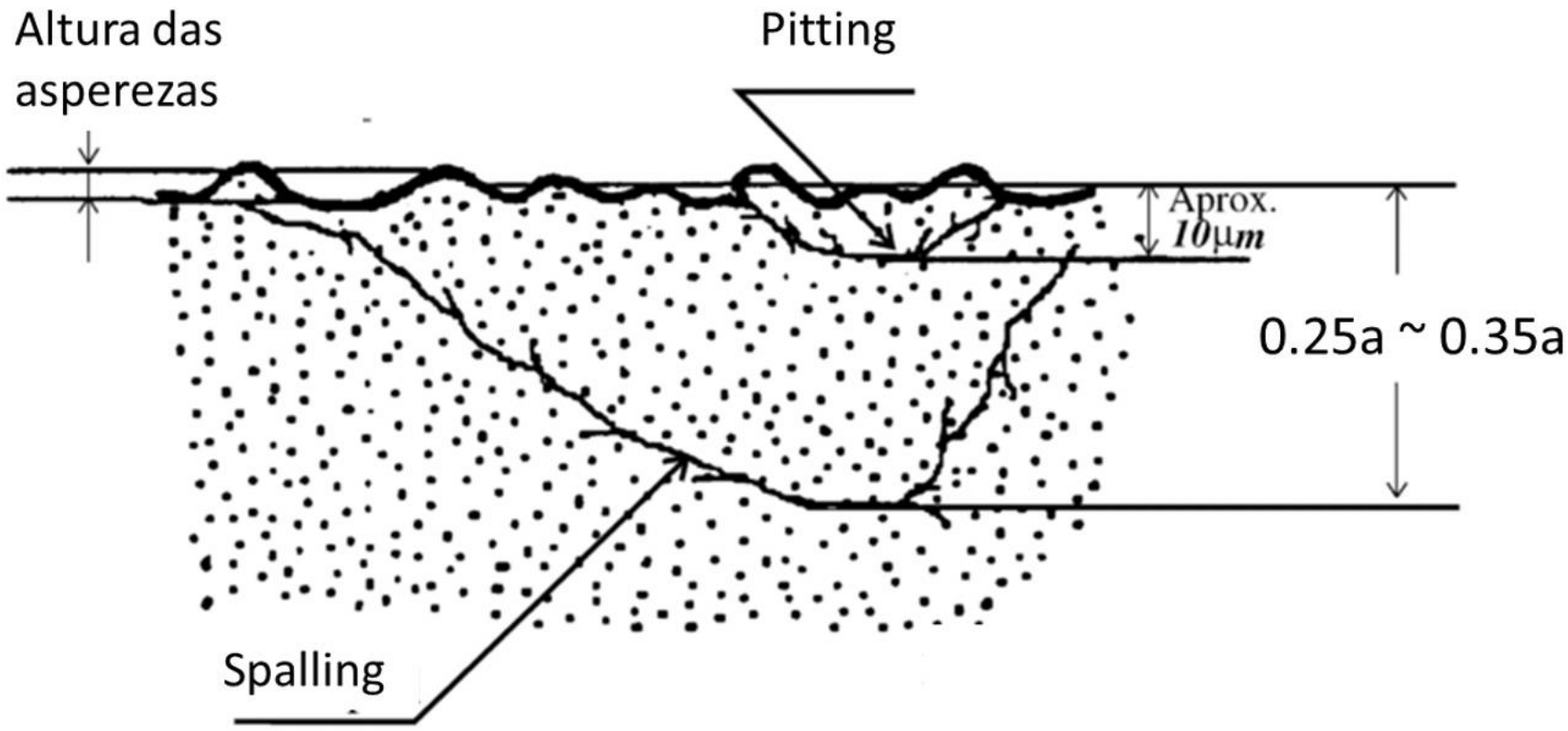

Fonte: Adaptado de Ding e Rieger (2003)

Tabela 2 - Comparação entre as características dos mecanismos de *pitting* e *spalling*

	Região de nucleação da trinca	Causa da nucleação (aumento de τ/Hv)	Principal modo de propagação	Escala da dimensão do desgaste
Pitting	Superfície[1]	Contato entre asperezas[2]	Modo I (tração devido à pressurização do lubrificante)[3]	Asperezas[4]
Spalling	Subsuperfície[1]	Inclusões ou defeitos[2]	Modo II (tensão de cisalhamento)[3]	Posição das máximas tensões cisalhantes[4]

[1] Ding e Rieger (2003); Olver (2005); Santus et al. (2012)
[2] Leng, Chen e Shao (1988b); Olver (2005); Santus et al. (2012)
[3] Ding e Gear (2009); Santus et al. (2012)
[4] Tallian (1999); Ding e Rieger (2003); Santus et al. (2012)

Durability – Wear

Surface damage analysis

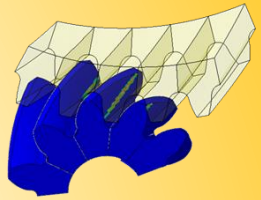

Examples of Gear Wear Results after Back-to-Back (FZG) tests

Scuffing – Sliding Abrasion marks suggesting scuffing failure mode.

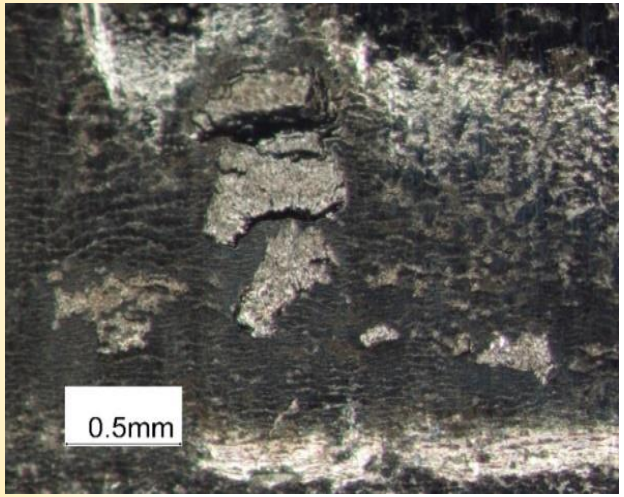

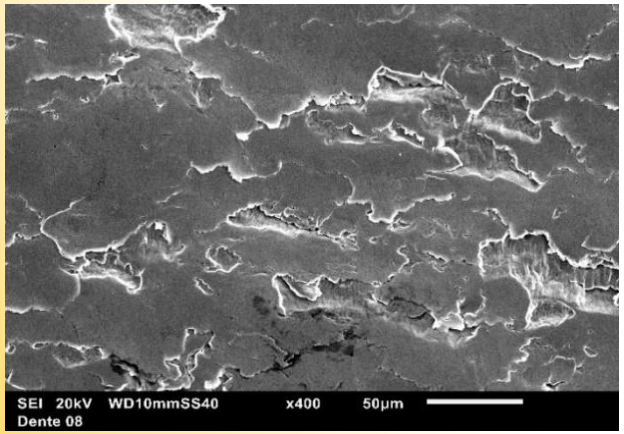

Pitting - 3D profile of detachment on contact region

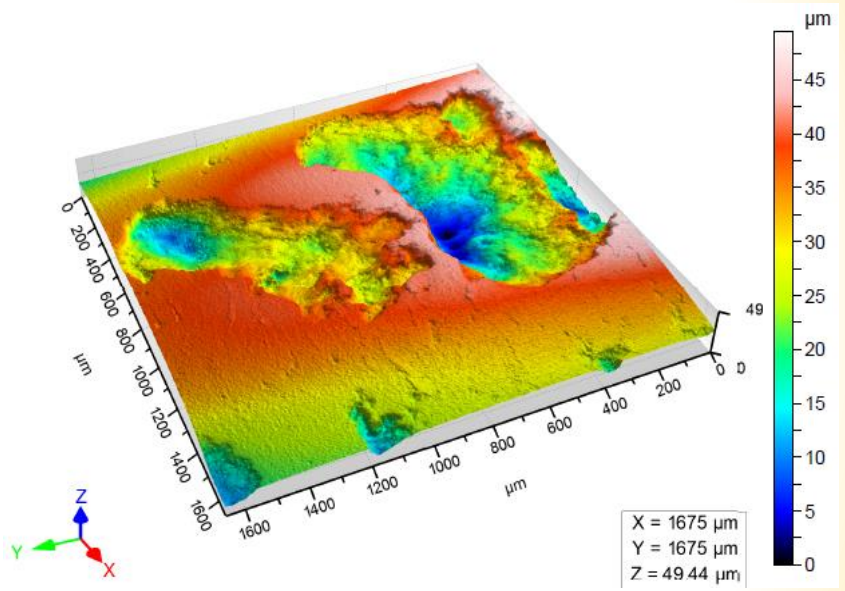

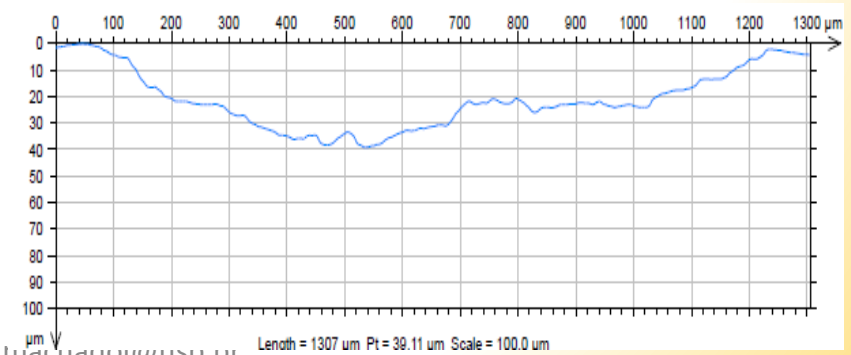

Microstructure

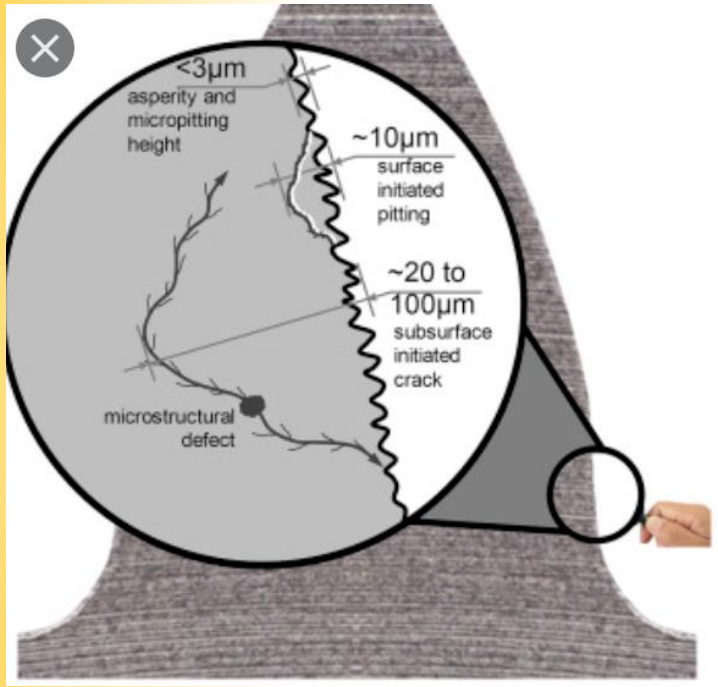

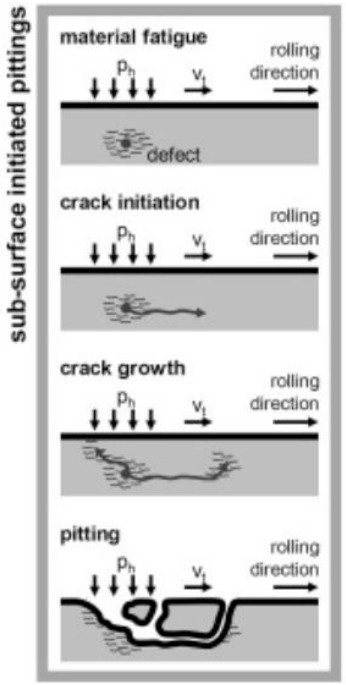

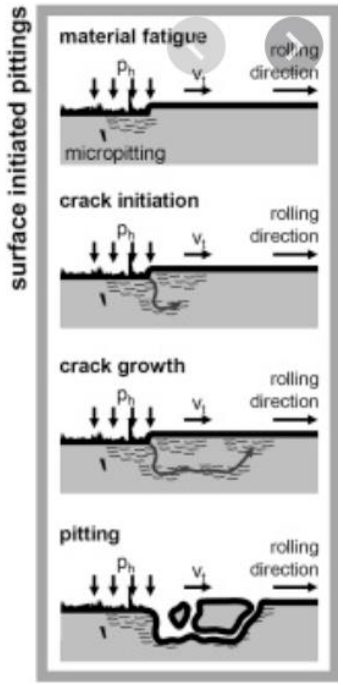

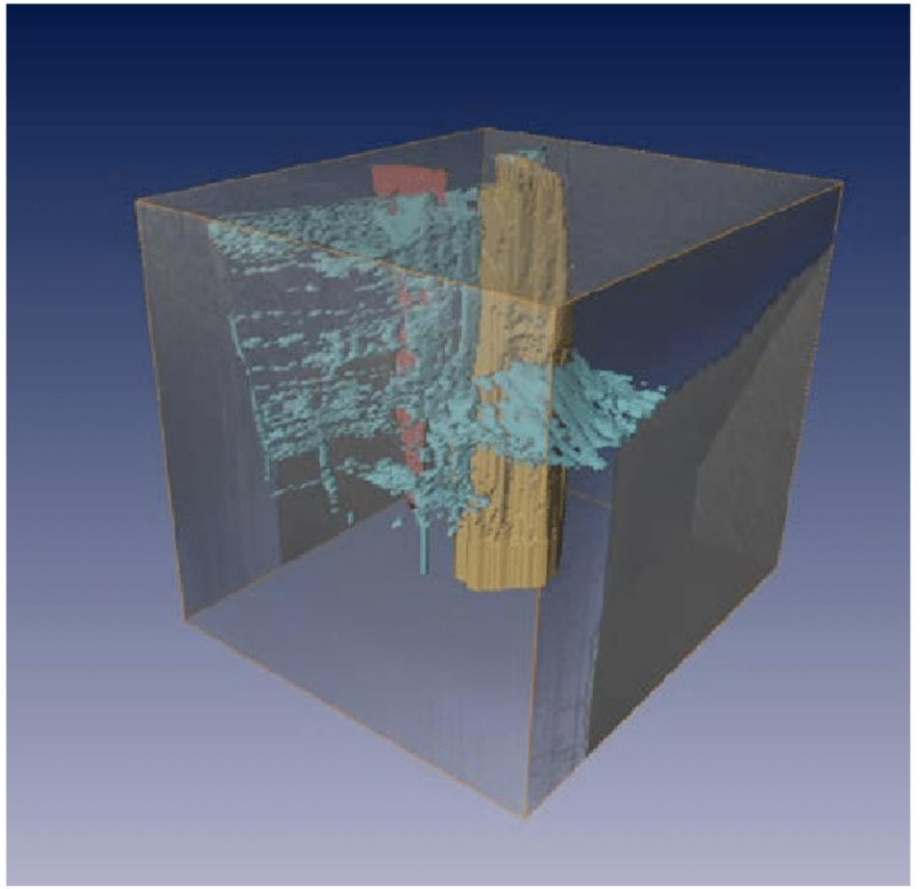

3D image of rolling contact fatigue cracks (light blue) around inclusions (yellow and orange) reconstructed with serial sectioning SEM images.

https://www.researchgate.net/figure/D-image-of-rolling-contact-fatigue-cracks-light-blue-around-inclusions-yellow-and_fig2_337841824

Microstructure

Fig. 14.13 (a) Fatigue crack nucleation at slip bands. (b) SEM of extrusions and intrusions in a copper sheet. (Courtesy of M. Judelwicz and B. Ilschner.)

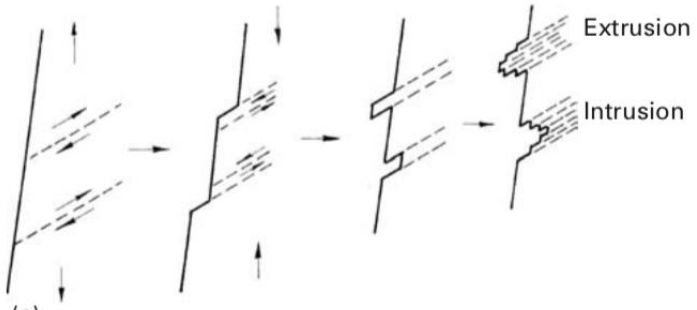

(a)

(b)

Fig. 14.12 Well-developed maze structure, showing dislocation walls on {100} in Cu–Ni alloy fatigued to saturation. (From P. Charsley, *Mater. Sci. Eng.*, 47 (1981) 181.)

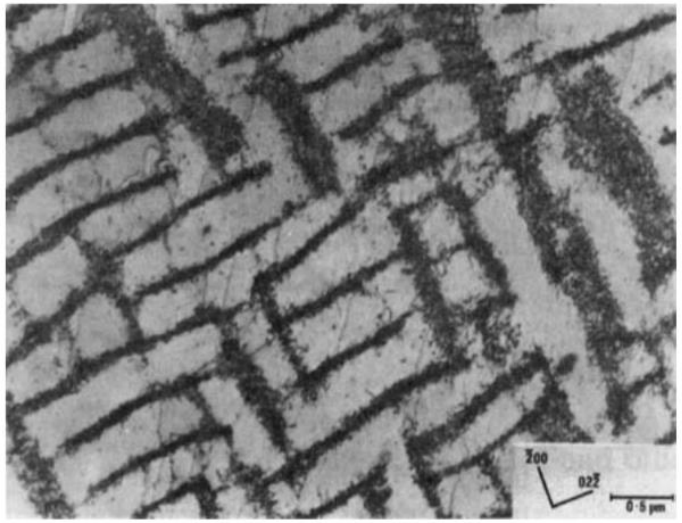

Laboratory tests and numerical simulation (TRIBOCode and T.E.S.T)

EFFICIENCY and DURABILITY

Local determination of lubrication - Tooth gear MODELING

LUBRICATION REGIMES IN GEAR CONTACT

Low engine rotation

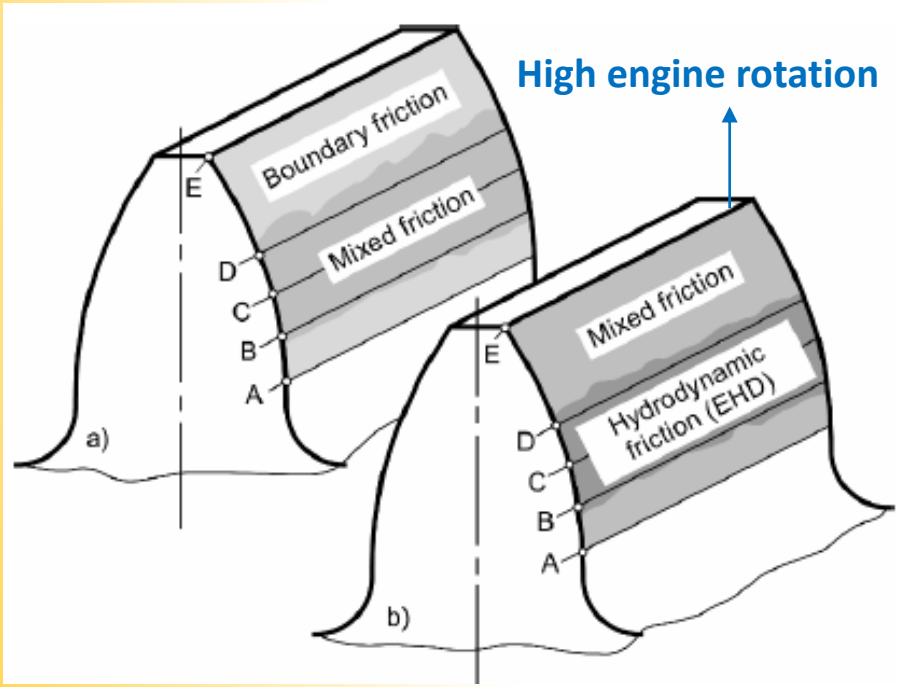

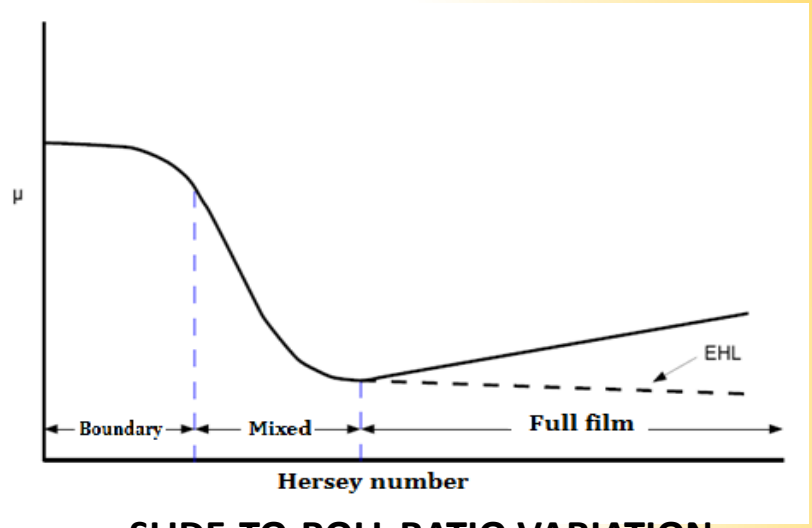

SLIDE-TO-ROLL RATIO VARIATION

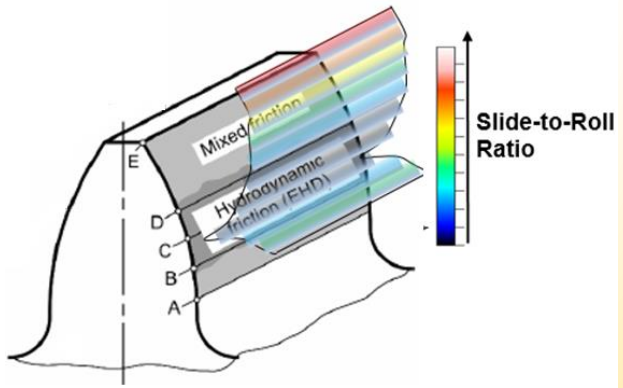

Local determination of lubrication - Tooth gear

Lubricant evaluation

Experimental tests: Mechanical losses due to friction in lubricated contact

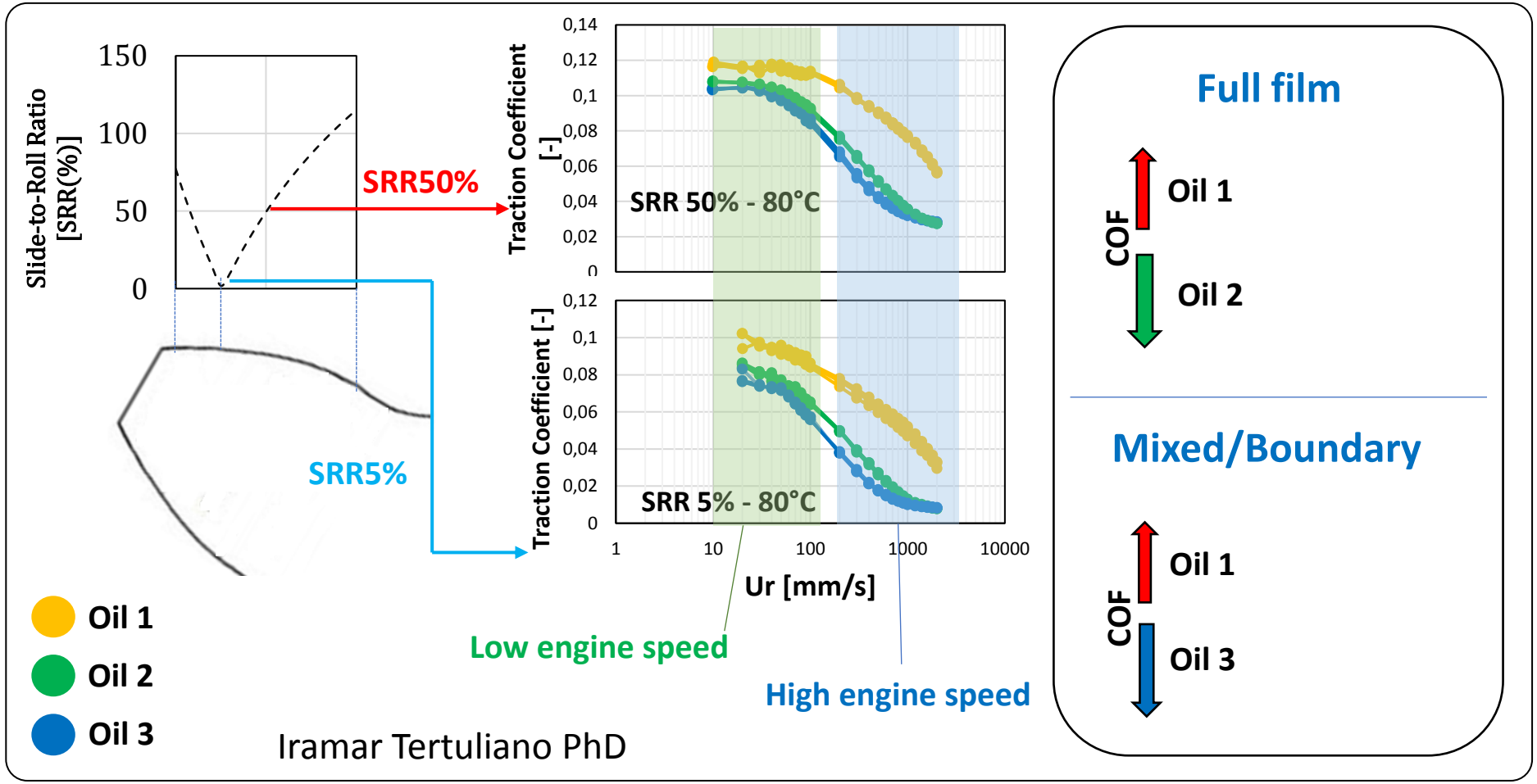

Iramar Tertuliano PhD

Stress Analysis to Improve Pitting Resistance in Gear Teeth

Newton K.Fukumasu Guilherme A.A.Machado Roberto M.Souza Izabel F.Machado
https://doi.org/10.1016/j.procir.2016.02.349

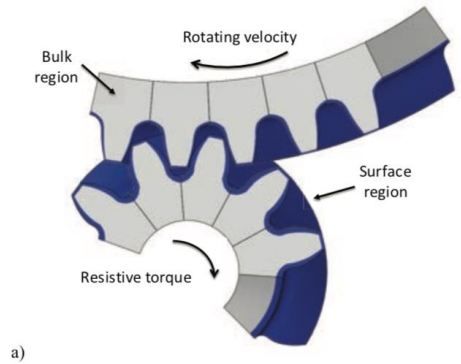

Fig. 1 – Finite Element Model of the helical gears: a) numerical model of five pairs of helical gear tooth, in which blue indicates the near surface region while the light gray indicates the bulk region of gear teeth; b) central point and path of numerical results extraction.

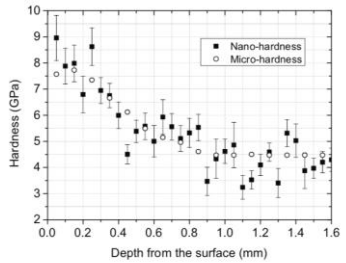

Fig. 3 – Hardness profile from surface towards the inner region of the helical gear measured by micro and nano-indentation techniques.

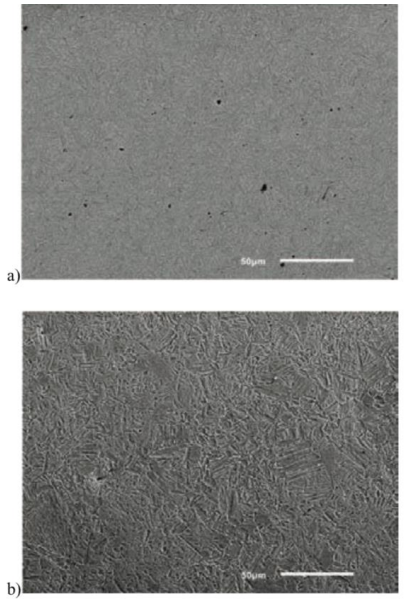

Fig. 2 – Back scattering SEM image of the microstructure of one gear tooth: a) bainitic inner region and b) martensitic surface region.

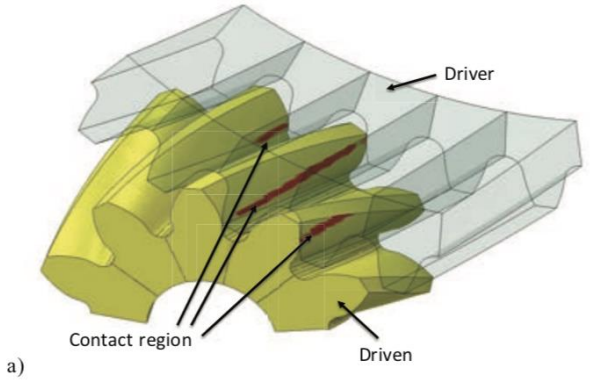

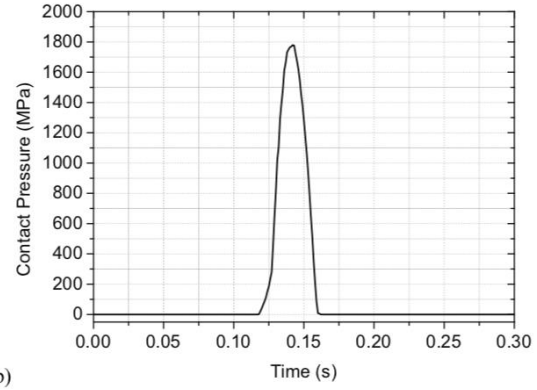

Fig. 4 – Contact in an engaged helical gear pair: a) contact region distributed in three pairs of gear tooth (red region) and b) evolution of contact pressure in the central point of the gear tooth (Fig. 1b).

Friction evaluation during contact – manual transmission

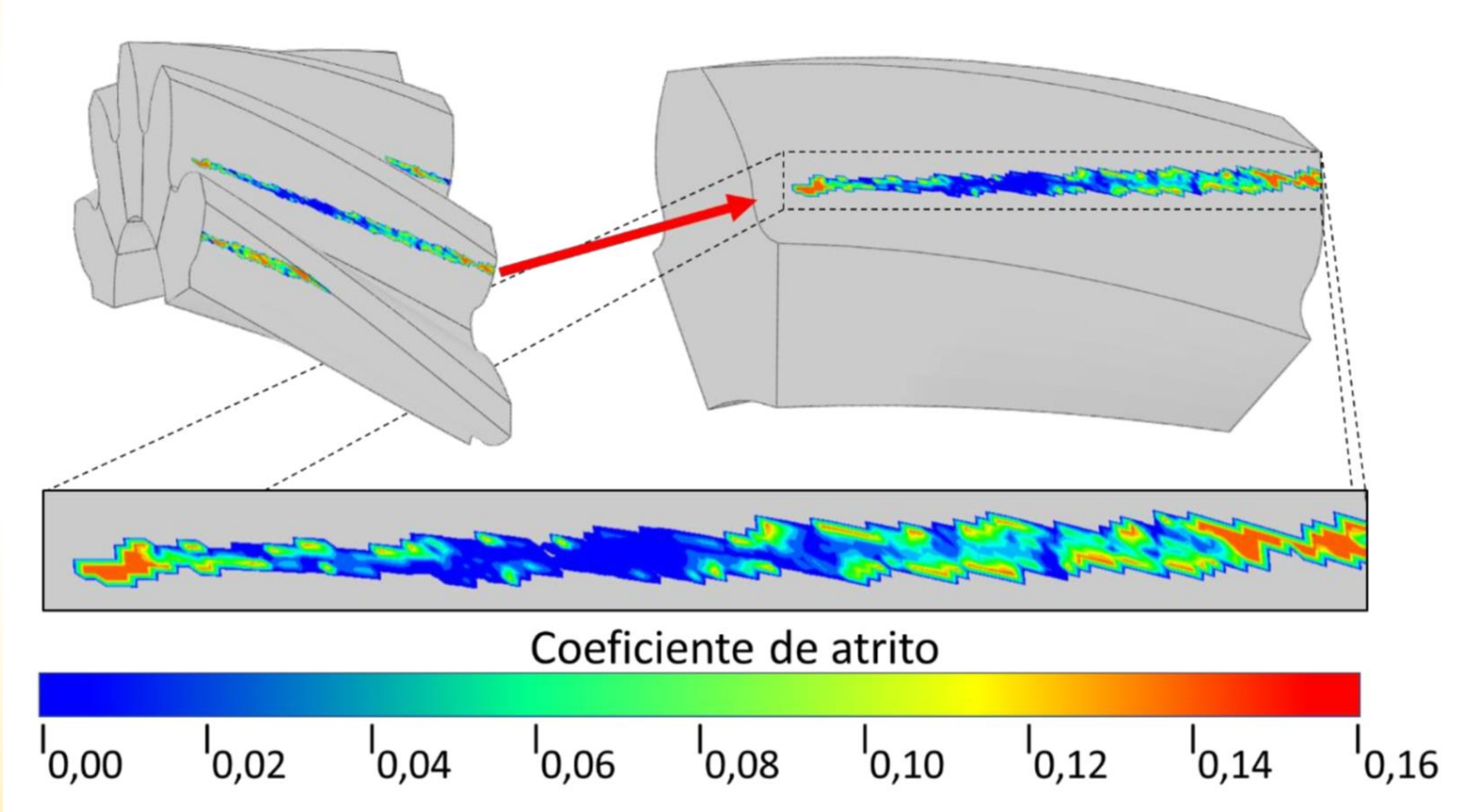

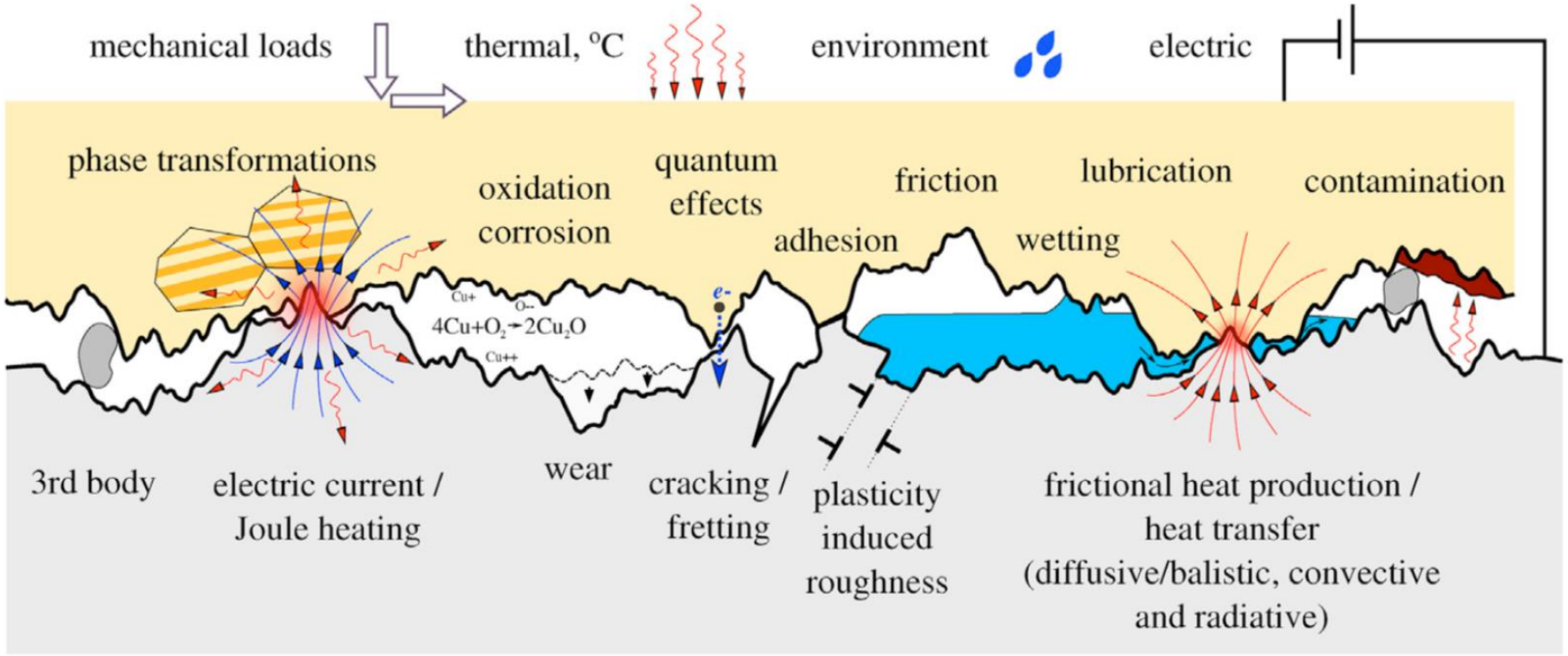

Fig. 2. A scheme representing the multiphysical nature of tribological interactions: two different solids with rough surfaces and relevant material microstructures are brought into mechanical contact and exposed to various loads: mechanical, thermal, electric, and environmental.

https://doi.org/10.1016/j.triboint.2018.02.005

Indentation size effect (ISE)

If a very low load is used, the measured micro-hardness is usually high; with an increase in test load it decreases. Such a phenomenon is referred to as “normal” ISE. It may be caused by the testing equipment or by intrinsic structural factors of the material: work hardening during indentation, load to initiate plastic deformation, elastic resistance and mixed elastic/plastic deformation response of material, the effect of indenter/specimen friction resistance, the effect of machining-induced residually stressed measured surface]. In the literature, there are many examples of “normal” ISE occurrence in brittle materials including glass.

In contrast to “normal“ ISE, a reverse (inverse) ISE (RISE), where the micro-hardness increases with increasing load, is also known. It essentially takes place in materials in which plastic deformation is predominant.

http://yadda.icm.edu.pl/baztech/element/bwmeta1.element.baztech-44573344-bfa8-42f6-af6d-a63081723649/c/Petrik_on_the_AMM_4_2016.pdf

Indentation size effect (ISE)

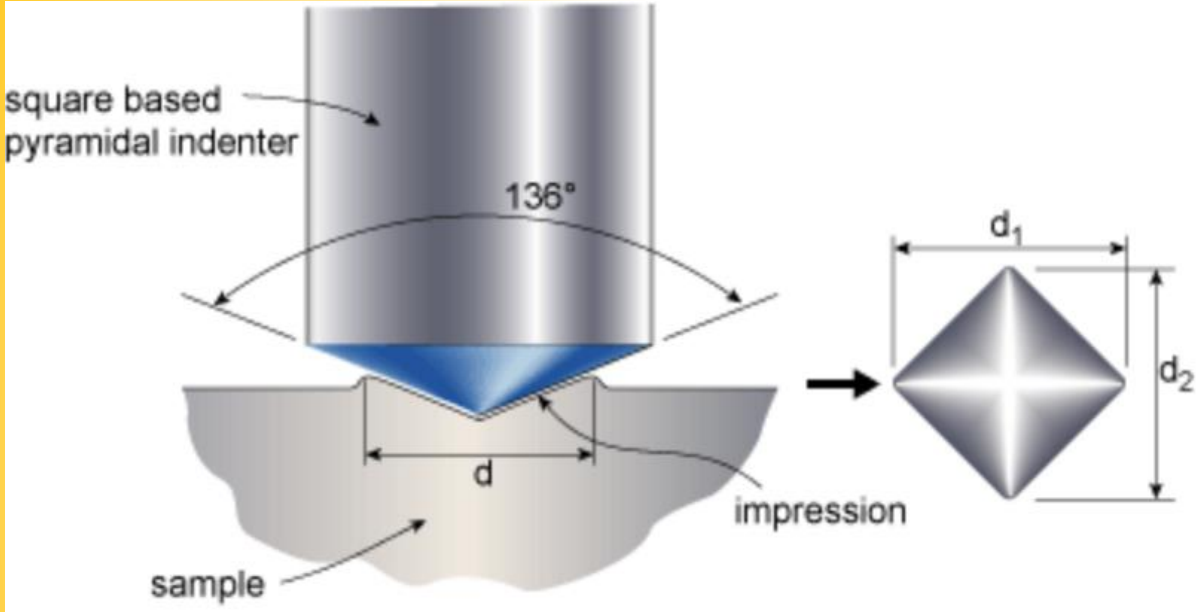

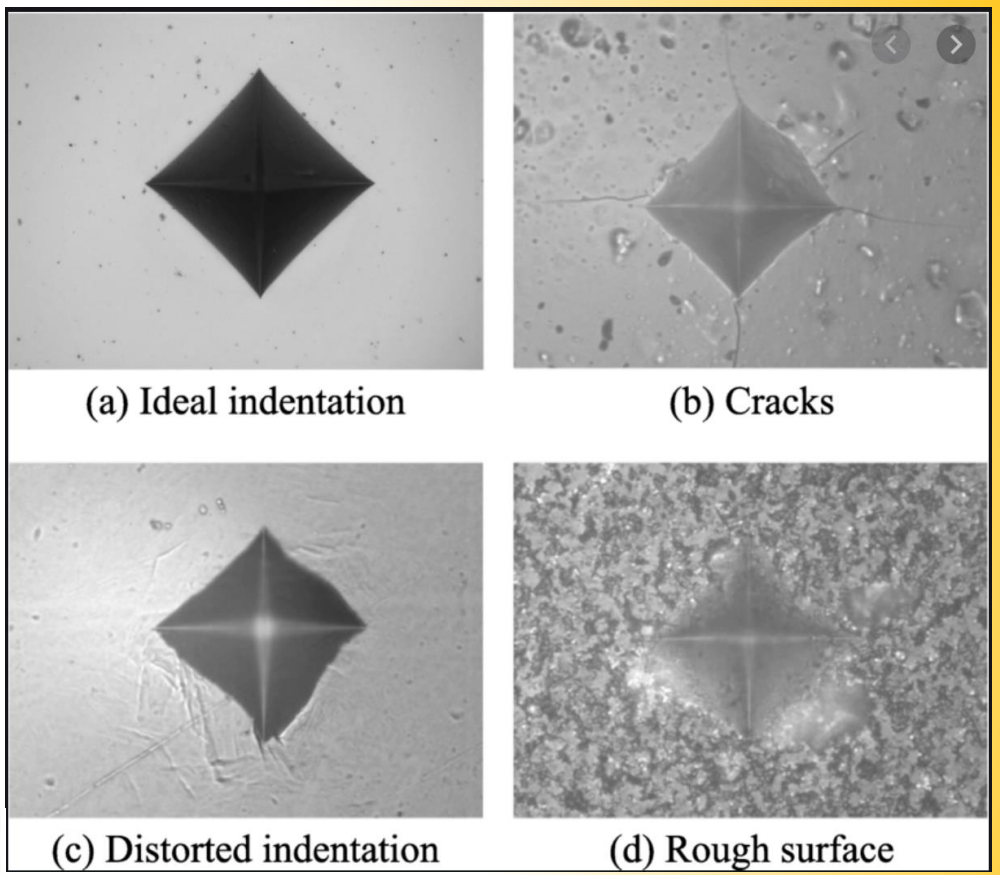

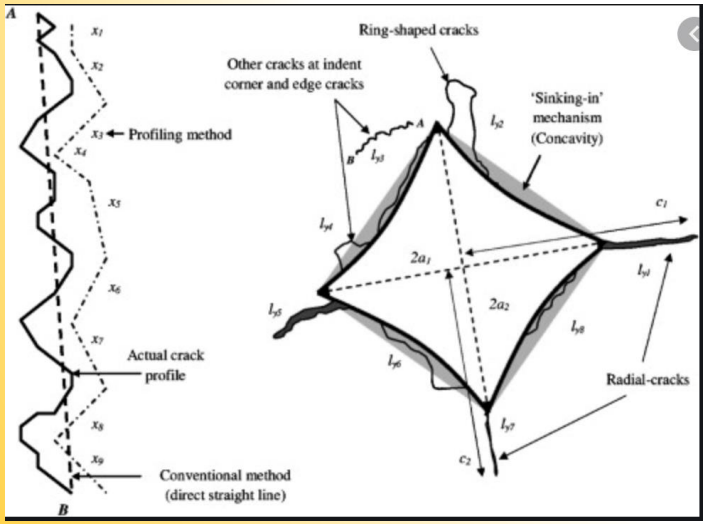

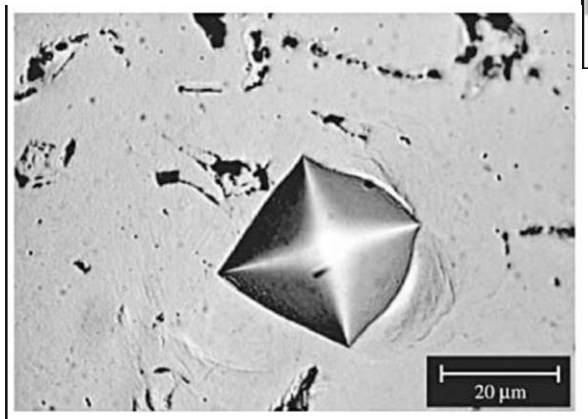

9. Vickers impression on top of aluminum. Load = 255 mN.

Tensões Residuais.

As tensões residuais resultam de deformações permanentes não uniformes na seção resistente de uma peça ou estrutura. As tensões residuais são tensões, que atuam num componente ou estrutura na ausência de esforços externos, sejam cargas mecânicas, esforços resultantes de gradientes de temperatura e etc. Se as tensões residuais ultrapassarem o limite de escoamento no local onde atuam, elas causaram um colapso plástico .

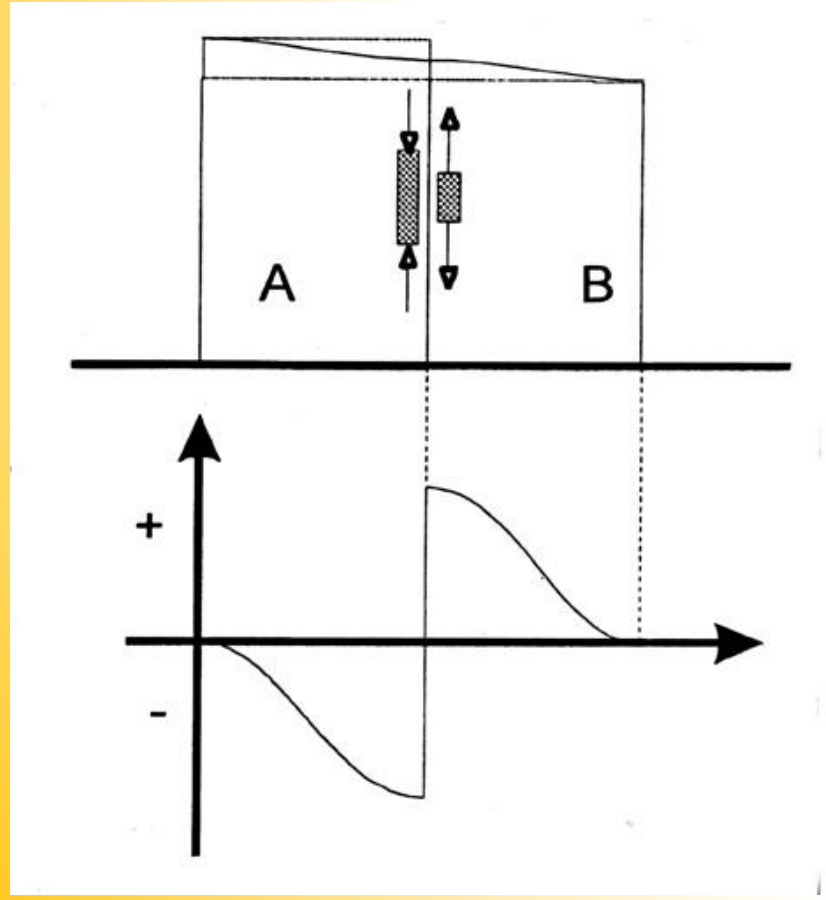

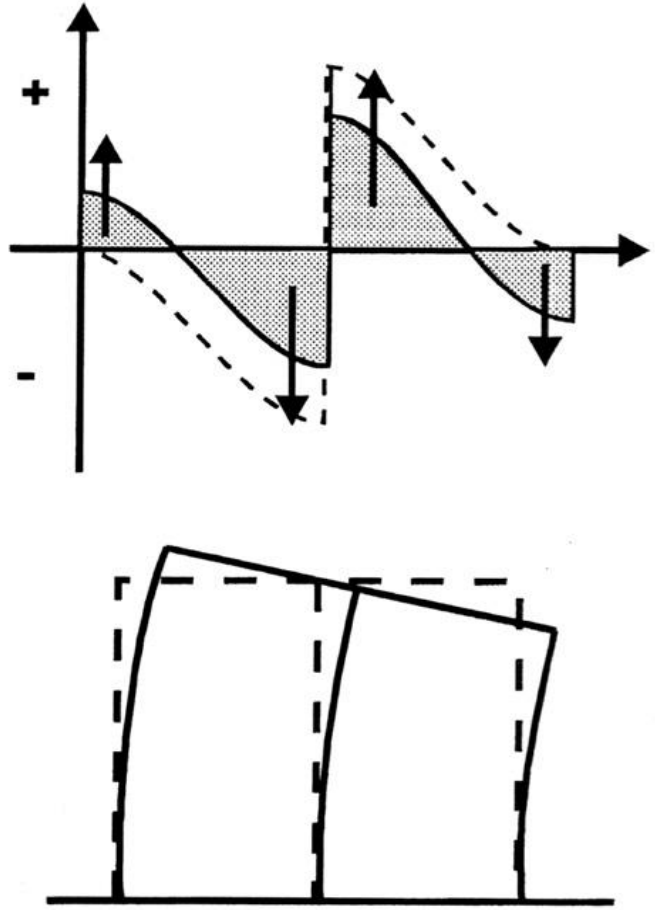

Elementos Finitos

LAMINAÇÃO A QUENTE

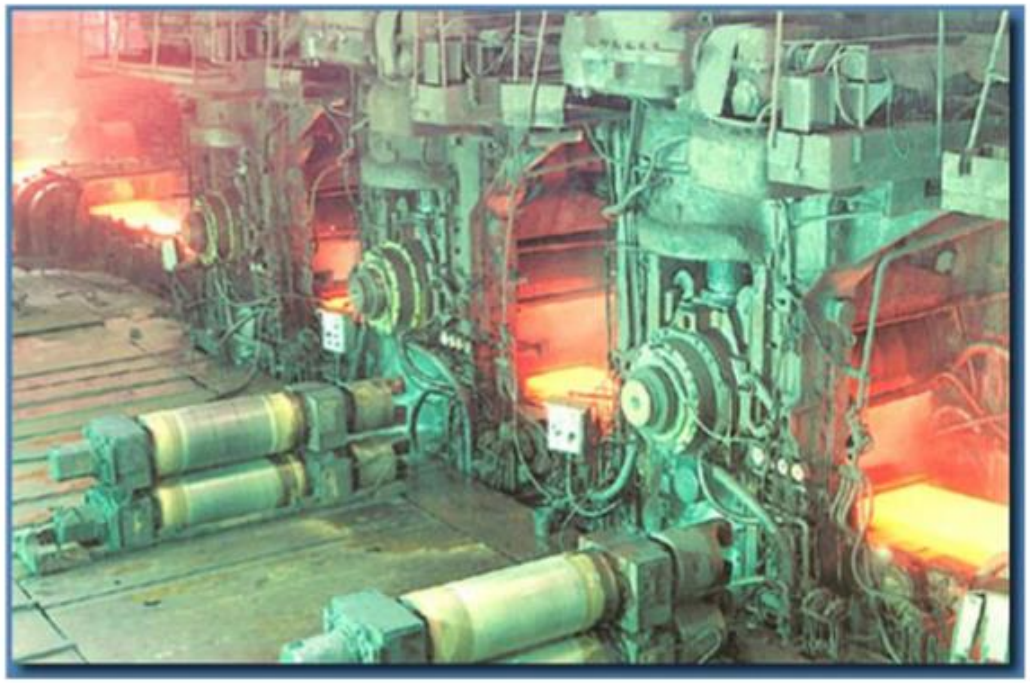

Laminador de tiras a quente

Laminador de tiras a quente

Elementos Finitos

Os cilindros de laminação podem utilizados como cilindros de trabalho ou cilindros de encosto (ou apoio).

- Os cilindros de trabalho são aqueles que entram em contato direto com o material laminado. Sofrem, portanto, as maiores solicitações de temperatura e desgaste.

- Os cilindros de encosto (ou apoio) são aqueles que não entram em contato com o material laminado, mas sim com o cilindro de trabalho. Servem para apoiar o cilindro de trabalho impedindo sua flexão. Para isso, são cilindros de maior porte.

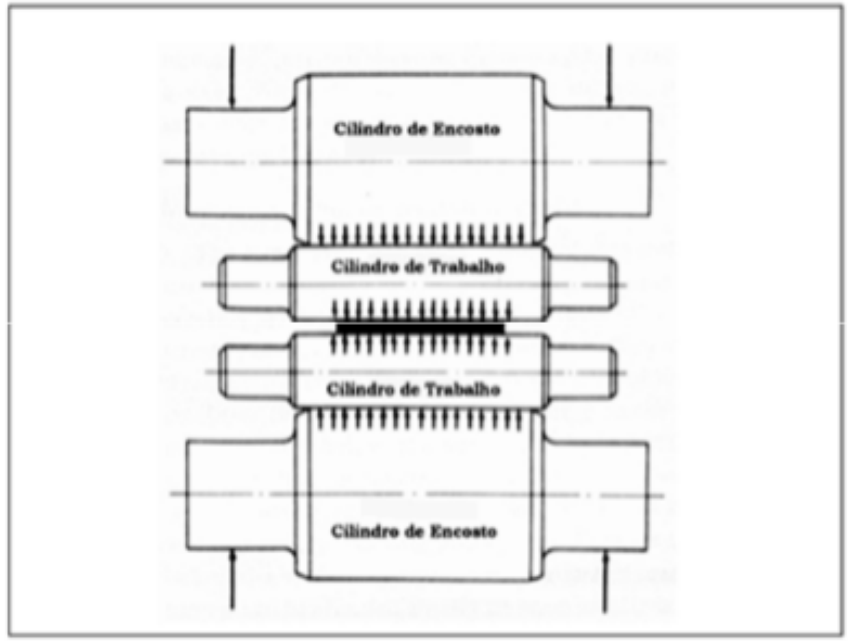

FEM Macroscale

- **PART 1:**

Workpiece - 3D – Deformable – Solid

20 x 20 x 200 m^3

Roller - 3D – Discrete Rigid – Solid – Extrusion

$\emptyset\ 100\ m$
Depth = 45 m

Create Reference Point (Tools).

- **PROPERTIES:**
  Workpiece - Steel

Plastic:

Yield Stress	Plastic Strain
380e6	0
420e6	0.04
470e6	0.12
500e6	0.19
530e6	0.25

- **PROPERTIES:**
  Workpiece - Steel

Elastic: E = 200 GPa;
$\nu = 0.3;$

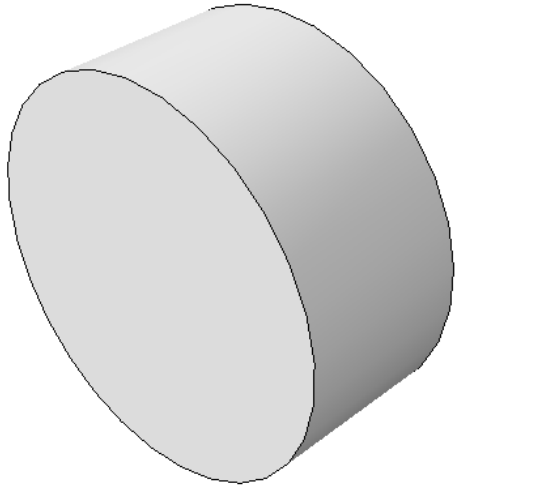

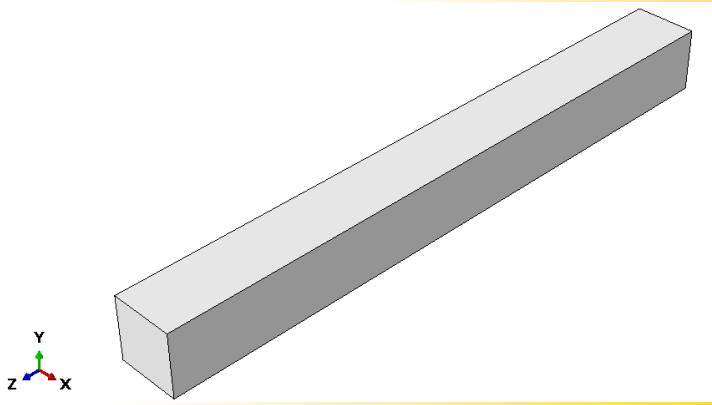

FEM Macroscale

- **ASSEMBLY:**

Rotate and Translate the Workpiece

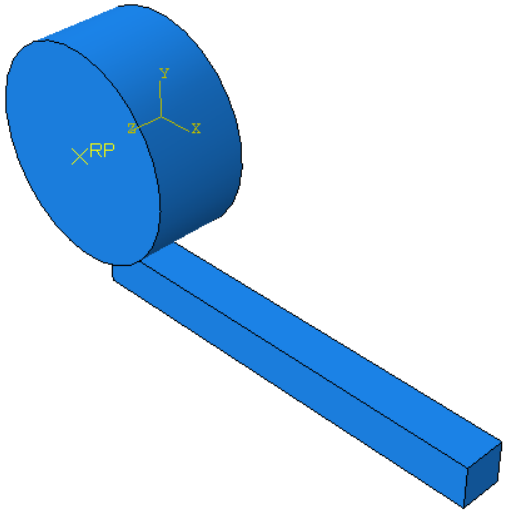

- **INTERACTION:**

Surface-to-surface;

Penalty: COF = 0.3;

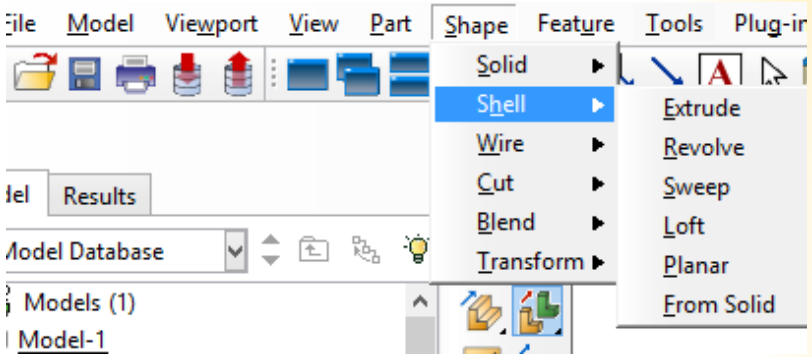

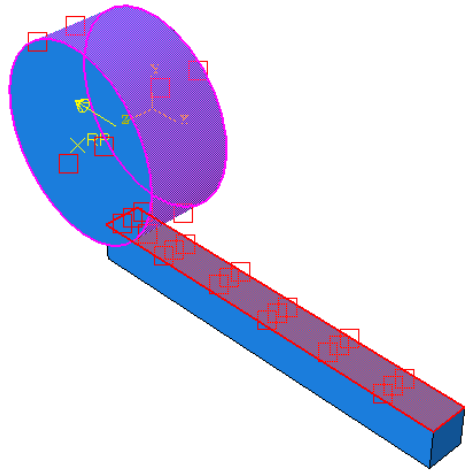

FEM Macroscale

- **LOAD:**

Workpiece

Pre-defined field (V_1 = - 70 m/s);
ZSymm;
YSymm.

RP – Roller:

Initial Step - $U_1 = U_2 = U_3 = UR_1 = UR_2 = 0$
Step -1: VR_3 = -5 rad/s

- **MESH:**

Workpiece: Hex (C3DR8) – Global Size: 3;

Roller: R3D4 – Global Size: 3;

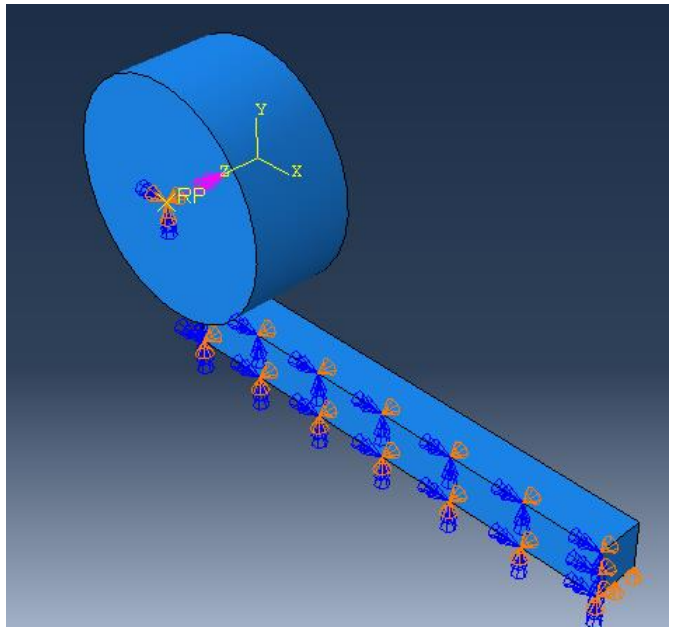

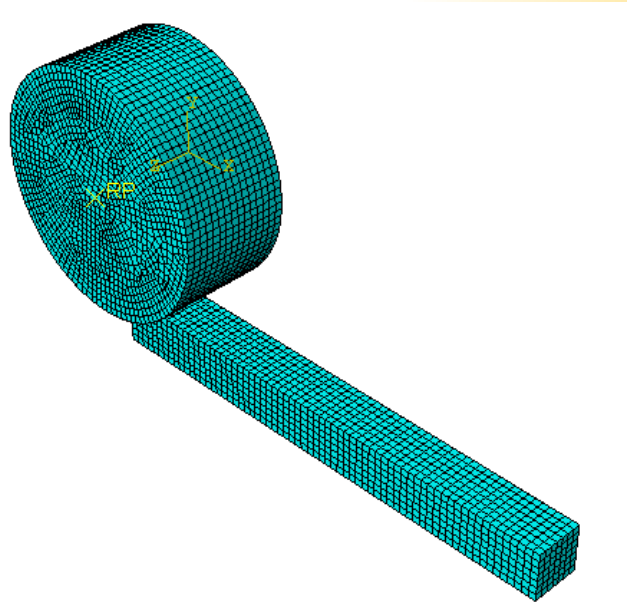

FEM Macroscale

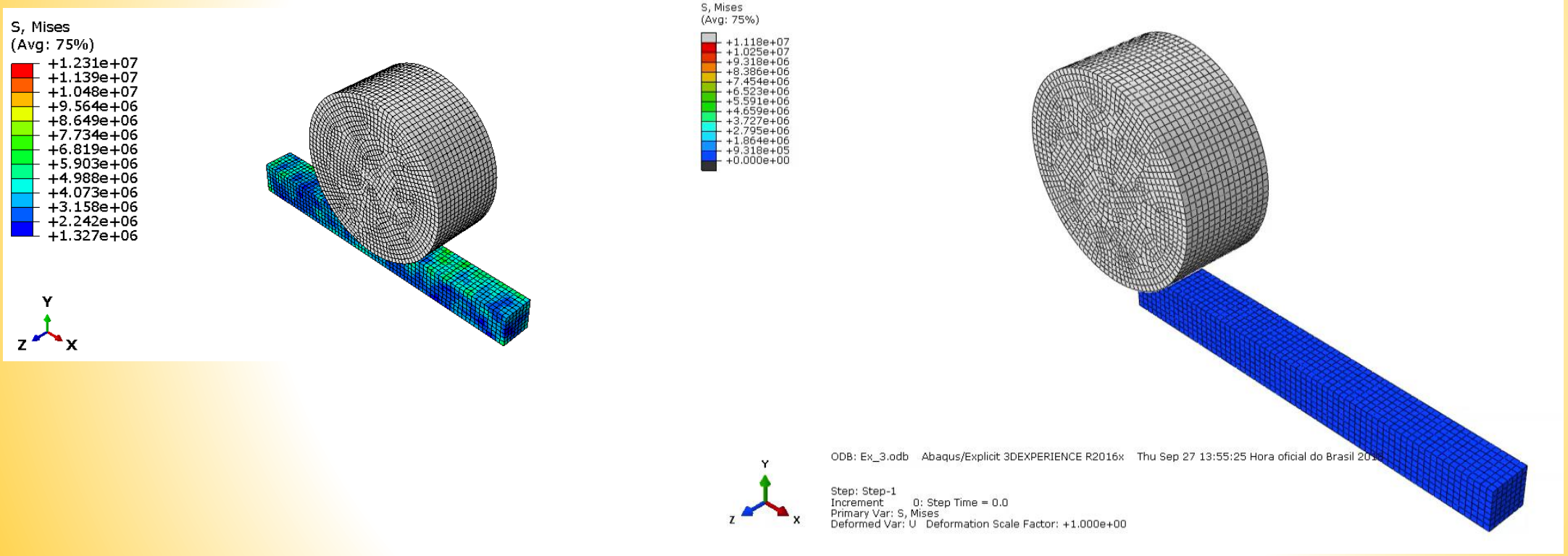

FEM Microescale

CAD, Parameters, MICROSTRUCTURE

X-Ray Tomography : resolution, densities of phases

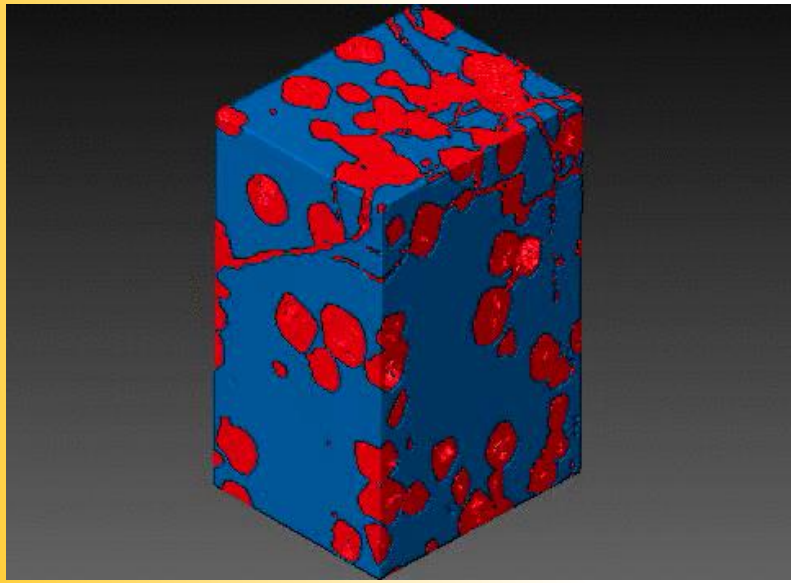
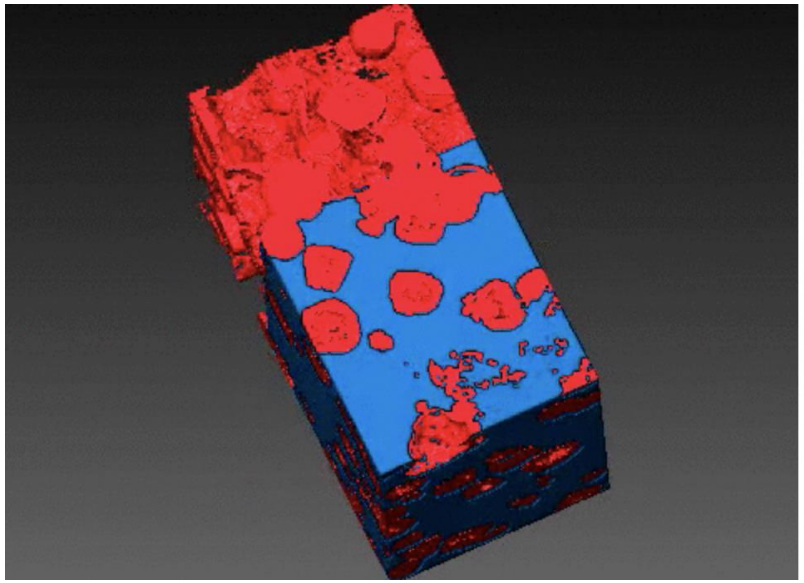
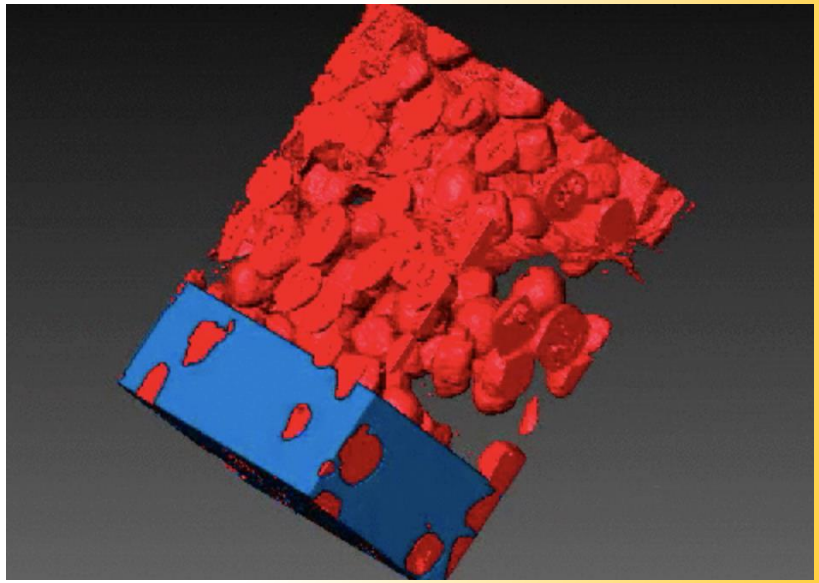

https://commons.wikimedia.org/wiki/File:Micro_CT_analysis_of_Ti2AlC_and_Al_composite.gif

FEM Microescale

CAD, Parameters, MICROSTRUCTURE

Softwares

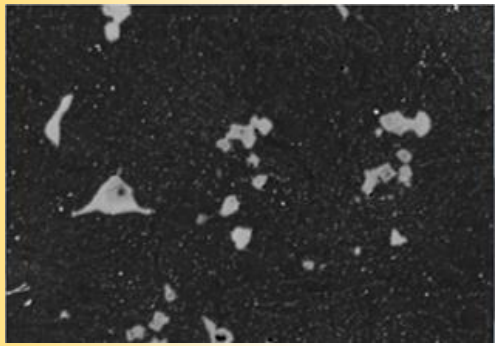

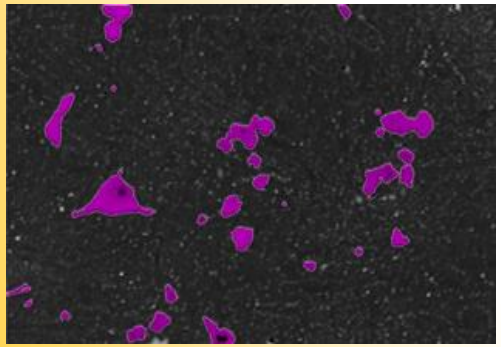

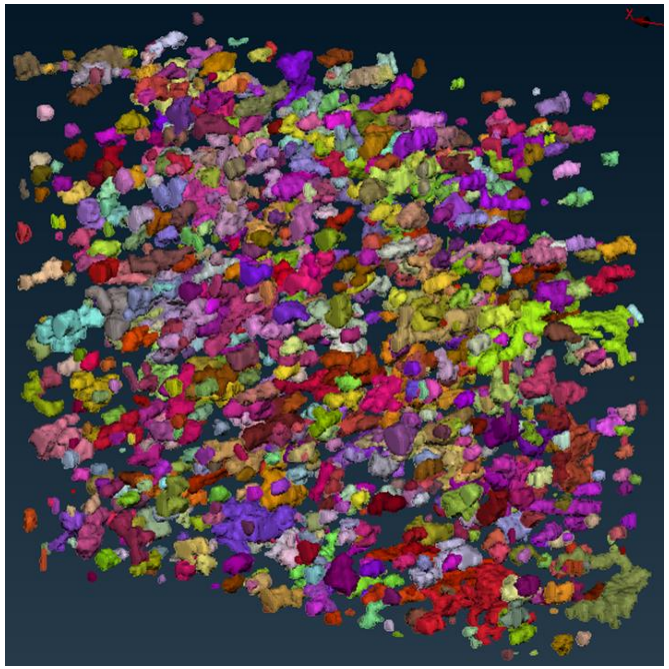

FEM Microescale

CAD, Parameters, MICROSTRUCTURE

FIB - EBDS

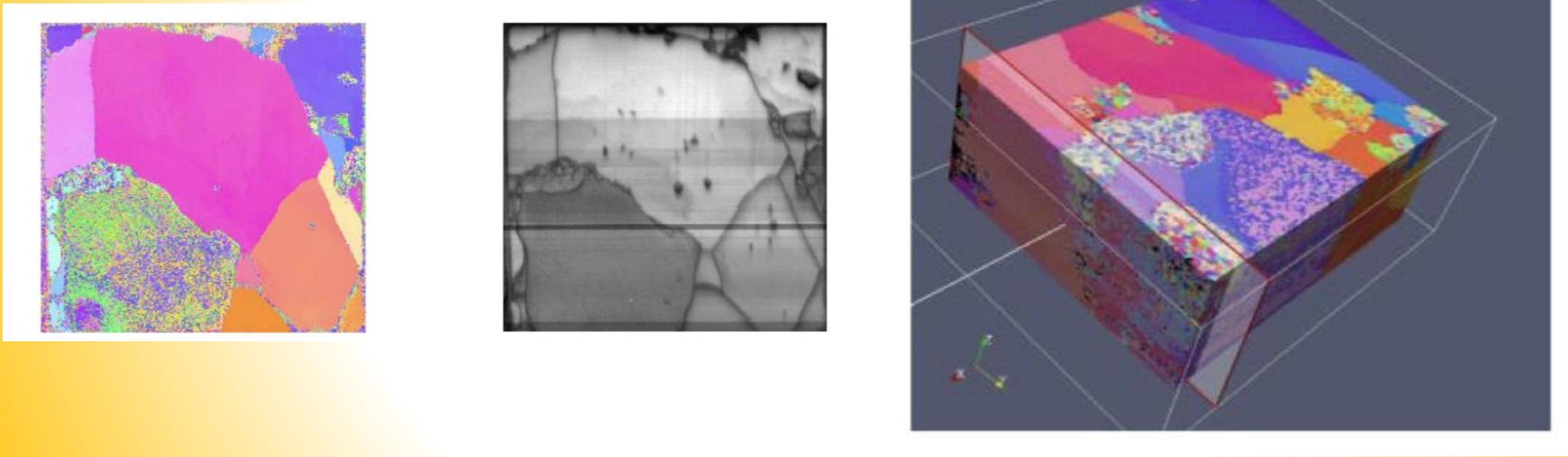

https://www.osti.gov/servlets/purl/1358236

FEM Microescale

CAD, Parameters, MICROSTRUCTURE

Softwares

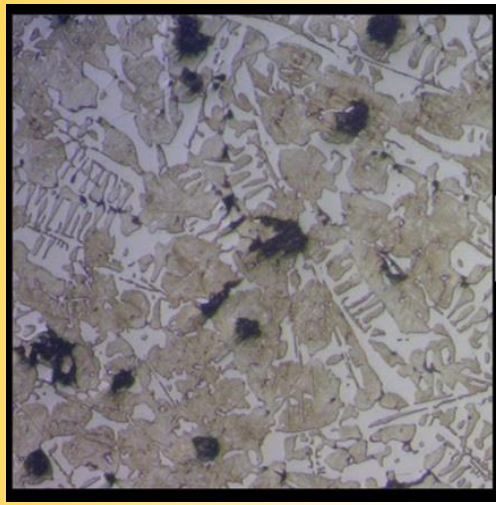

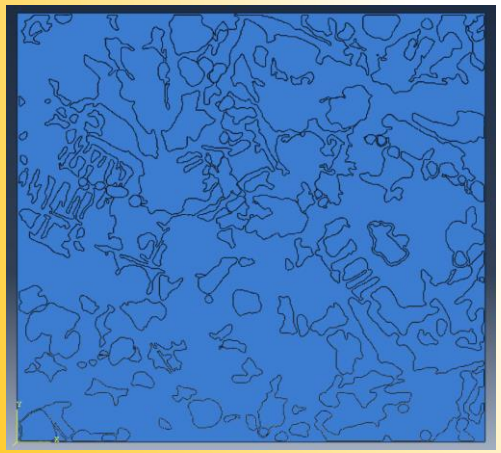

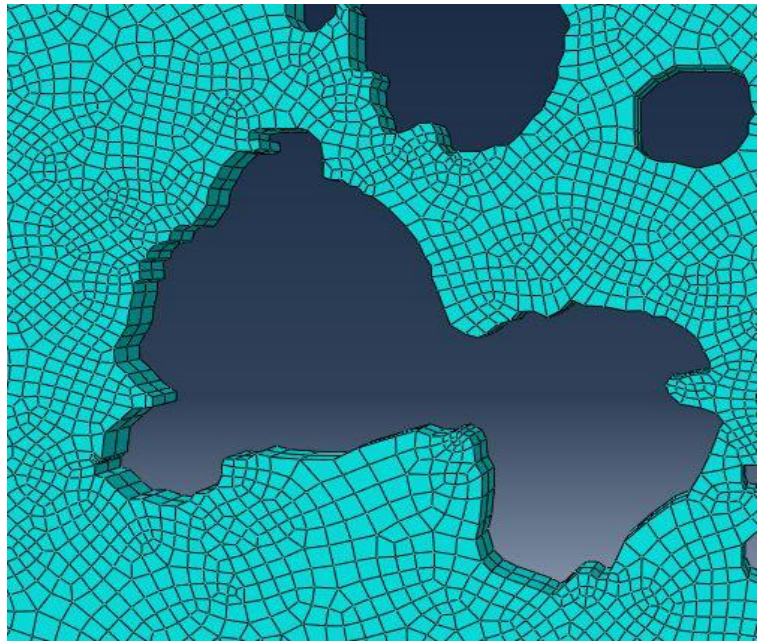

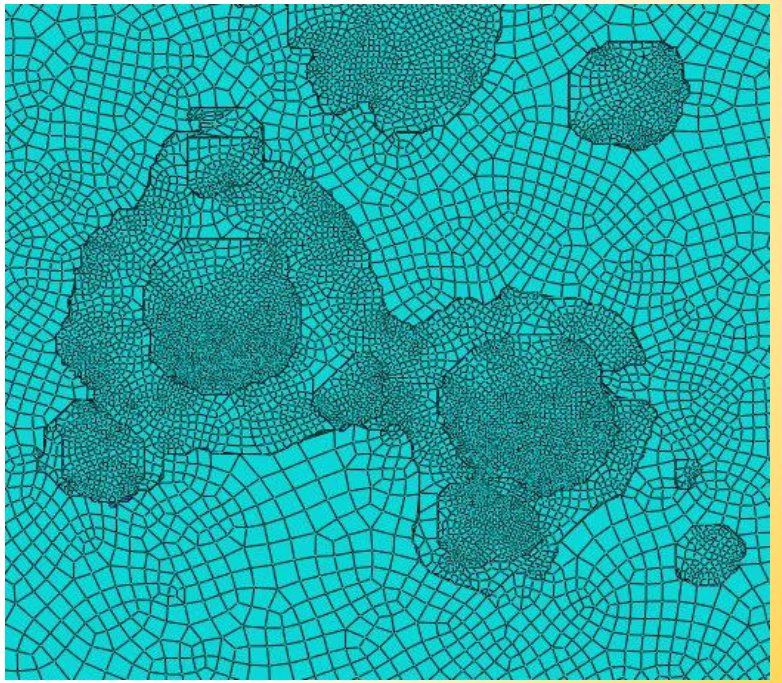

Izabel Machado – machadoi@usp.br

Mechanical and Tribological (Micro) Behavior Assessment using Finite Element Method Tools

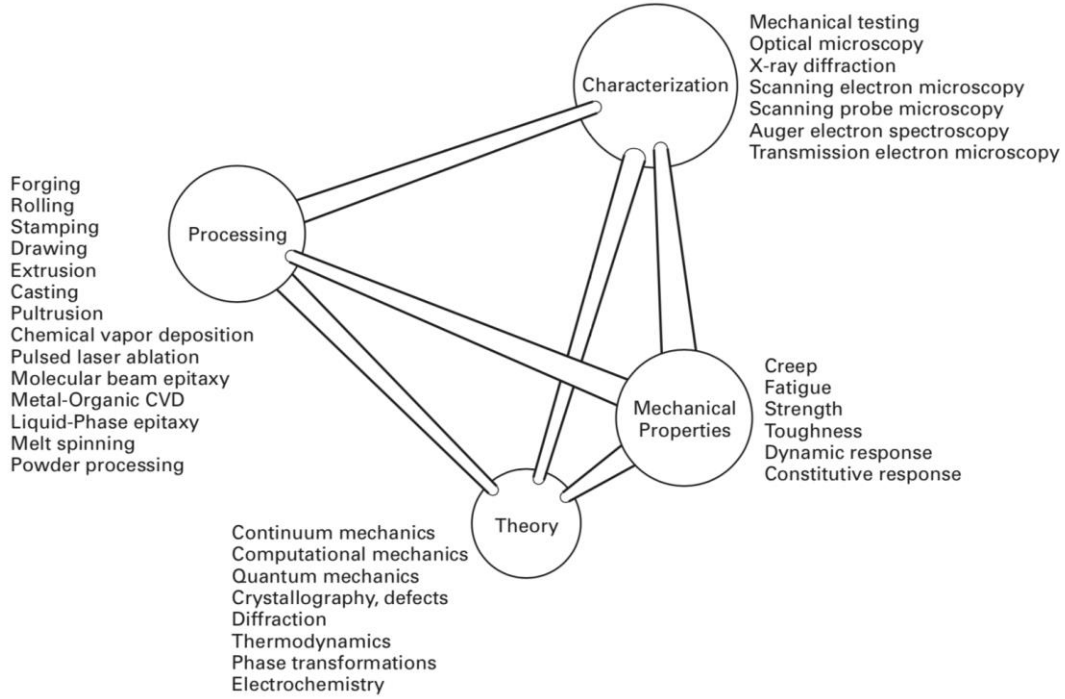

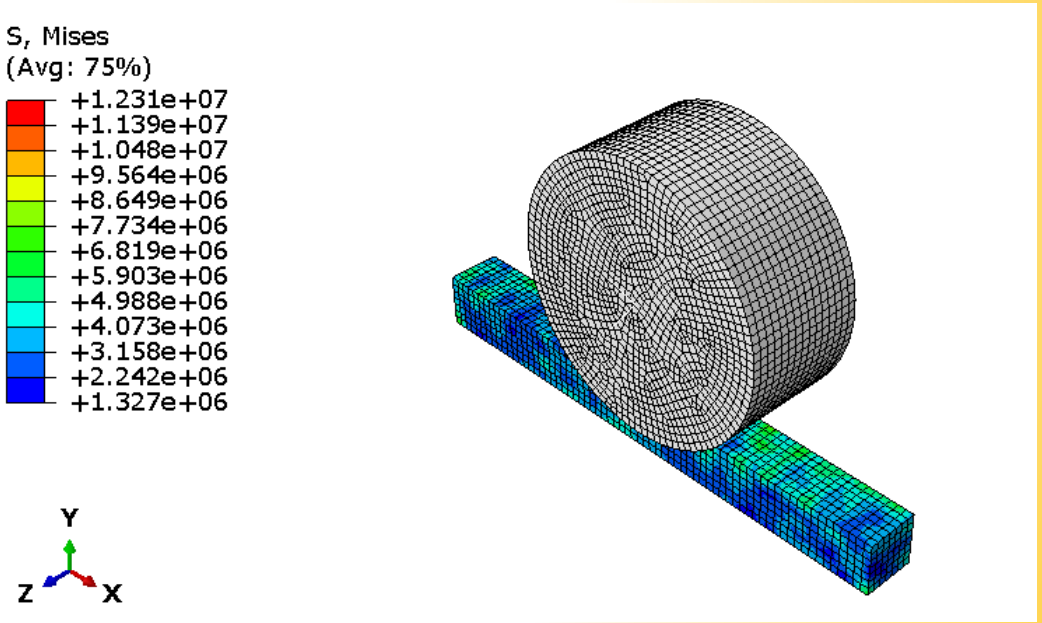

Meyers and Chawla, Mechanical behavior of Materials , 2009

Scales - FEM

2D Analysis: Stresses at the microstructural level - ABAQUS + ppm2oof (NIST, USA)

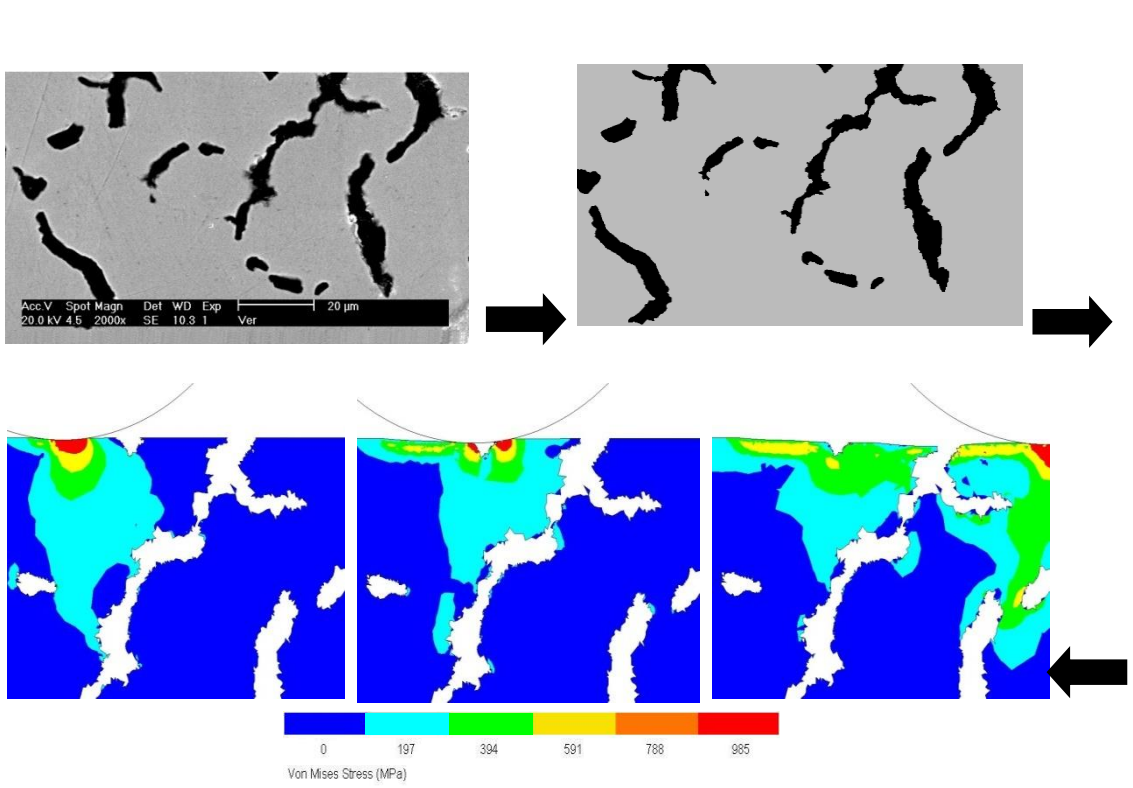

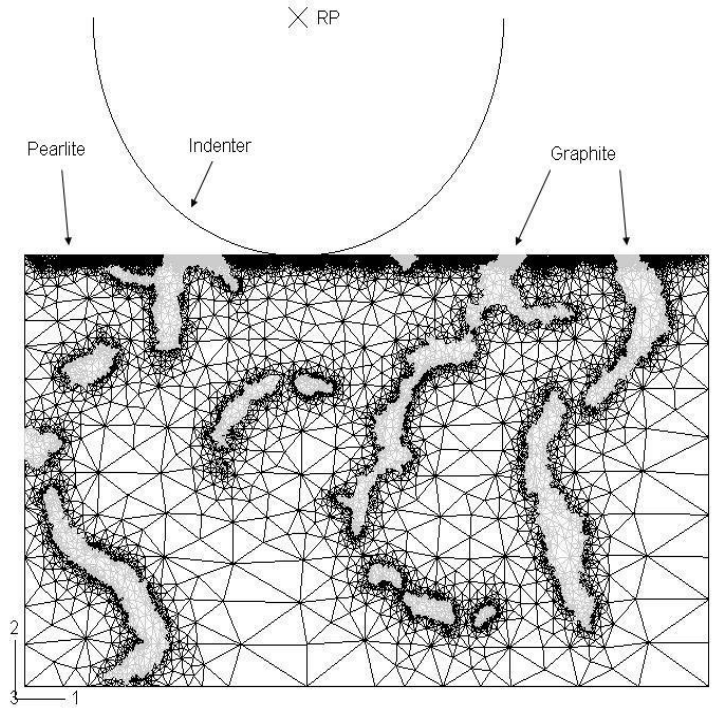

roberto.souza@poli.usp.br

[N.K. Fukumasu et al. Wear 2005]

Finite element analysis of the effects of thermo-mechanical T loadings on a tool steel microstructure

V. Seriacopi, N.K. Fukumasu, R.M. Souza, I.F. Machado, Engineering Failure Analysis , https://doi.org/10.1016/j.engfailanal.2019.01.006

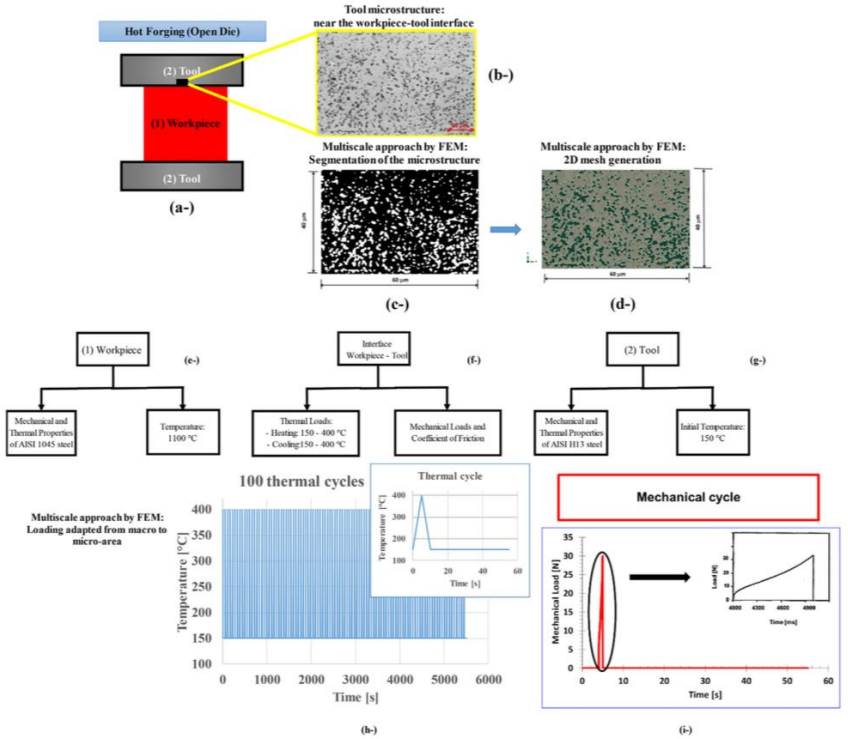

Fig. 1. Schematic representation containing the assumption of the micro-analyses conducted from the macroscopic system, mainly focused on the hot forging tool. Simplified frames are provided to specify the inputs of the models: purely thermal and thermo-mechanical loadings: (a-) general layout of the open die forging process, where (1) is the workpiece and (2) is the tool; (b-) microstructure of the tool steel studied; (c-) micrograph after segmentation, considering gray scales; (d-) 2D mesh assigned to the microstructural region evaluated; (e-) inputs of the numerical model regarding the workpiece – AISI 1045 steel; (f-) inputs of the numerical model regarding the interface between tool and workpiece; (g-) inputs of the numerical model regarding the tool – AISI H13 steel; (h-) thermal cycle considered on the analyses; and (i-) mechanical cycle evaluated by numerical modelling.

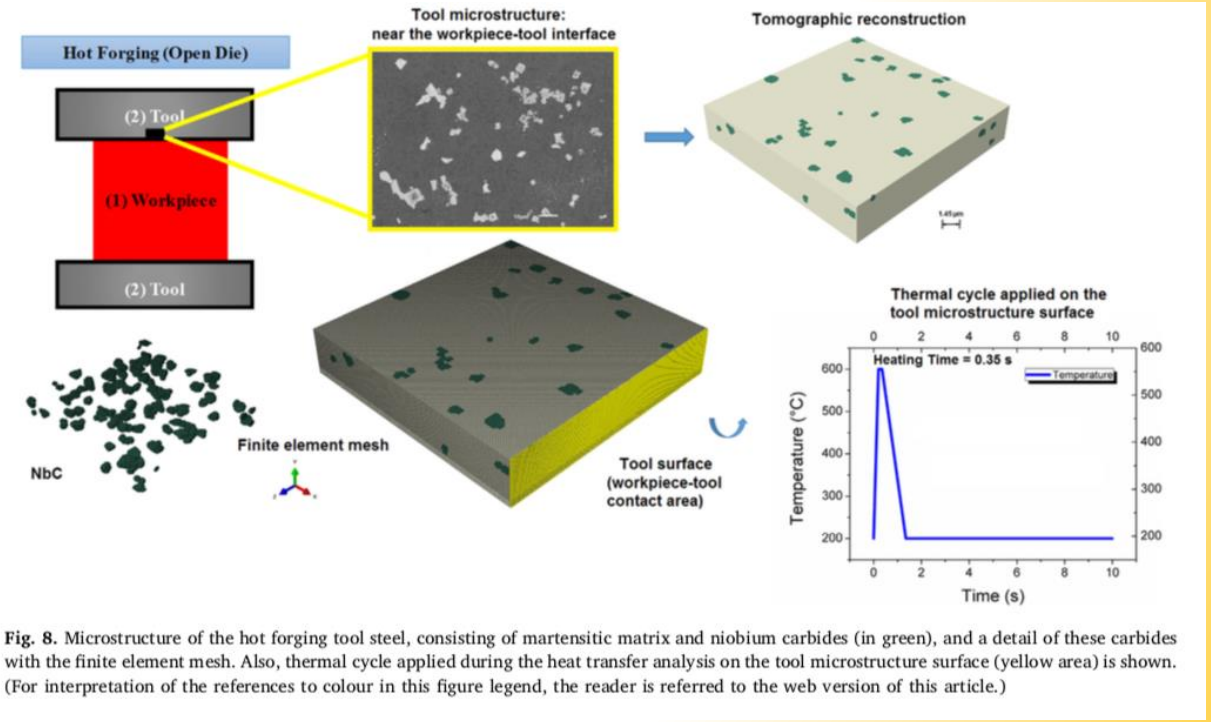

Fig. 8. Microstructure of the hot forging tool steel, consisting of martensitic matrix and niobium carbides (in green), and a detail of these carbides with the finite element mesh. Also, thermal cycle applied during the heat transfer analysis on the tool microstructure surface (yellow area) is shown. (For interpretation of the references to colour in this figure legend, the reader is referred to the web version of this article.)

Finite element analysis of the effects of thermo-mechanical loadings on a tool steel microstructure

V. Seriacopi, N.K. Fukumasu, R.M. Souza, I.F. Machado, Engineering Failure Analysis , https://doi.org/10.1016/j.engfailanal.2019.01.006

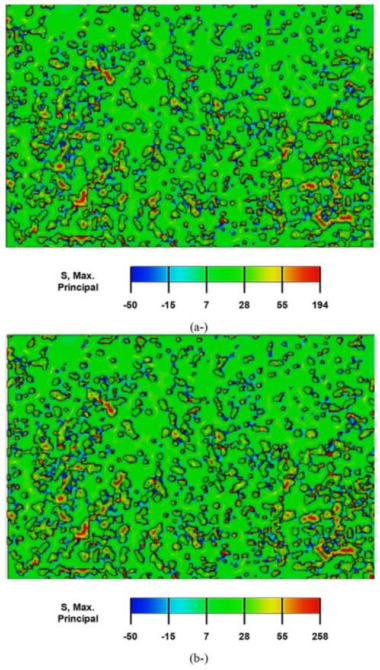

Fig. 6. Thermo-mechanical Loading results: Evolution of the results for Maximum Principal Stress [MPa] obtained during the post-cooling: (a-) First cycle; (b-) Hundredth Cycle.

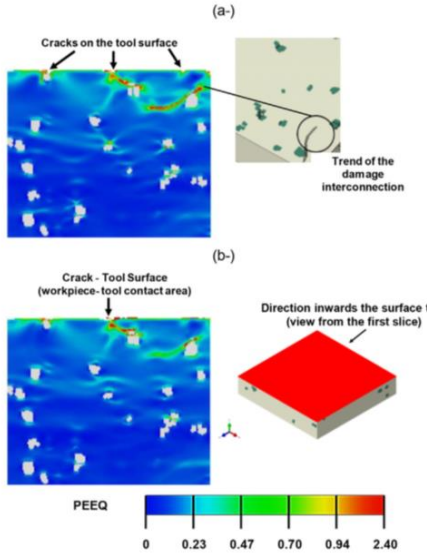

Fig. 11. View from the first slice in the direction inwards the surface tool - Equivalent plastic strain (PEEQ) field after the cooling for the following cases of NbC fracture toughness: 5 $MPam^{1/2}$ (a) and 7 $MPam^{1/2}$ (b).

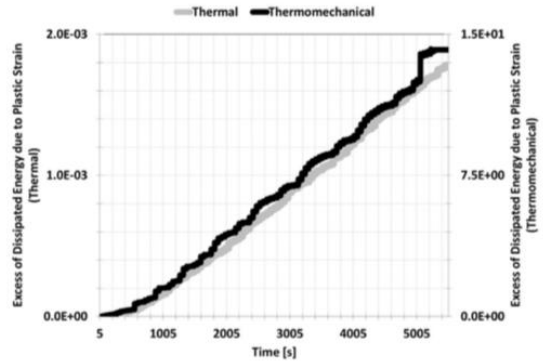

Fig. 7. Excess of the energy dissipated due to plastic strain along the time during 100 thermal cycles. This parameter was calculated from the normalized relation by 5 first seconds of heating.

Experimental and numerical analysis of dry contact in the pin on disc test

E.M. Bortoleto, A.C. Rovani, V. Seriacopi, F.J. Profito, D.C. Zachariadis, I.F. Machado, A. Sinatora, R.M. Souza, WEAR. http://dx.doi.org/10.1016/j.wear.2012.12.005

Table 2
Material properties of the pin (AISI 4140 steel) and disc (AISI H13 steel) [14].

	Material	
	AISI 4140 (wt%)	AISI H13 (wt%)
Density [kg/m^3]	7885	7800
Elastic modulus [GPa]	210	210
Poisson's ratio	0.29	0.3
Yield stress [MPa]	1370	1410

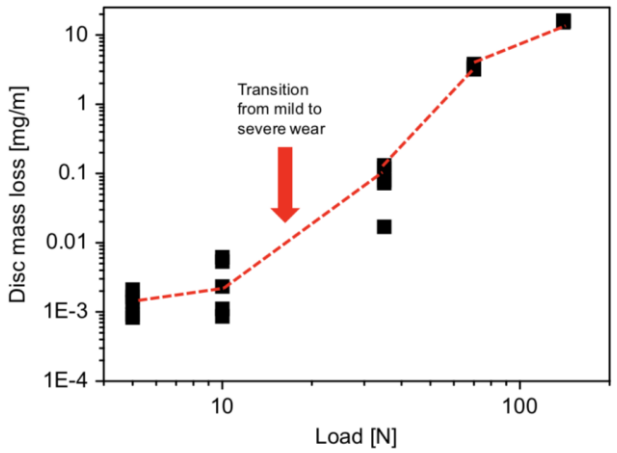

Fig. 6. Disc mass loss of the experimental results for the 5, 10 35, 70 and 140 N.

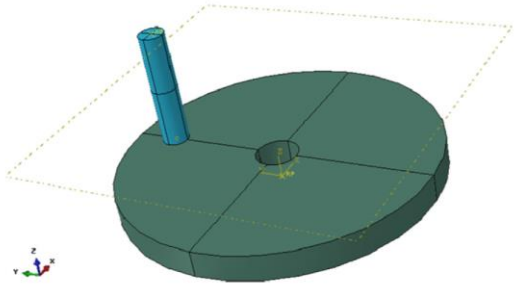

Fig. 1. Geometry of the contact pair pin on disc (tribological system).

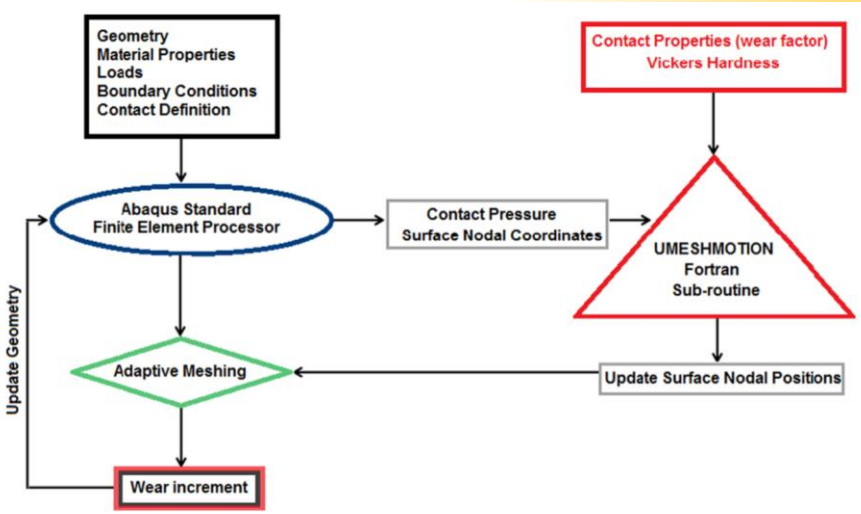

Fig. 4. Flowchart for the UMESHMOTION subroutine.

Experimental and numerical analysis of dry contact in the pin on disc test

E.M. Bortoleto, A.C. Rovani, V. Seriacopi, F.J. Profito, D.C. Zachariadis, I.F. Machado, A. Sinatora, R.M. Souza, WEAR. http://dx.doi.org/10.1016/j.wear.2012.12.005

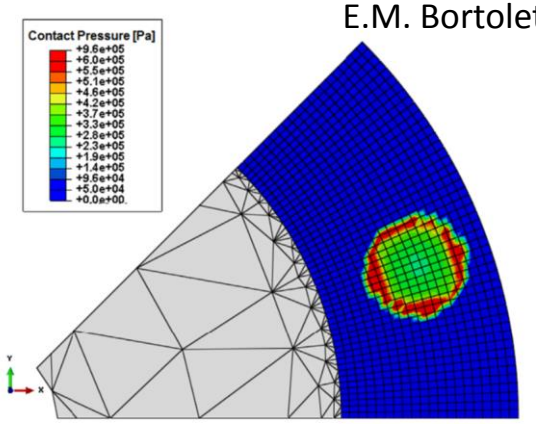

Fig. 8. Contact pressure on the disc surface during pin sliding with 10 N normal load.

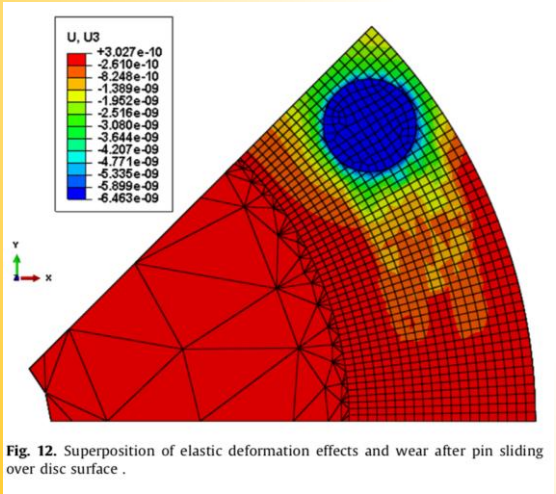

Fig. 12. Superposition of elastic deformation effects and wear after pin sliding over disc surface .

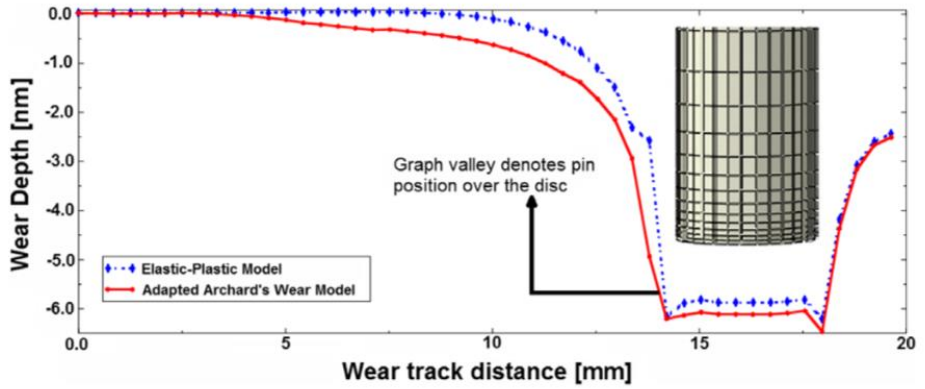

Fig. 11. Comparison between wear profile (continuous line) and elastic deformation (dashed line) during pin sliding over disc under 10 N load along movement direction.

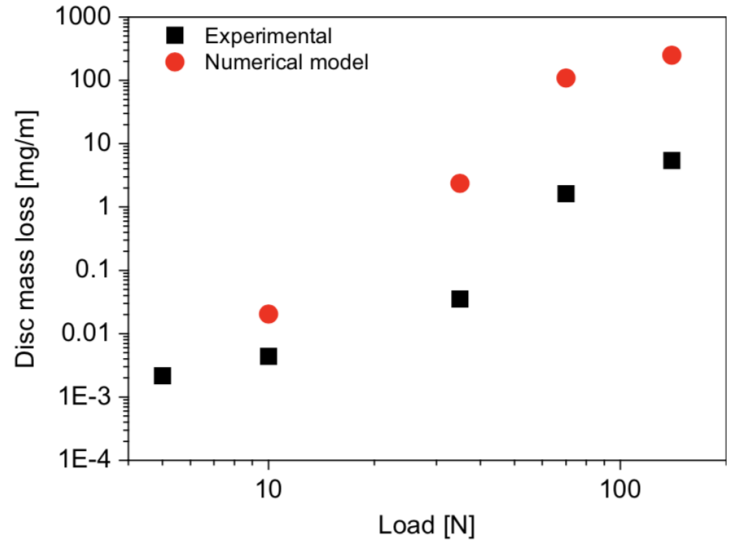

Fig. 10. Comparison between mass losses of experimental and numerical results after the sliding wear.

Numerical Model of Machining Considering the Effect of MnS Inclusions in an Austenitic Stainless Steel

G.M.P.Chagas I.F.Machado
https://doi.org/10.1016/j.procir.2015.04.093

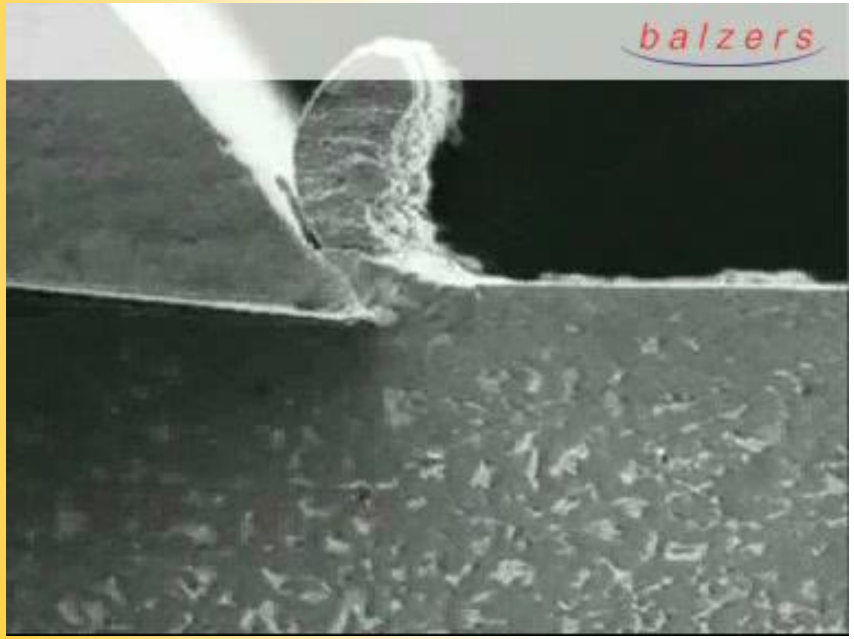

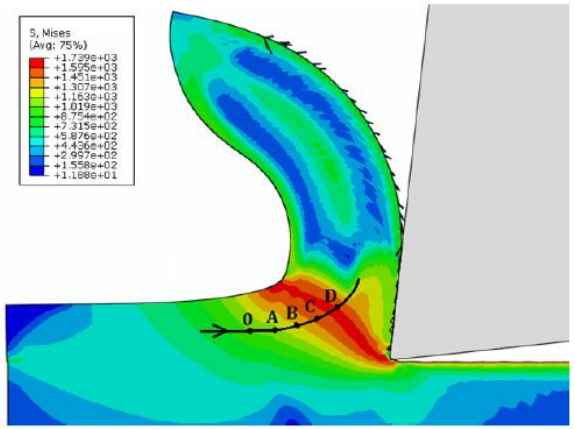

Fig. 4. Von Mises stress with positions evaluated along the flow line

Table 4. Maximum and minimum plane stress

Distance	σ_1 (MPa)	σ_2 (MPa)
0-A	59	-1267
A-B	118	-1229
B-C	470	-1151
C-D	615	-1187

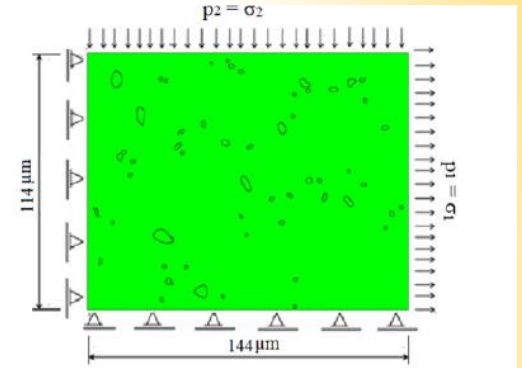

Fig.7. Microstructure boundary conditions and loads applied

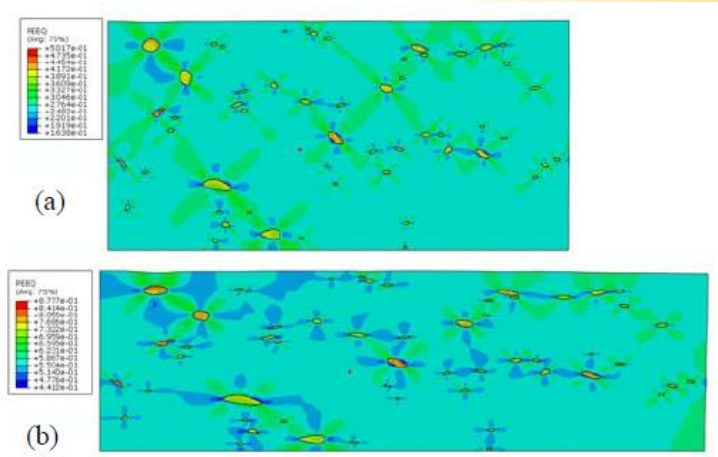

Fig. 11 Equivalent plastic strain behavior:
(a) in the instant time of 8.083 x10^{-5}s, (b) instant of time of 2.546x10^{-4}s.

Phenomena – Abrasion, 2D analysis

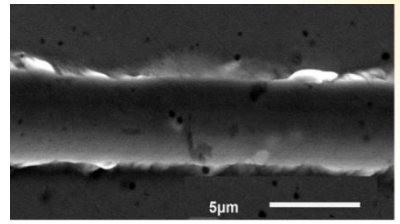

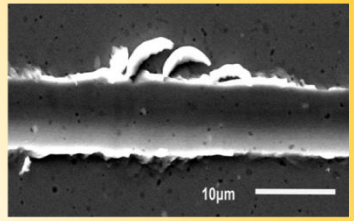

Chip formation mechanism during cutting: When the scalar stiffness degradation is unity, the material failure will occur promoting debris such as discontinuous chips agreement with the experimental results.

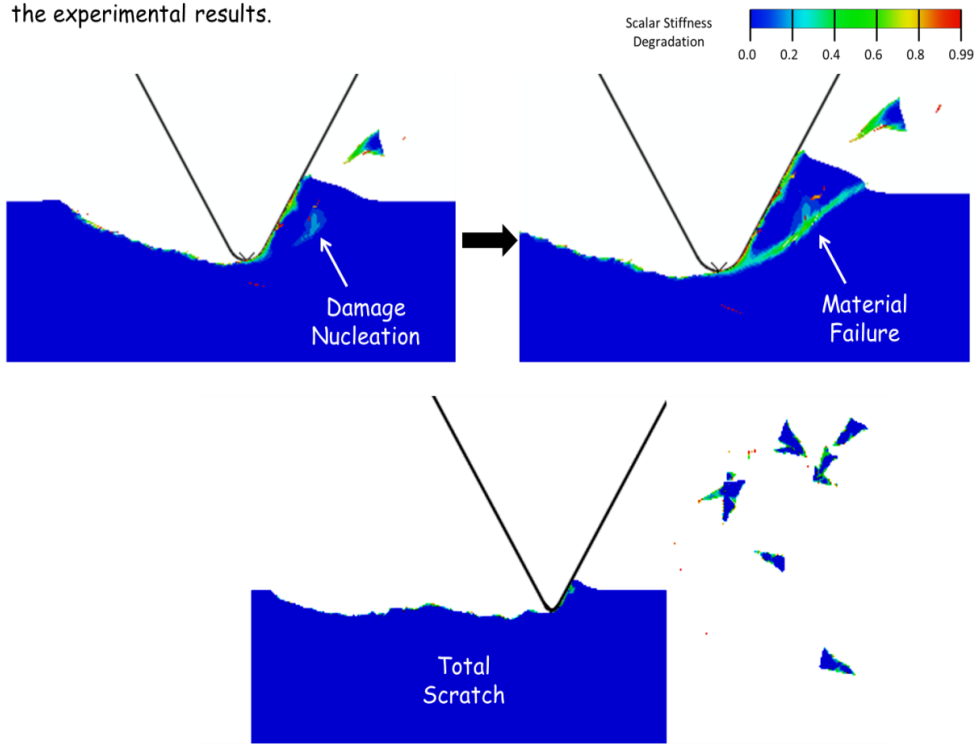

50 mN - Mechanism Transition

100 mN - Cutting

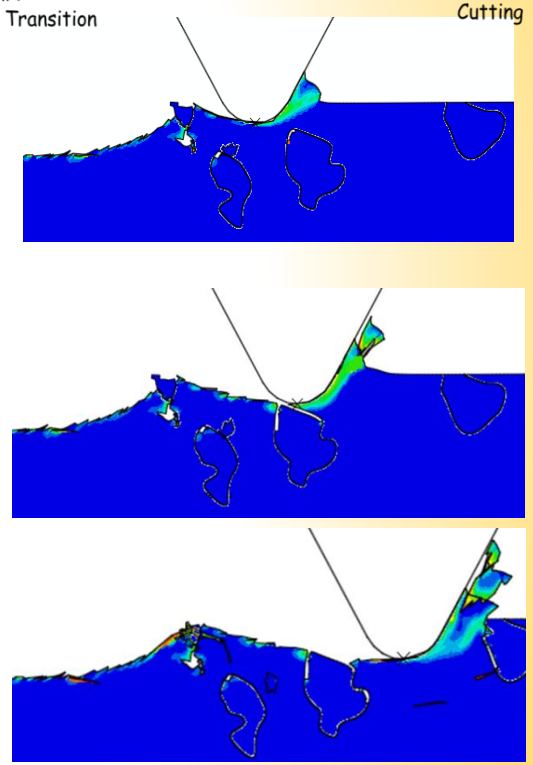

Homogeneous material

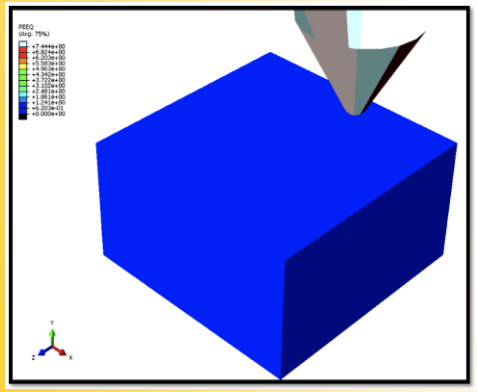

Analysis of abrasion mechanisms in the AISI 303 stainless steel: Effect of deformed layer

V. Seriacopi, N. K. Fukumasu, R. M. Souza, I. F. Machado

10.1016/j.procir.2016.02.326

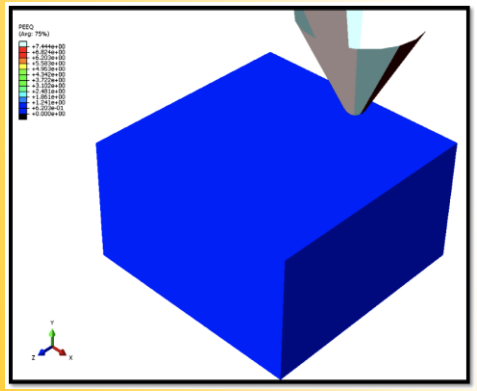

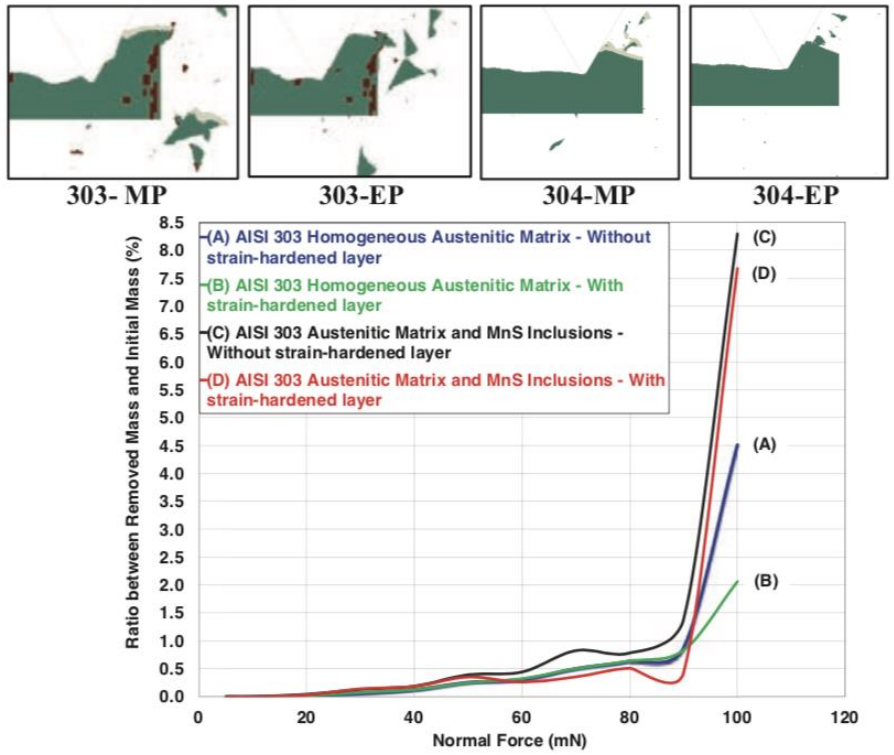

Fig. 6. Numerical results of mass removal by abrasion, obtained considering difference in surface finishing and microstructure.

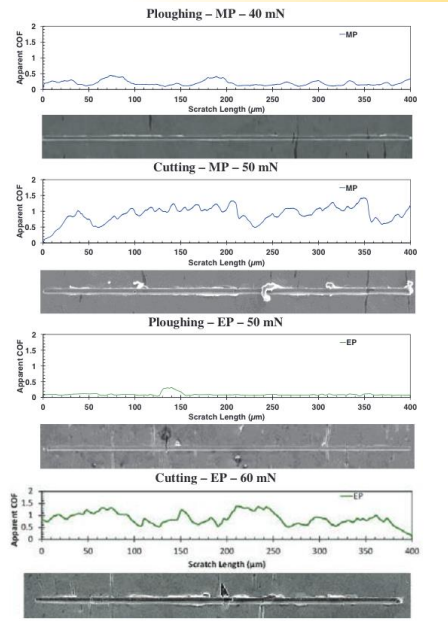

Fig. 4. Abrasion mechanism transitions characterized by SEM (secondary electrons).

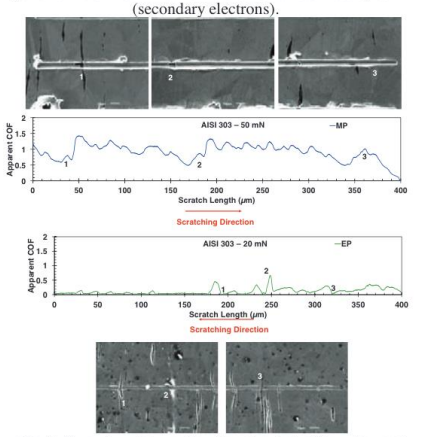

Fig. 5. Experimental results of scratch test at the microscale: details of AISI 303 microstructural behavior.

Izabel Machado – machadoi@usp.br

Vanessa Seriacopi. Evaluation of abrasive mechanisms in metallic alloys during scratch tests: a numerical-experimental study in micro-scale. 2017.

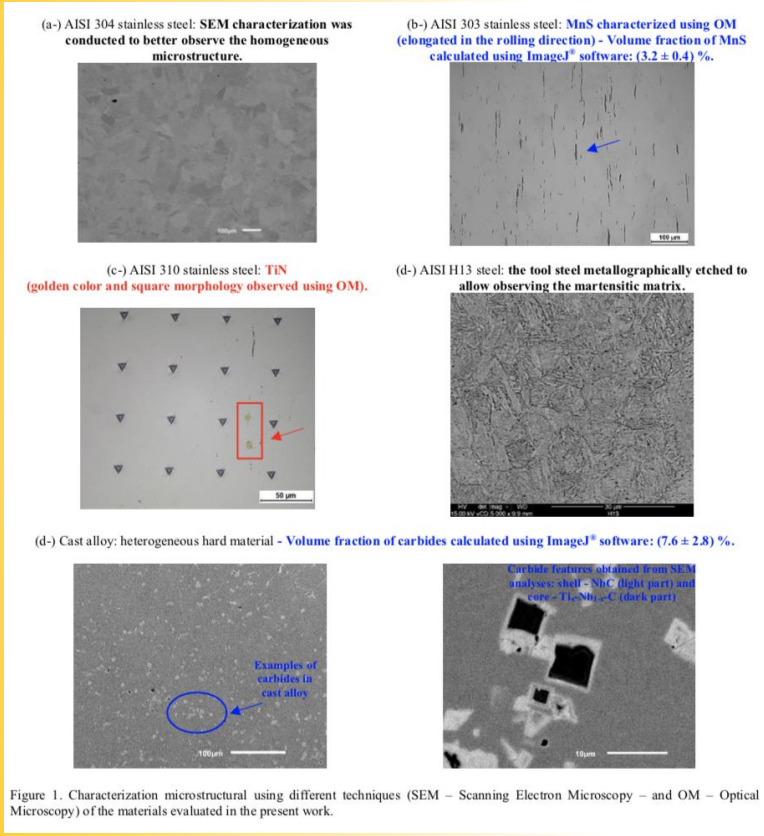

Figure 1. Characterization microstructural using different techniques (SEM – Scanning Electron Microscopy – and OM – Optical Microscopy) of the materials evaluated in the present work.

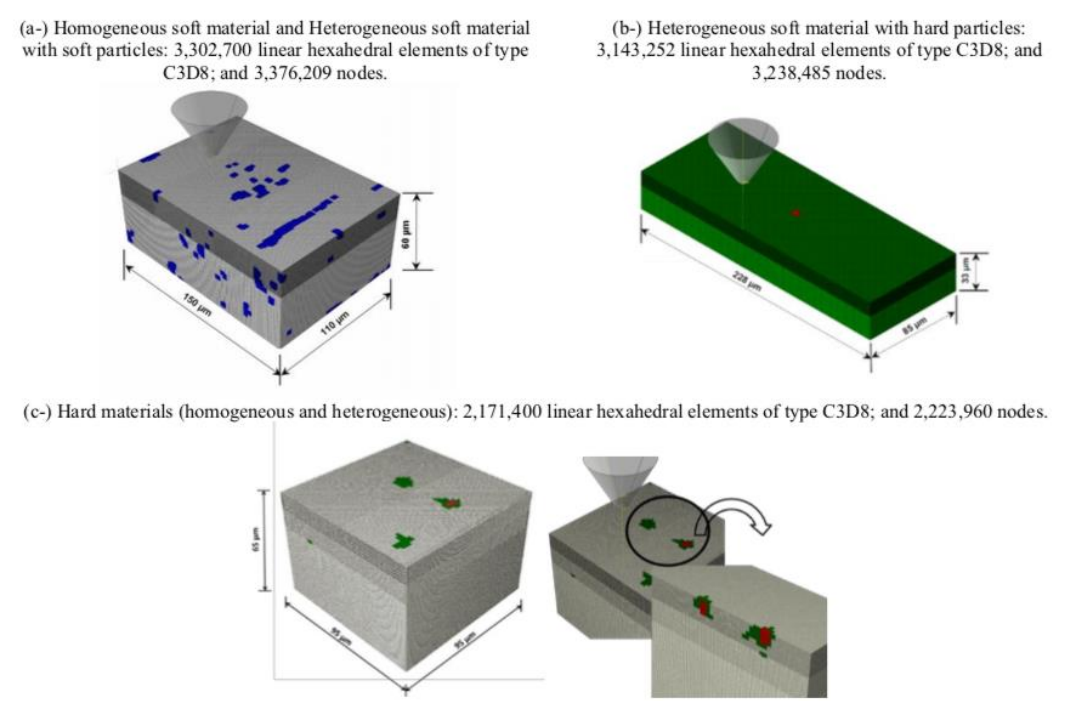

Figure 2. Finite element meshes generated from the microstructures of the materials studied: (a-) details of the heterogeneous soft material with soft precipitates (Group 2), composed by austenitic matrix and manganese sulfides; and (b-) heterogeneous soft material with hard precipitate (Group 3): austenitic matrix and titanium nitride; (c-) details of the heterogeneous hard material (Group 5), composed by martensitic matrix and niobium carbides, which are divided into a shell (in green – rich in Nb) and a core (in red – rich in Ti) [16].

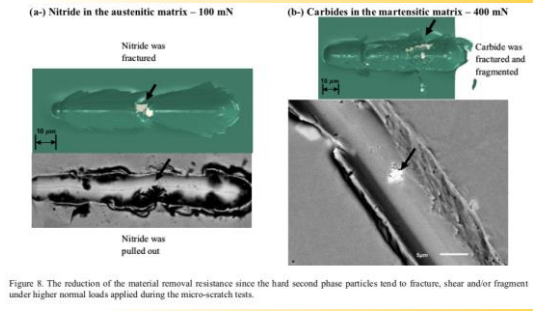

Figure 8. The reduction of the material removal resistance since the hard second phase particles tend to fracture, shear and/or fragment under higher normal loads applied during the micro-scratch tests.

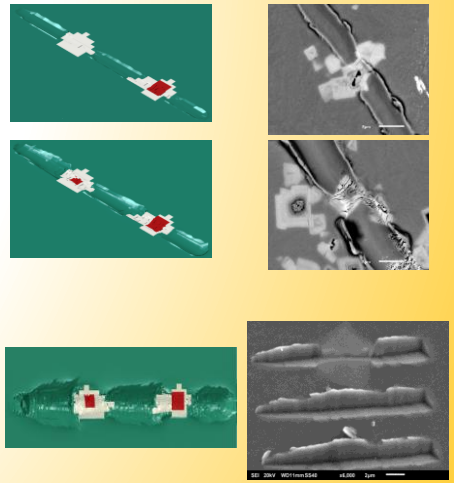

Vanessa Seriacopi. Evaluation of abrasive mechanisms in metallic alloys during scratch tests: a numerical-experimental study in micro-scale. 2017.

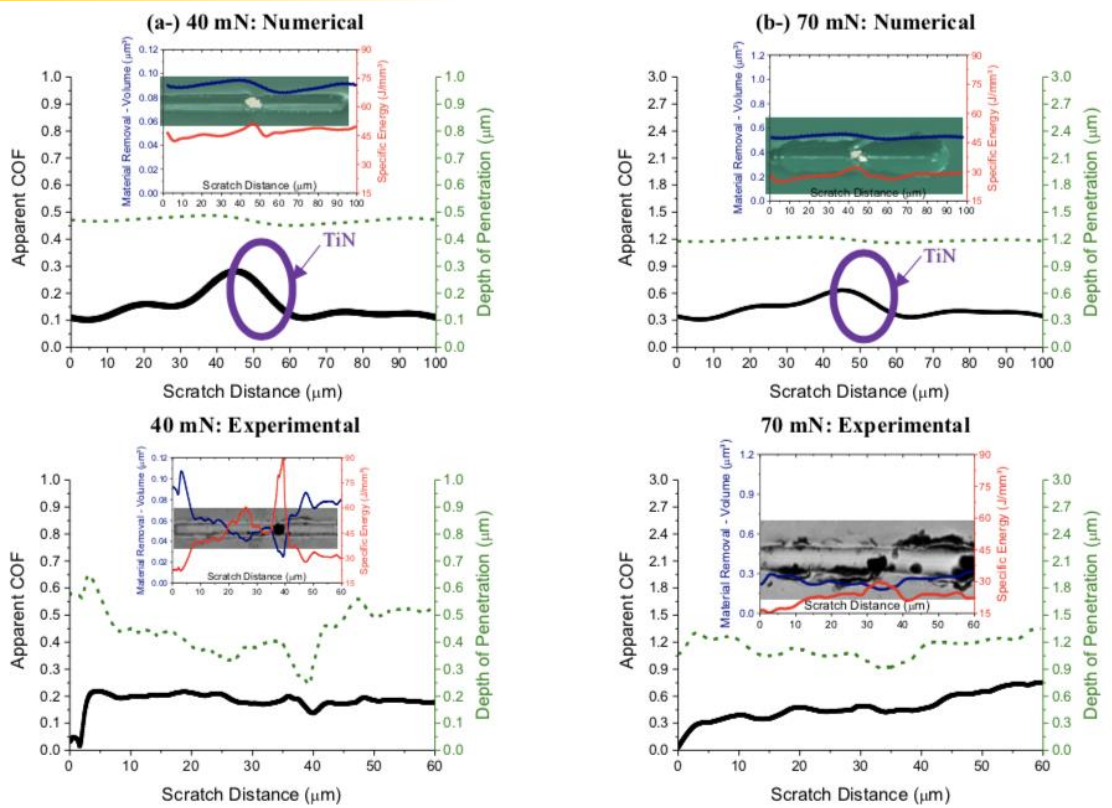

Figure 3. Particle abrasive - heterogeneous soft material with hard second phase (group 3) contact pair: numerical and experimental results of the apparent coefficient of friction, depth of penetration, material removal and specific energy along the scratch length, based on different normal load conditions: (a-) 40 mN; and (b-) 70 mN.

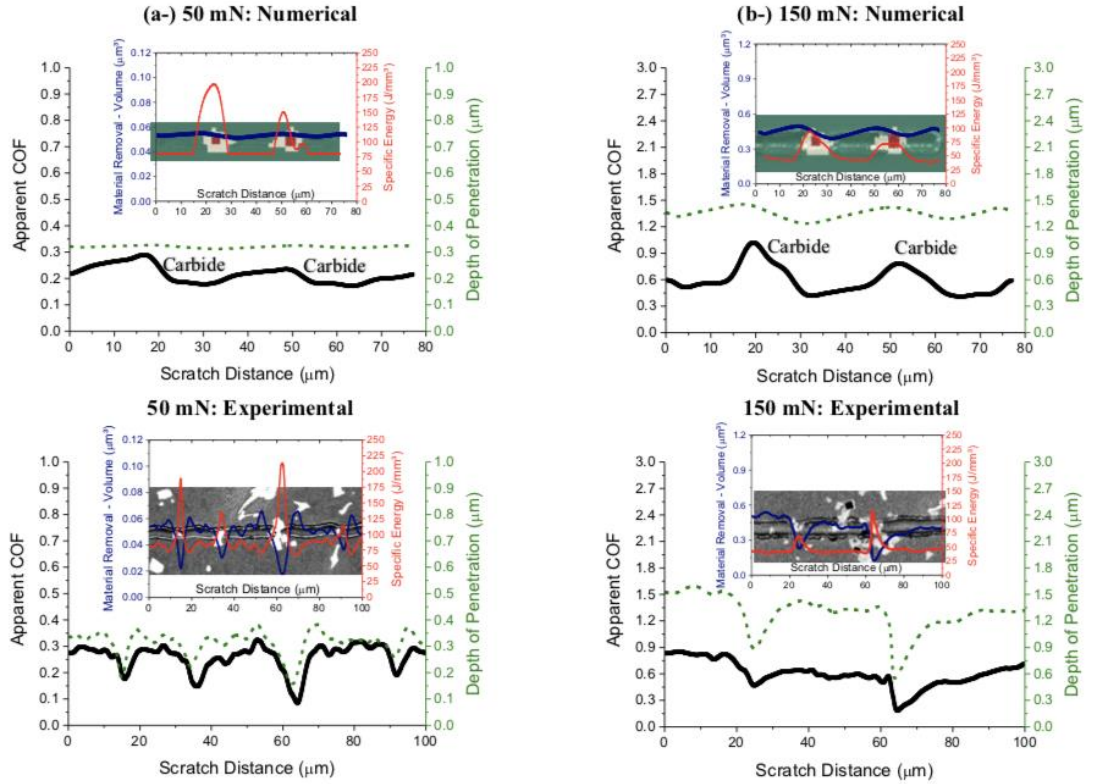

Figure 4. Particle abrasive - heterogeneous hard material (group 5) contact pair: numerical and experimental results of the apparent coefficient of friction, depth of penetration, material removal and specific energy along the scratch length, based on different normal load conditions: (a-) 50 mN; and (b-) 150 mN.

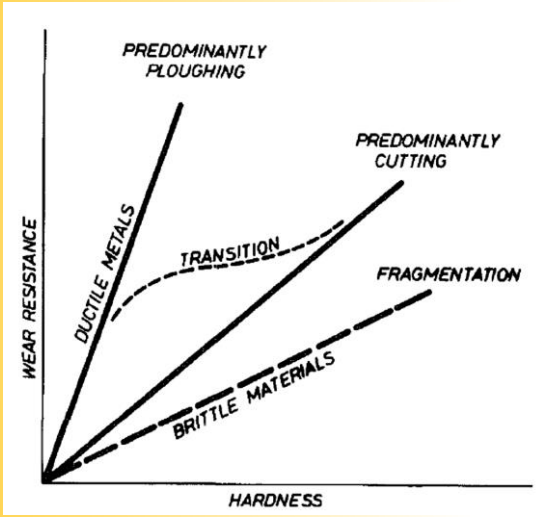

(MURRAY; MUTTON; WATSON, 1979)

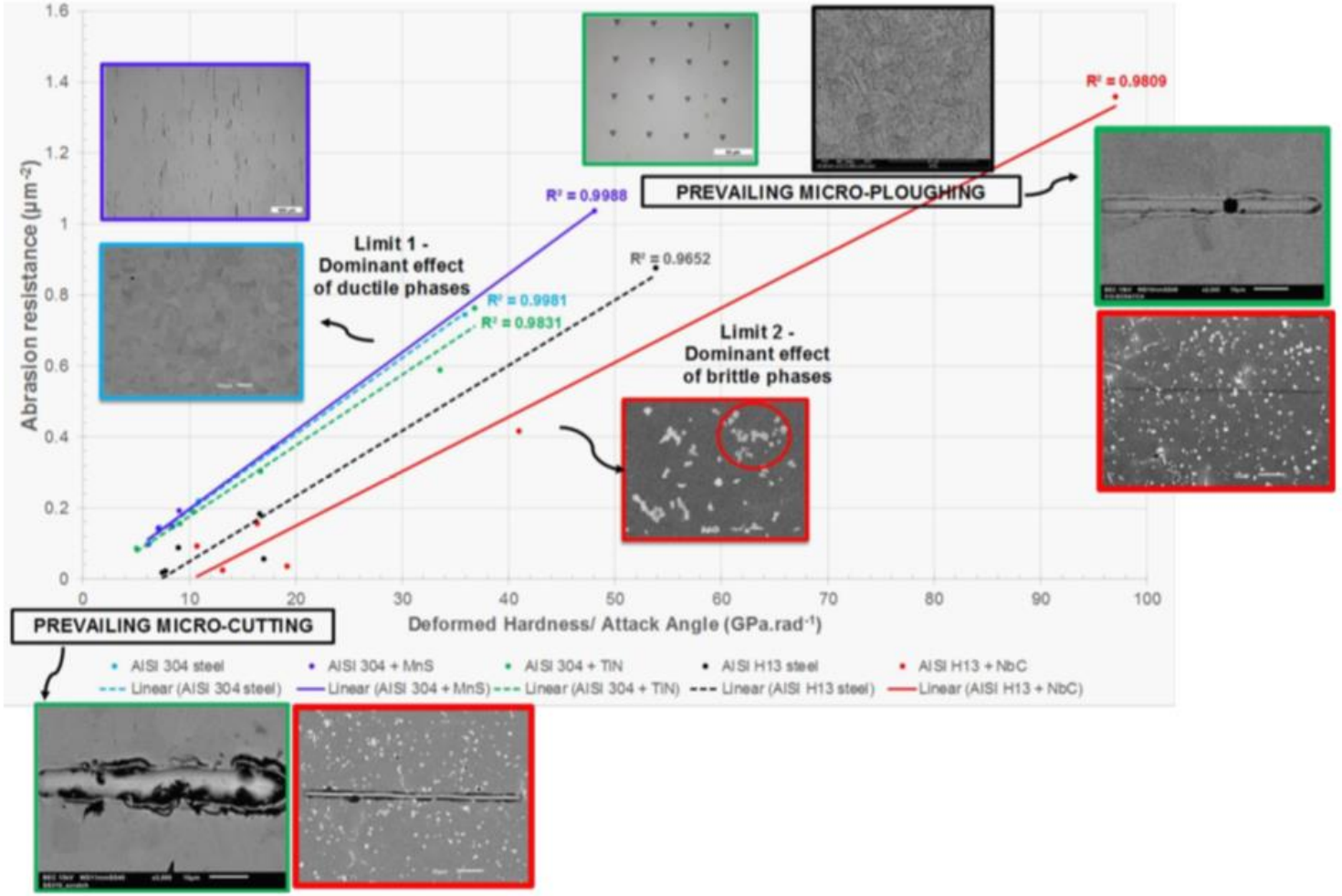

Figure 10. Quantitative map developed from the numerical results, in which frontiers can be delineated to determine the dominant ductile or brittle features (mechanical and damage behavior), and the prevailing abrasive micro-mechanism: abrasion resistance as a function of H_{def}/Attack Angle.

Study of angular cutting conditions using multiple scratch tests onto low T carbon steel: An experimental-numerical approach

V. Seriacopi, S. Mezghani, S. Crequy, I.F. Machado, M. El Mansori, R.M. Souza, Wear
https://doi.org/10.1016/j.wear.2019.01.101

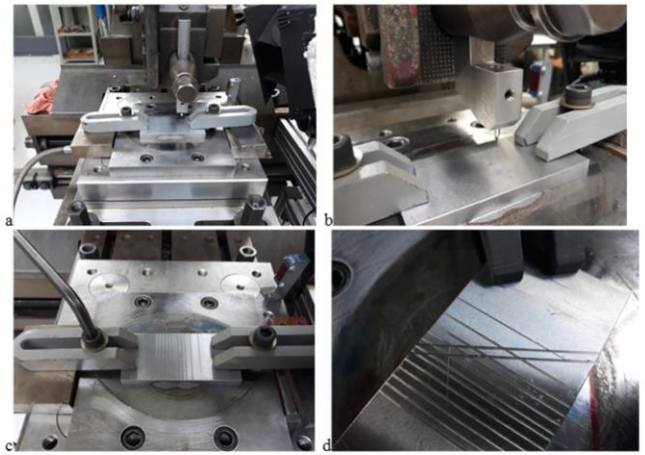

Fig. 1. Experimental setup of the scratch tests onto the 1020 steel conducted in the sequence a-d. Parallel scratches were carried out (a-c) and later a second set of parallel scratches was run at a specific angle (10, 20 or 30°) with respect to the previous one (d).

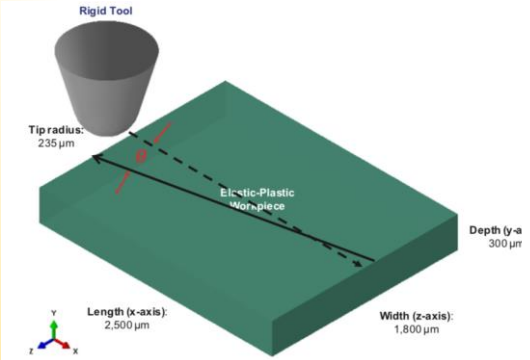

Fig. 2. Numerical modelling created to study the angled scratches. The following successive steps can be predicted here: (i-) first scratch due to the tool movement along x-direction; (ii-) tool moving along z-direction; and finally (iii-) angular scratches in the x-z plane (θ = 10, 20 and 30°), resulting in a V-shape or a X-shape depending on the angle and the consequent final scratch length.

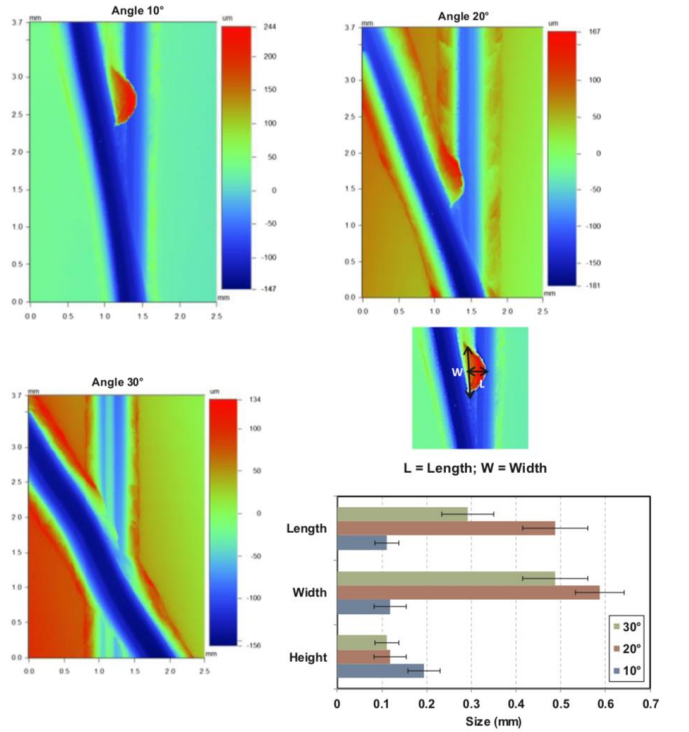

Fig. 5. Experimental results: topography characterization for all orientations. The burr features – length, width and height - are also displayed h

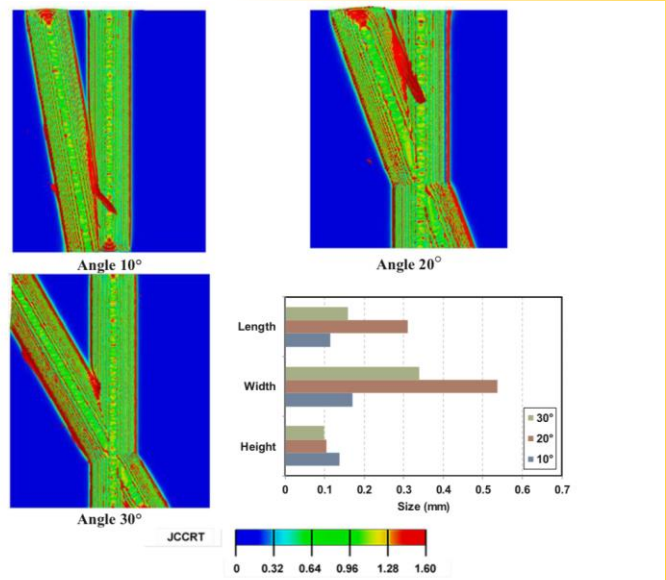

Fig. 6. Numerical results: Equivalent plastic strain at the onset of the fracture, defined by the Johnson-Cook damage criterion (JCCRT) for all orientations. The burr features – length, width and height – obtained from the numerical analyses are available here.

Study of angular cutting conditions using multiple scratch tests onto low T carbon steel: An experimental-numerical approach

V. Seriacopi, S. Mezghani, S. Crequy, I.F. Machado, M. El Mansori, R.M. Souza, Wear
https://doi.org/10.1016/j.wear.2019.01.101

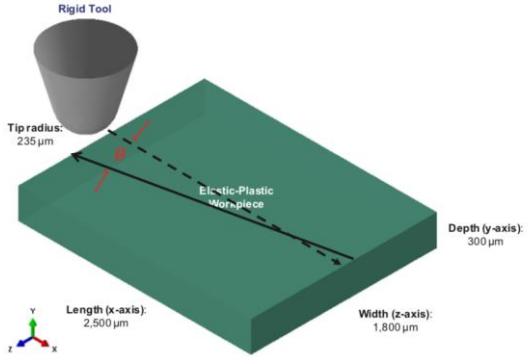

Fig. 2. Numerical modelling created to study the angled scratches. The following successive steps can be predicted here: (i-) first scratch due to the tool movement along x-direction; (ii-) tool moving along z-direction; and finally (iii-) angular scratches in the x-z plane (θ = 10, 20 and 30°), resulting in a V-shape or a X-shape depending on the angle and the consequent final scratch length.

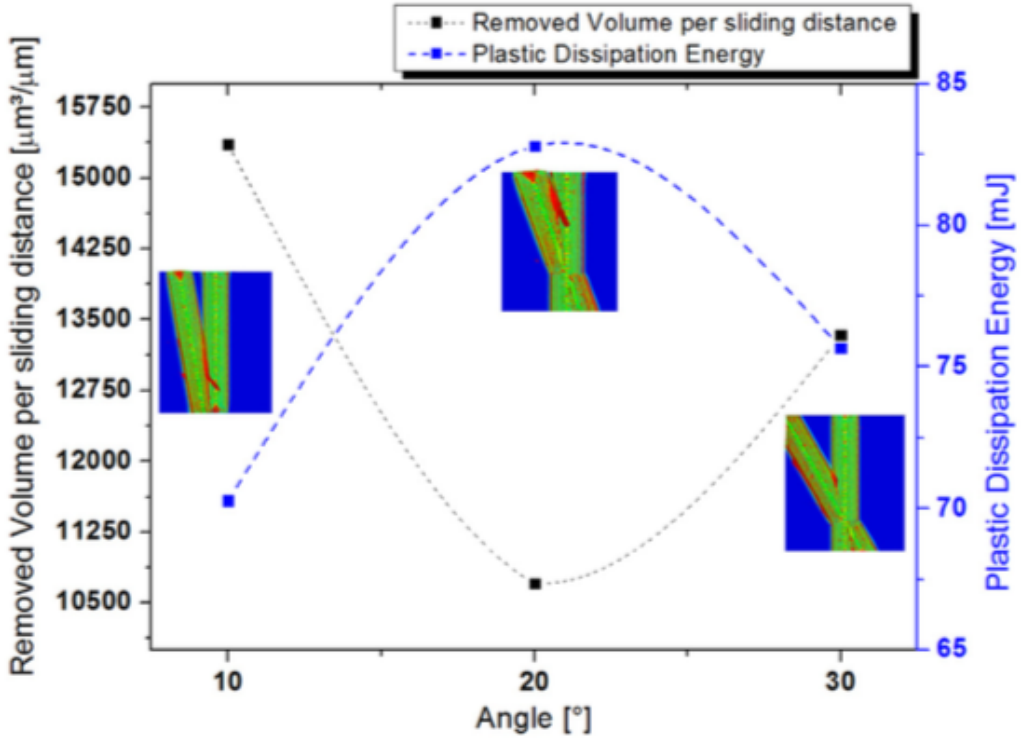

Fig. 7. Numerical results of the material removal and plastic dissipation energy as a function of the orientation of the angular scratch.

Numerical analyses of stress induced damage during a reciprocating lubricated test of FeCMo SPS sintered alloy

N.K.Fukumasu, G.Boidi, V.Seriacopi, G.A.A.Machado, R.M.Souza, I.F.Machado, Tribology International

https://doi.org/10.1016/j.triboint.2016.12.025

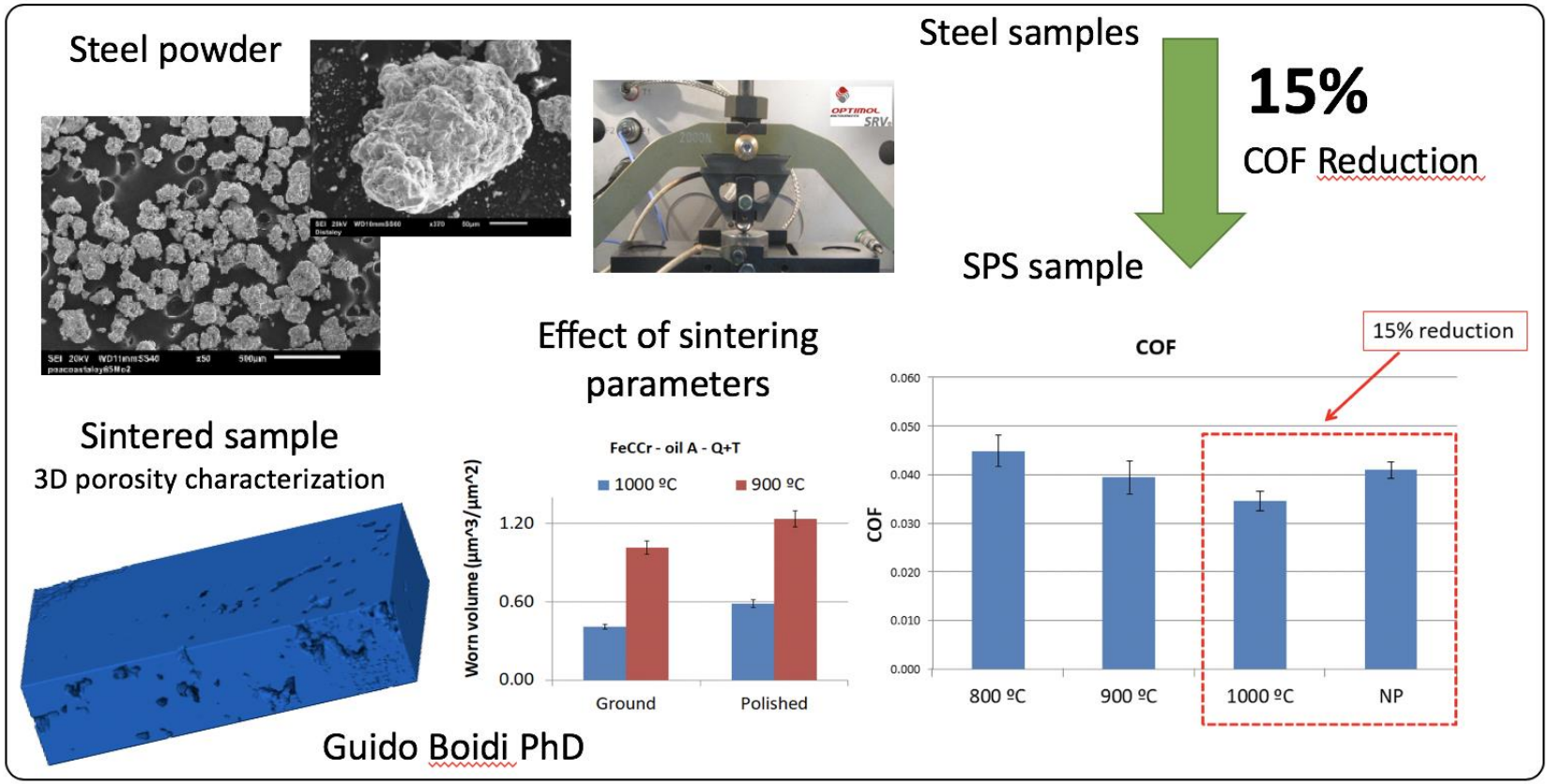

Numerical analyses of stress induced damage during a reciprocating lubricated test of FeCMo SPS sintered alloy

N.K.Fukumasu, G.Boidi, V.Seriacopi, G.A.A.Machado, R.M.Souza, I.F.Machado, Tribology International

https://doi.org/10.1016/j.triboint.2016.12.025

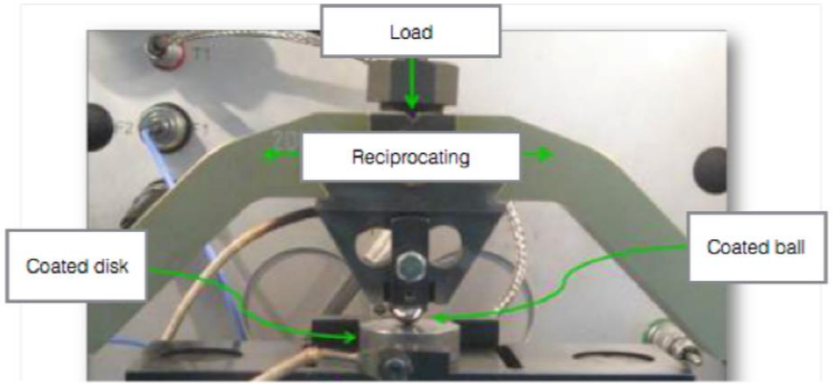

Fig. 1. Macroscale reciprocating test configuration analyzed in this work, in which both sphere and disk were coated.

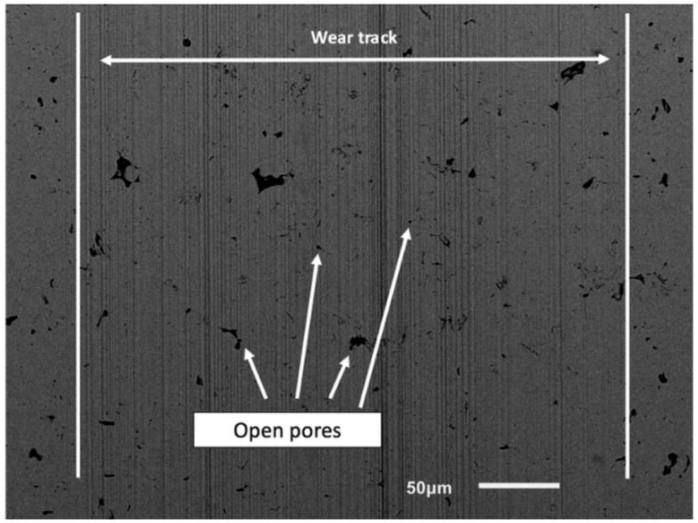

Fig. 5. Back scattered SEM image of the wear track from the experimental reciprocating test with contact pressure of 2.5 GPa.

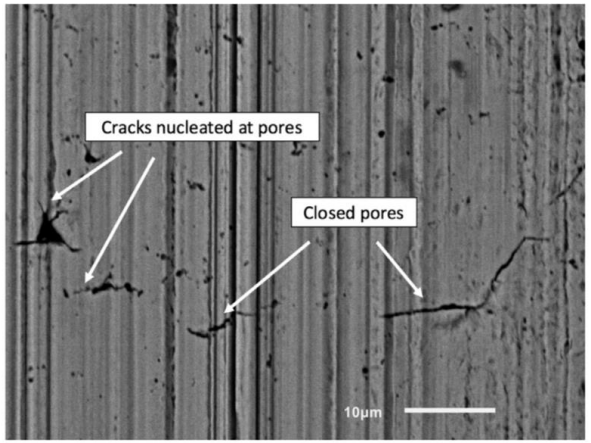

Fig. 8. Higher magnification of the back scattered SEM image of the white ellipses in Fig. 7.

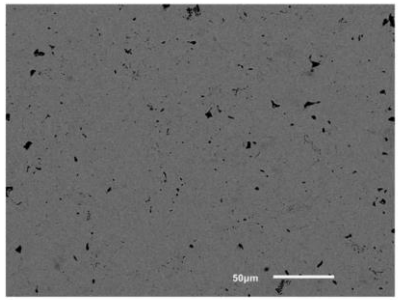

Fig. 3. Back scattered SEM image of the sintered FeCMo material presenting less than 2% porosity.

Numerical analyses of stress induced damage during a reciprocating lubricated test of FeCMo SPS sintered alloy

N.K.Fukumasu, G.Boidi, V.Seriacopi, G.A.A.Machado, R.M.Souza, I.F.Machado, Tribology International

https://doi.org/10.1016/j.triboint.2016.12.025

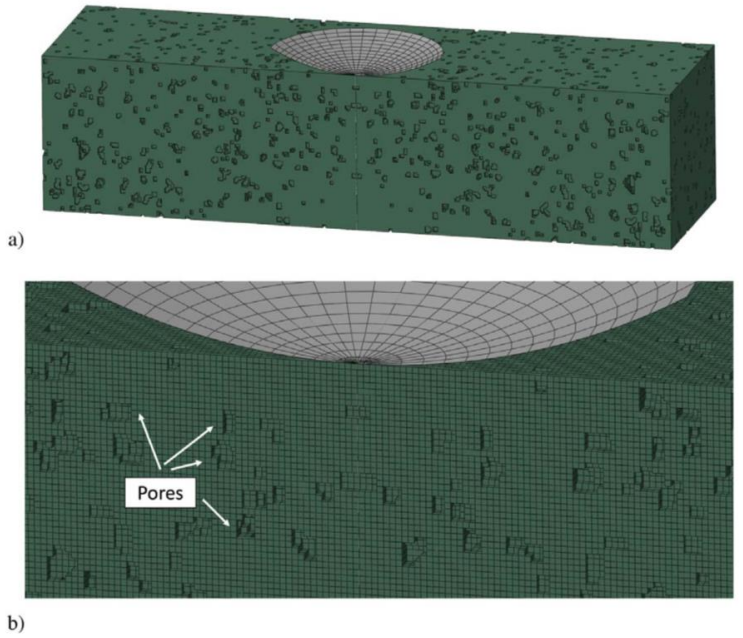

Fig. 1. Computational domain for the reciprocating test analyses: a) system composed by an analytical rigid sphere (gray) and a plane counterbody (dark green); b) detail of the system indicating the porosity represented as small voids (regions without elements) in the numerical mesh. (For interpretation of the references to color in this figure legend, the reader is referred to the web version of this article.)

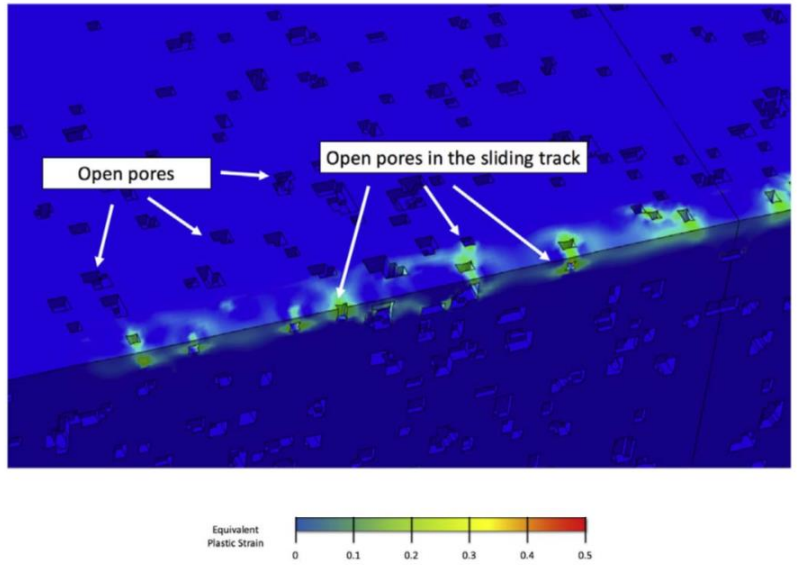

Fig. 4. Localized plastic deformation induced by the pores during the sliding of the sphere. The color field indicate the level of plastic deformation.

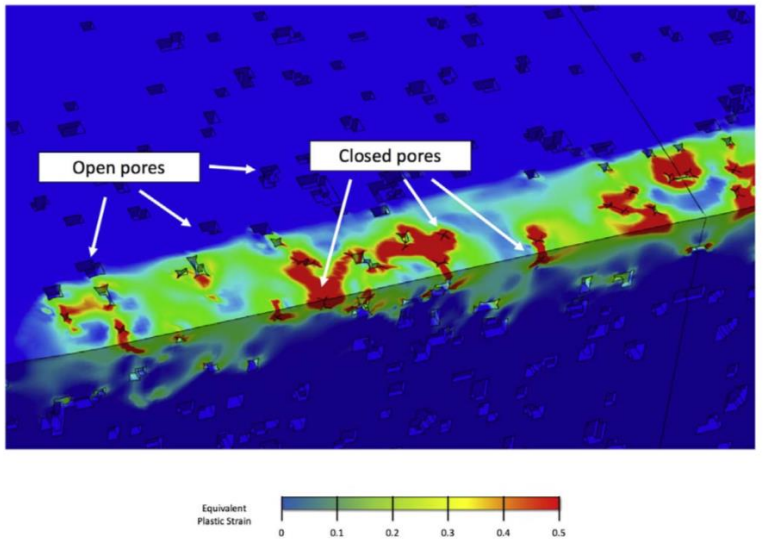

Fig. 6. Collapse of the pores by the plastic deformation during the sliding of the sphere. The color field indicate the level of plastic deformation and red regions indicate plastic deformation higher than 50%.

Numerical analyses of stress induced damage during a reciprocating lubricated test of FeCMo SPS sintered alloy

N.K.Fukumasu, G.Boidi, V.Seriacopi, G.A.A.Machado, R.M.Souza, I.F.Machado, Tribology International

https://doi.org/10.1016/j.triboint.2016.12.025

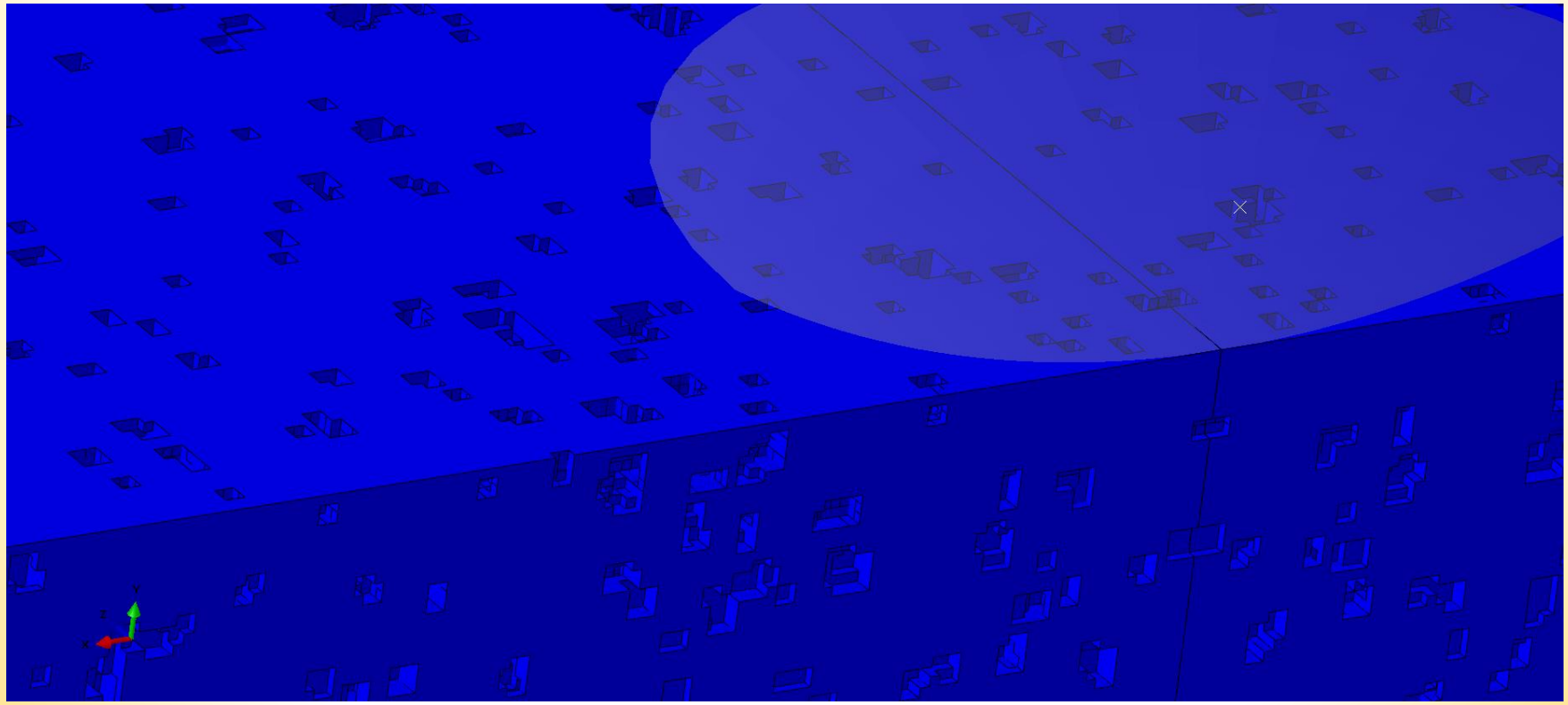

Numerical analyses of stress induced damage during a reciprocating lubricated test of FeCMo SPS sintered alloy

N.K.Fukumasu, G.Boidi, V.Seriacopi, G.A.A.Machado, R.M.Souza, I.F.Machado, Tribology International

https://doi.org/10.1016/j.triboint.2016.12.025

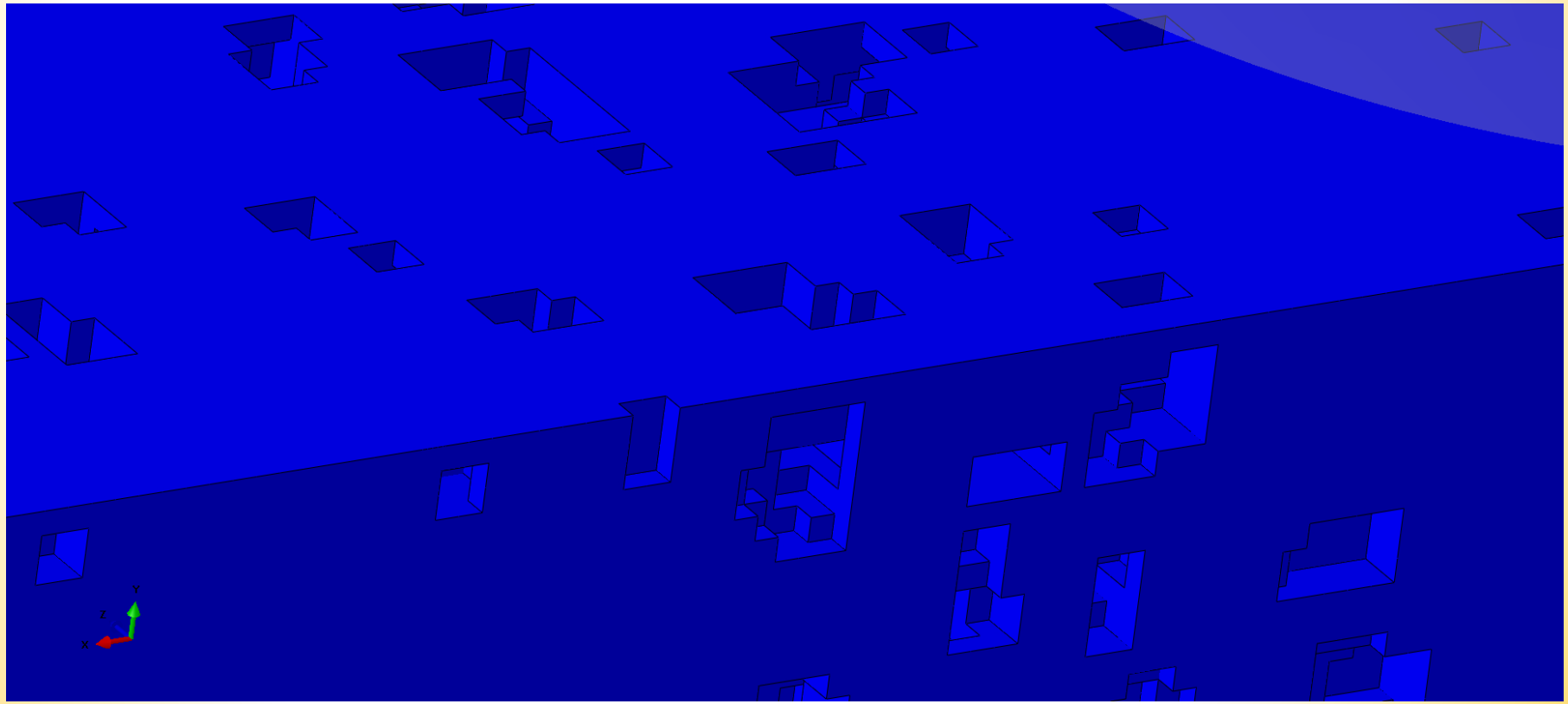

Influence of Sintering Parameters on Micro-Scale Mechanical and Tribological Behavior of Niobium Carbides

N.K. Fukumasu, A.J.O.Tertuliano, C.F. Bernardes, V. Seriacopi, R.M. Souza, I.F. Machado

Plansee Seminar - 2017

Motivation: Previous studies to evaluate the mechanical properties and influence on wear of NbC on the AISI H13 steel with 5% volume fraction of NbC –, design of materials and multiscale analysis - evaluate bulk properties

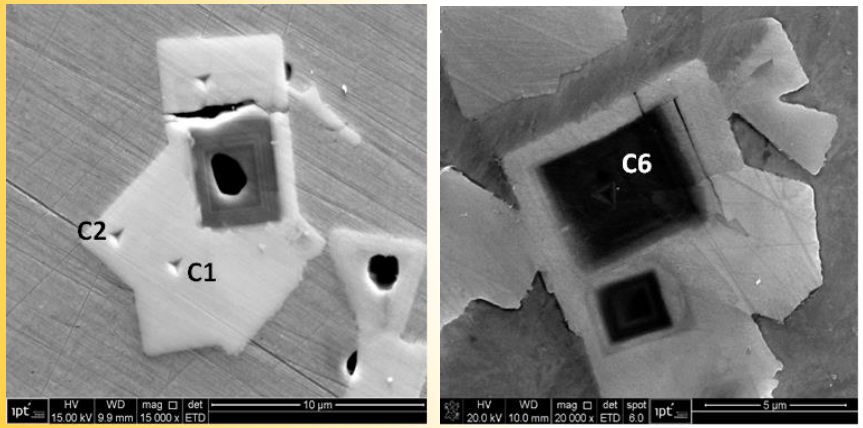

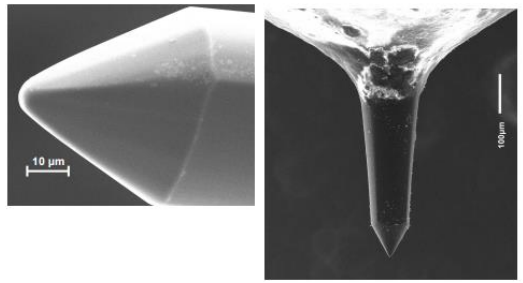

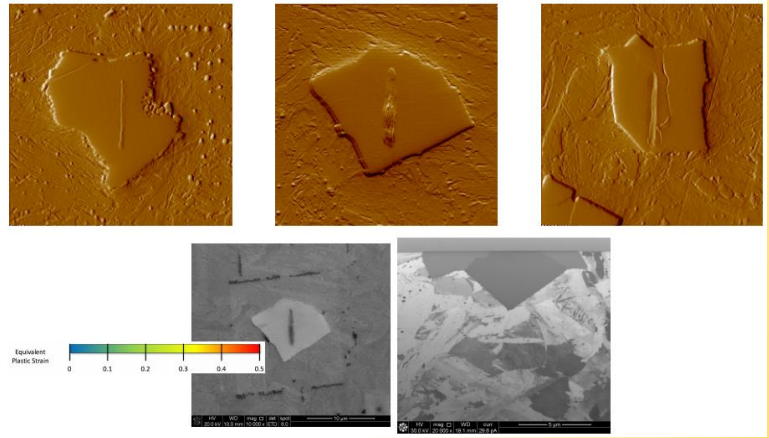

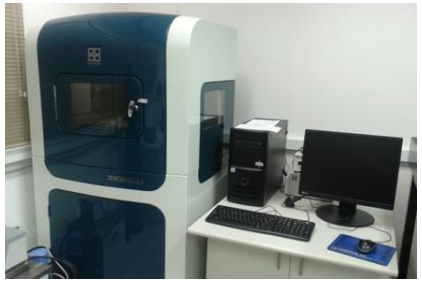

Triboindenter Hysitron - TI950

Influence of Sintering Parameters on Micro-Scale Mechanical and Tribological Behavior of Niobium Carbides

N.K. Fukumasu, A.J.O.Tertuliano, C.F. Bernardes, V. Seriacopi, R.M. Souza, I.F. Machado

Plansee Seminar - 2017

Motivation: Previous studies to evaluate the mechanical properties and influence on wear of NbC on the AISI H13 steel with 5% volume fraction of NbC –, design of materials and multiscale analysis - evaluate bulk properties

Pressure applied during the consolidation was 60MPa of maximum pressure, vacuum range was between 10 and 15 Pa, the average heating rate was 50°C/min, The temperature reached was 1600°C and the holding time

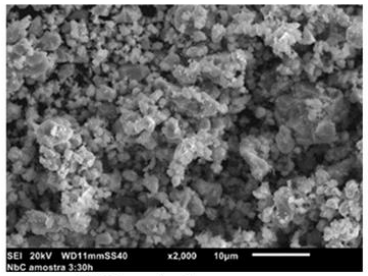

NbC Powder features

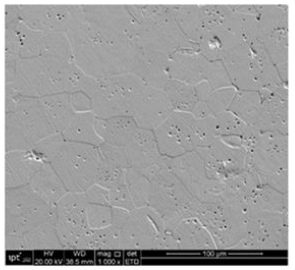

95% densified (7.40 g/cm³)

Pores (FEG-FIB)

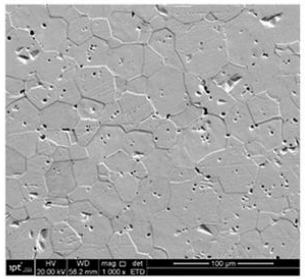

97% densified (7.60 g/cm³)

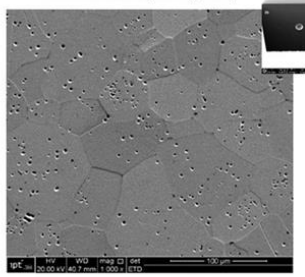

99% densified (7.76 g/cm³)

Fracture

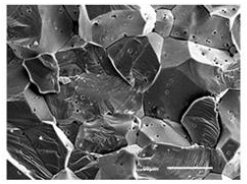

Sample	Holding time (min)	Cooling
NbC95	5	Free cooling in the die
NbC97	10	Free cooling in the die
NbC99	10	100°C/min from 1600°C to 1100°C and free cooling in the die.

Influence of Sintering Parameters on Micro-Scale Mechanical and Tribological Behavior of Niobium Carbides

N.K. Fukumasu, A.J.O.Tertuliano, C.F. Bernardes, V. Seriacopi, R.M. Souza, I.F. Machado

Plansee Seminar - 2017

Wear tests

- Procedure and details of this method development and description can be found elsewhere [E. Broitman, Francisco J. Flores-Ruiz, Journal of Vacuum Science & Technology [A 33], 043201 (2015)
- Wear tests were conducted in different grains after EBDS analysis. Indentation marks were made previously to identify the grains scanned.

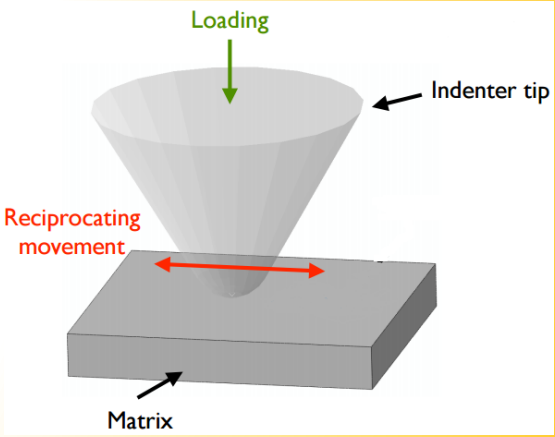

Finite element method simulation

- The Finite Element Method (FEM), using the Abaqus® commercial package, is used to build a 3D
- The numerical simulations have focused on the influence of mechanical and failure properties on the wear behavior of the NbC. An explicit time integration
- Rigid cono-spherical indenter with tip diameter of 10 μm, which is in contact with a square counterbody with 30 μm in length, 30 μm in width and 5 μm in height. (likewise the experimental tests)
- Fracture toughness was selected as 5 MPa $m^{0.5}$, based on the literature that indicates a variation from 2 to 8 MPa $m^{0.5}$

Influence of Sintering Parameters on Micro-Scale Mechanical and Tribological Behavior of Niobium Carbides

N.K. Fukumasu, A.J.O.Tertuliano, C.F. Bernardes, V. Seriacopi, R.M. Souza, I.F. Machado

Plansee Seminar - 2017

Table displays the values of hardness (H), reduced elastic modulus (Er), elastic modulus (E), and the ratio between E and H . Different E porous NbC

Sample	H (GPa)	Er (GPa)	E (GPa)	E/H
NbC95	21.9 ± 1.7	299.7 ± 5.4	**388**	17.7
NbC97	24.1 ± 1.3	362.1 ± 4.0	**506**	20.1
NbC99	23.7 ± 2.1	356.2 ± 2.0	**494**	20.8

Wear

Blue -> analyzed region

Red -> whole curve

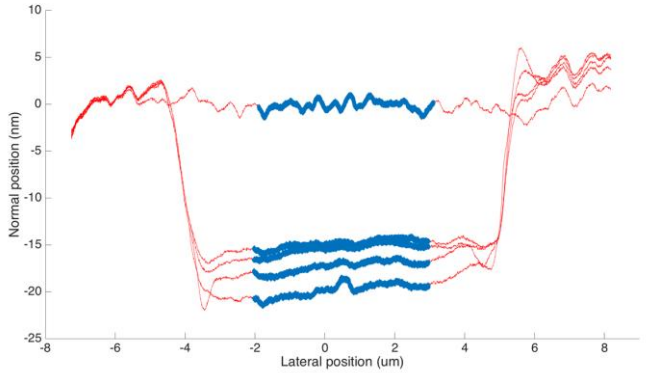

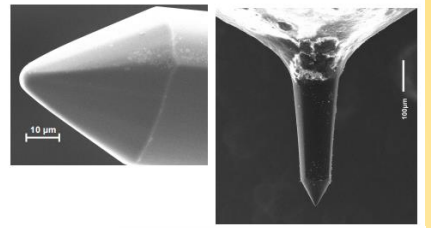

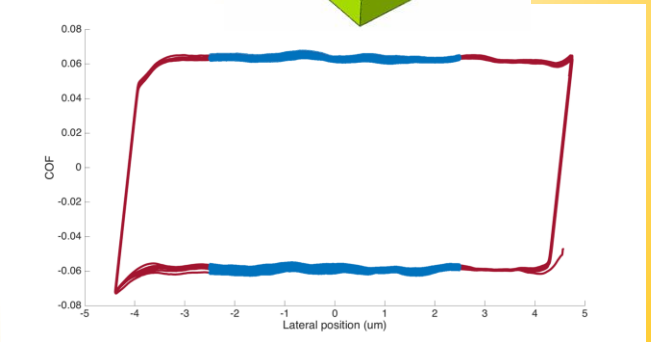

Influence of Sintering Parameters on Micro-Scale Mechanical and Tribological Behavior of Niobium Carbides

N.K. Fukumasu, A.J.O.Tertuliano, C.F. Bernardes, V. Seriacopi, R.M. Souza, I.F. Machado

Plansee Seminar - 2017

Wear

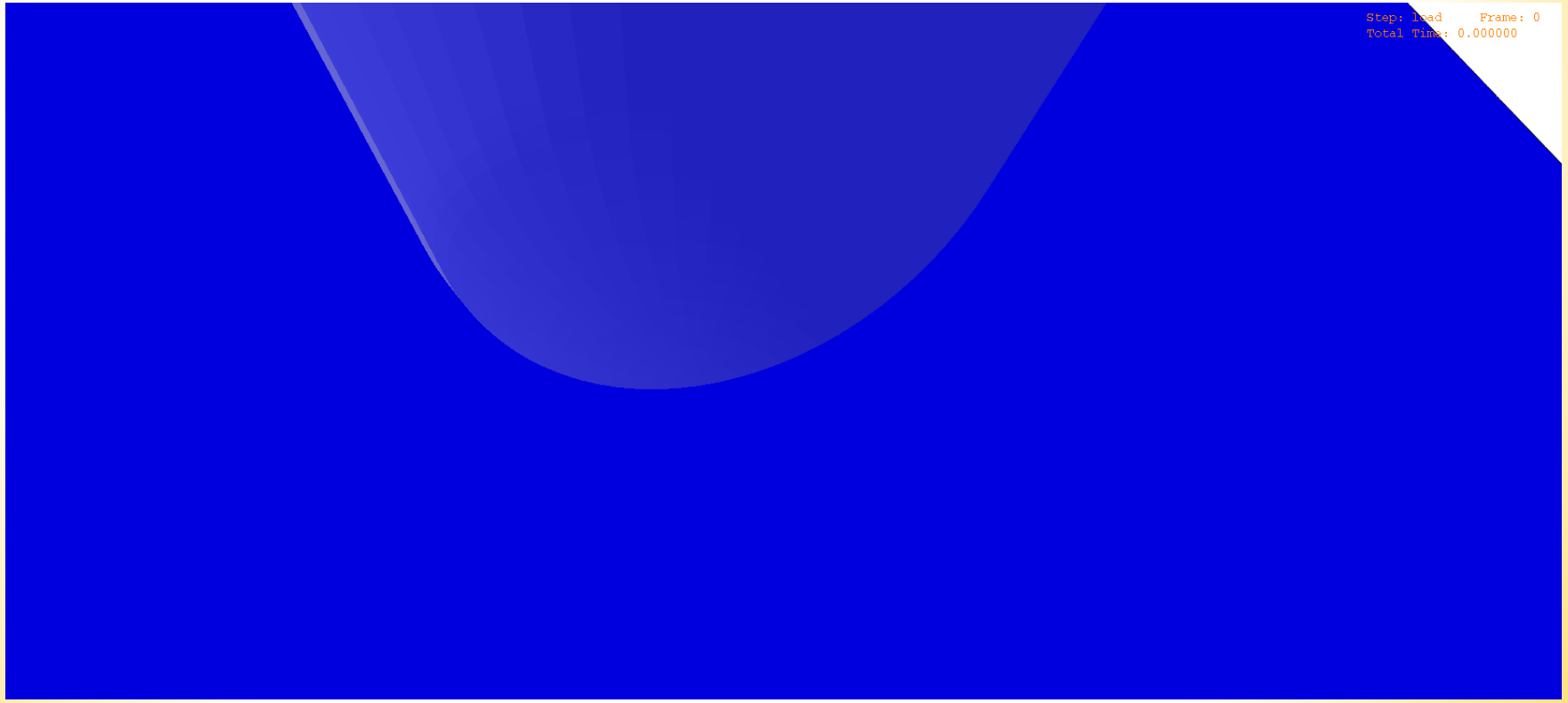

Local transformation of amorphous hydrogenated carbon coating induced by high contact pressure

N.K. Fukumasu, C.F. Bernardes, M.A. Ramirez, V.J. Trava-Airoldi, R.M. Souza, I.F. Machado

Tribology International

https://doi.org/10.1016/j.triboint.2018.04.006

The coating and the interlayer were deposited using a pulsed Direct Current Plasma Enhanced Chemical Vapor Deposition (DC PECVD)

Under dry sliding condition, DLC coated systems may present a reduction of friction force based on the graphitization of the contacting surfaces, as observed by Liu et al. [9]. This phenomenon is related to the re- arrangement of the sp3 and sp2 carbon bonds by energy transferred from the mechanical movement to chemical bond kinetics.

Scratch test on coated systems – sequence of stress states

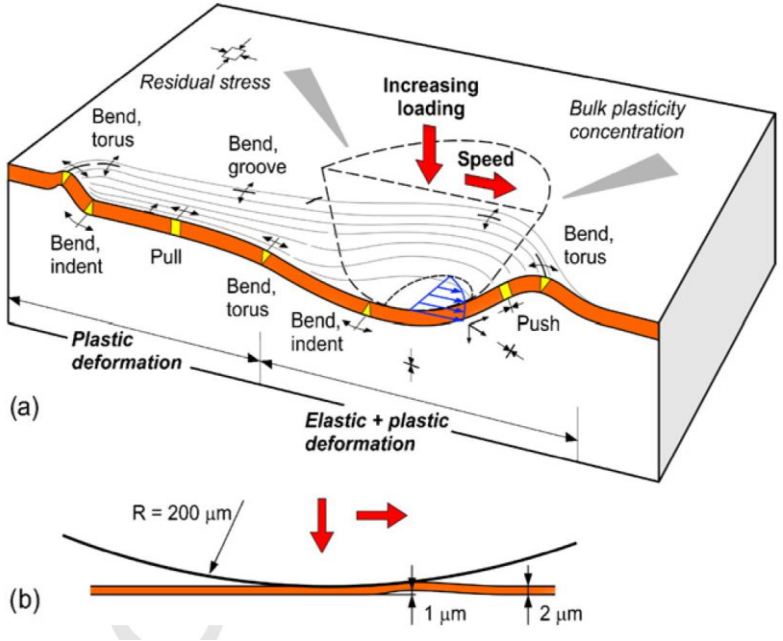

[Holmberg *et al.* Wear 267 (2009) 2142–2156]

Local transformation of amorphous hydrogenated carbon coating induced by high contact pressure

N.K. Fukumasu, C.F. Bernardes, M.A. Ramirez, V.J. Trava-Airoldi, R.M. Souza, I.F. Machado

Tribology International

https://doi.org/10.1016/j.triboint.2018.04.006

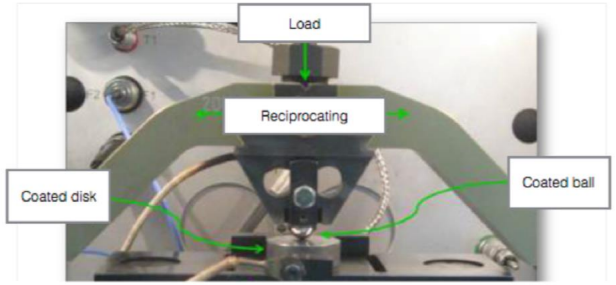

Fig. 1. Macroscale reciprocating test configuration analyzed in this work, in which both sphere and disk were coated.

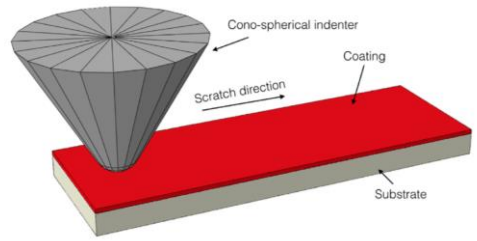

Fig. 2. Numerical model configuration consisting of a cono-spherical tip used to scratch the coated (red) substrate (light gray). (For interpretation of the references to color in this figure legend, the reader is referred to the Web version of this article.)

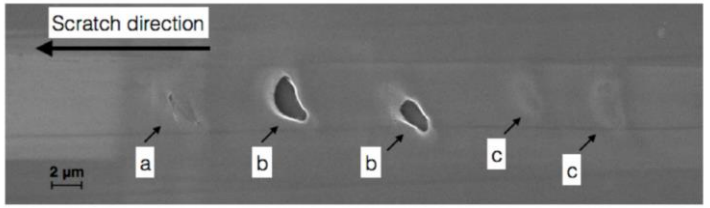

Fig. 8. Microscale scratch track presenting the local typical observed failure modes: a) adhesive and cohesive failures of the coating; b) complete spallation o coating and c) adhesive failure of the coating/substrate interface.

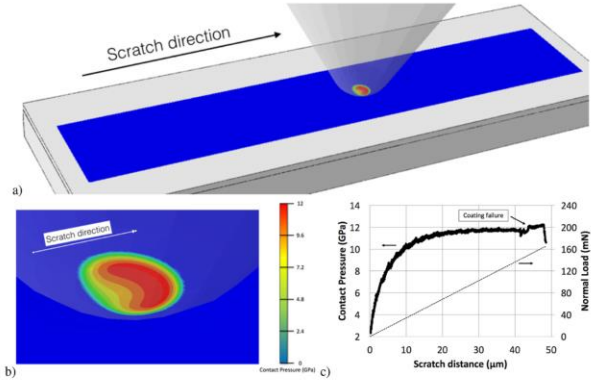

Fig. 14. Contact Pressure at the coating promoted by the indenter movement: a) Instantaneous spatial distribution of the contact pressure; b) detail of the contact region and c) evolution of the contact pressure with the ramping load during the scratch test.

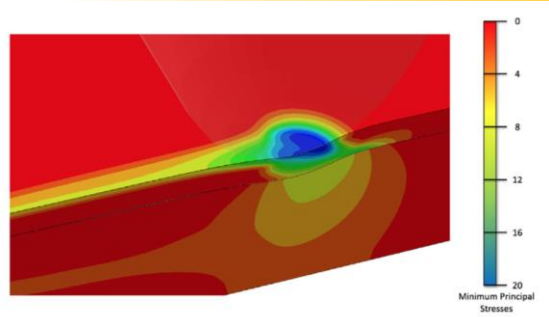

Fig. 15. Minimum Principal Stresses distribution developed inside of the material during the scratch test.

Local transformation of amorphous hydrogenated carbon coating induced by high contact pressure

N.K. Fukumasu, C.F. Bernardes, M.A. Ramirez, V.J. Trava-Airoldi, R.M. Souza, I.F. Machado , Tribology International

https://doi.org/10.1016/j.triboint.2018.04.006

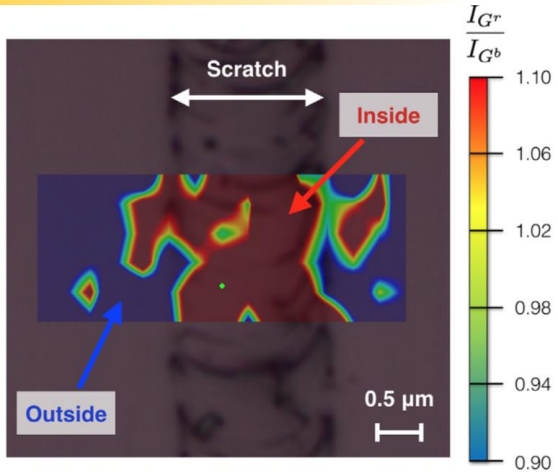

Fig. 9. Superimposed Raman spectroscopy map of I_{G^r}/I_{G^b} ratio on the scratch track of Fig. 8. Higher ratio values (red colored regions) indicate a red-shift of the G band. (For interpretation of the references to color in this figure legend, the reader is referred to the Web version of this article.)

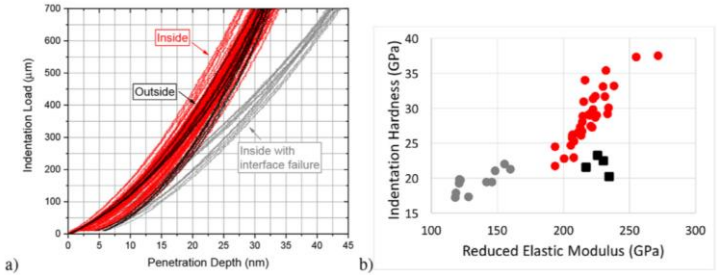

Fig. 6. Nano-indentation measurements of the coating: a) nano-indentation curves for inside (red and gray lines) and outside (black lines) of the wear track; b) results for hardness and reduced elastic modulus of the coating for inside (circles) and outside (squares) of the wear track. Red circles indicate similar reduced elastic modulus but higher hardness compared to outside measurements (black squares), while gray circles indicate a reduction on both characteristics. (For interpretation of the references to color in this figure legend, the reader is referred to the Web version of this article.)

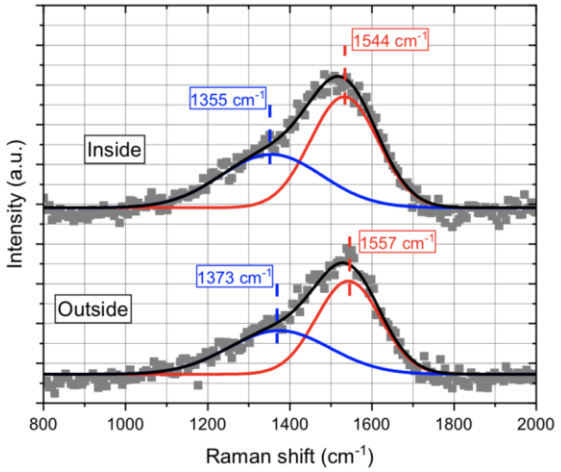

Fig. 10. Raman spectroscopy analysis of a-C:H coatings after the scratch test. Gray squares indicate typical spectra obtained for inside and outside the scratched regions, while lines indicate the deconvolution of the Raman spectra into D (blue) and G (red) bands. (For interpretation of the references to color in this figure legend, the reader is referred to the Web version of this article.)

Numerical simulation indicates high contact pressure (>12GPa) developed at the surface and high internal stresses, ranging from 20 GPa to 12 GPa, are developed along coating thickness. The increase on indentation hardness inside the scrat- ched region are compatible with the nucleation of sp3 carbon bond sites derived from sp2 bonds.

Scales – Molecular Dynamics

- Attempts to analyze the effect of hardness - defects
- Indentation and sliding in previously deformed aluminum slab

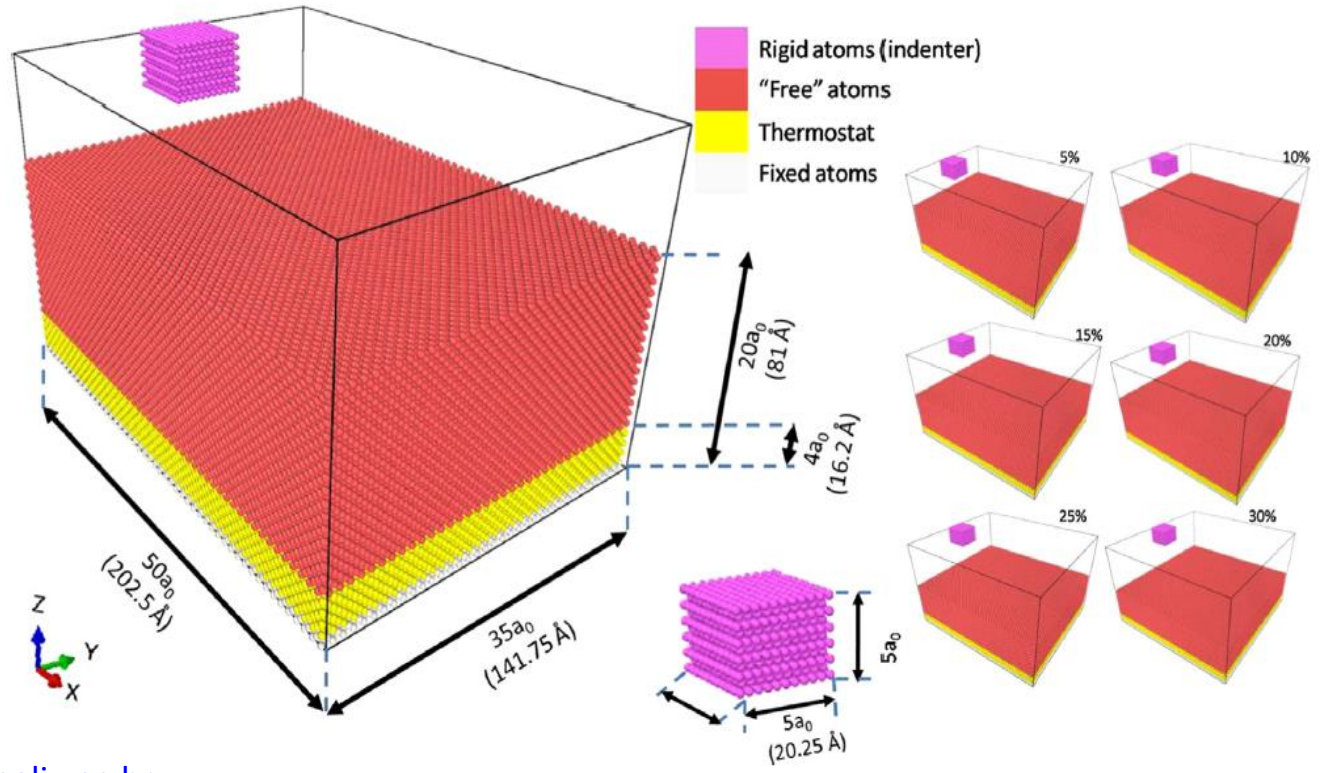

roberto.souza@poli.usp.br

[Bortoleto *et al.*, Tribology International 82 (2015) 311-318]

Scales – Molecular Dynamics

- Interaction of contact loads with defects in the structure of the aluminum slab – crystal structures

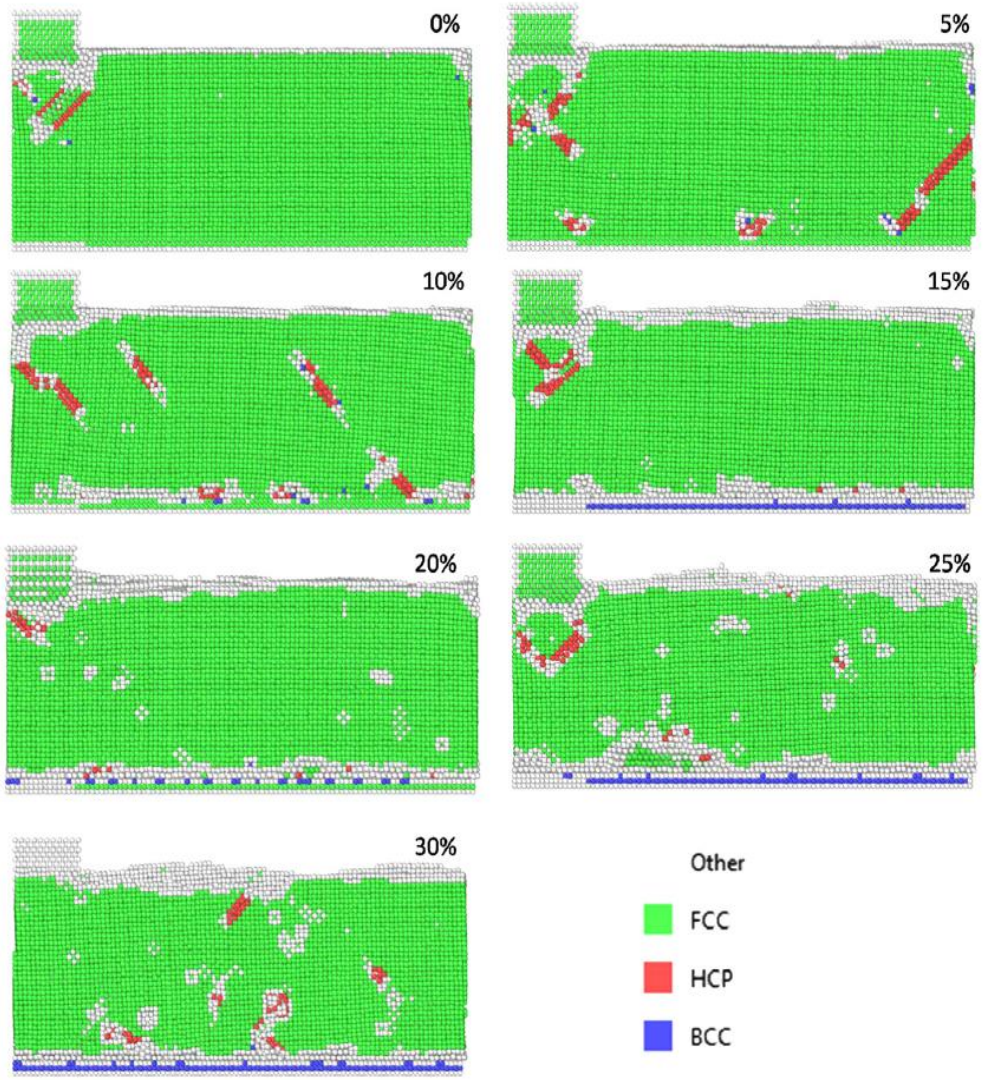

[Bortoleto *et al*., Tribology International 82 (2015)]

roberto.souza@poli.usp.br

Real time monitoring and control of friction stir welding process using multiple sensors

https://doi.org/10.1016/j.cirpj.2020.03.004

FSW - Friction Stir Welding

Um novo esquema de monitoramento e controle remoto e em tempo real baseado em nuvem foi desenvolvido para um processo de fabricação denominado soldagem por fricção e agitação (FSW) para evitar a ocorrência de defeitos de solda. Este modelo adquire dados de vários sensores associados à máquina FSW e os transmite para a nuvem. Os sinais são analisados e processados na nuvem em tempo real por meio de várias técnicas de processamento de sinais e aprendizado de máquina. O modelo fornece um feedback para a máquina em relação aos parâmetros controlados desejados para obter uma qualidade de solda aprimorada. Este é um exemplo da Indústria 4.0 onde um processo de manufatura pode ser controlado em tempo real de qualquer local.

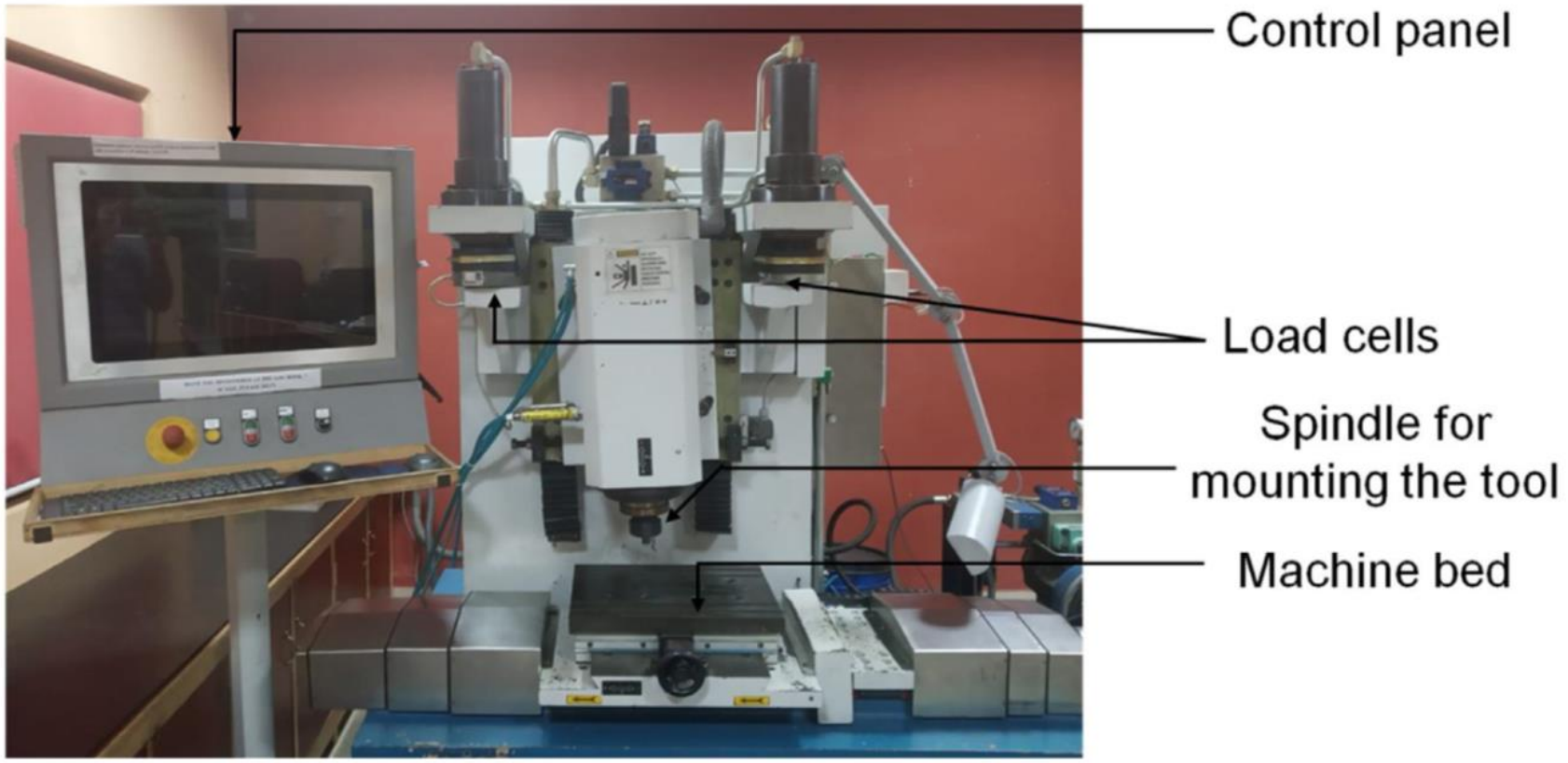

Fig. 1. FSW machine.

D. Mishra et al. / CIRP Journal of Manufacturing Science and Technology 30 (2020) 1–11

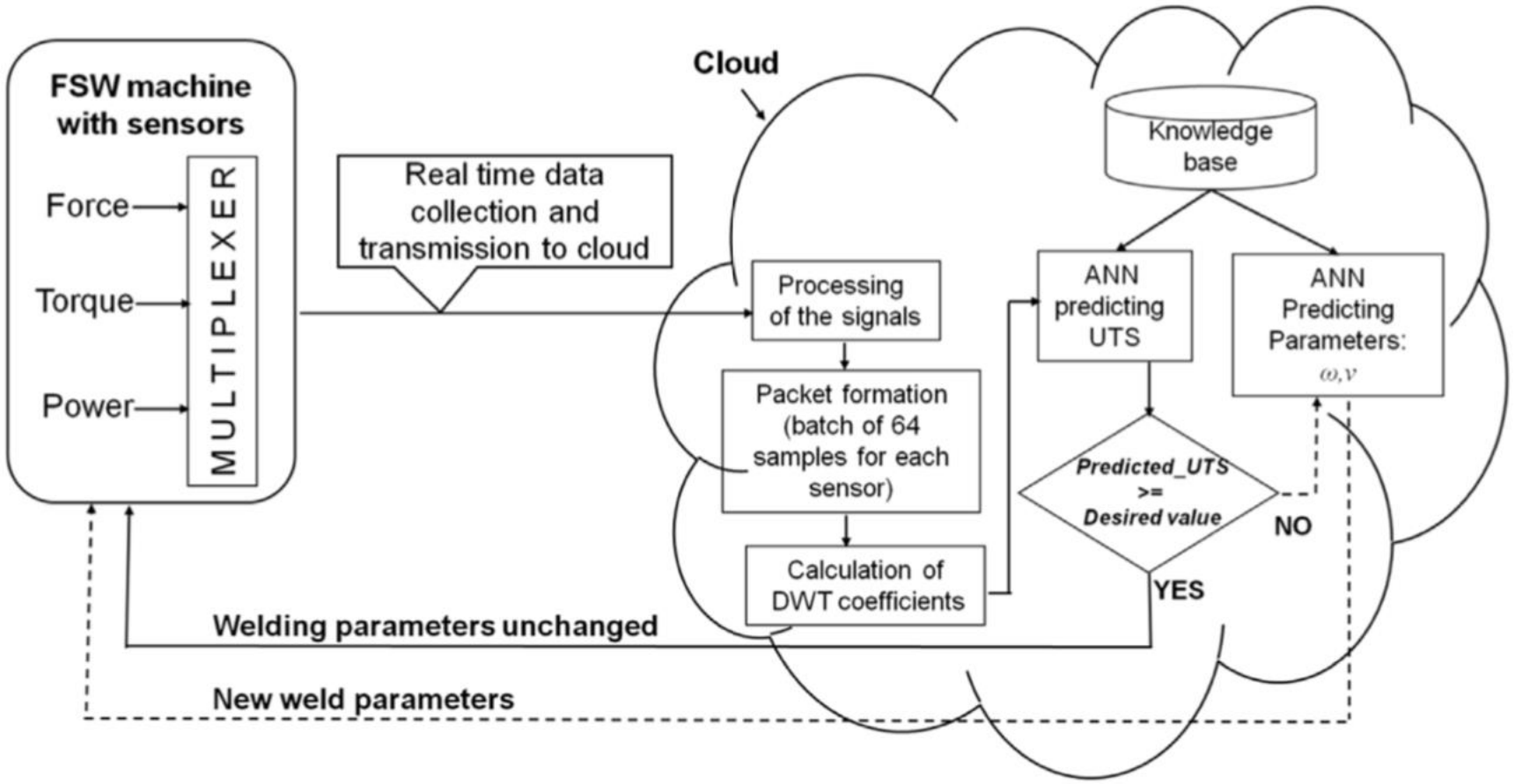

Fig. 3. Diagram of the multi-sensor model.

D. Mishra et al. / CIRP Journal of Manufacturing Science and Technology 30 (2020) 1–11

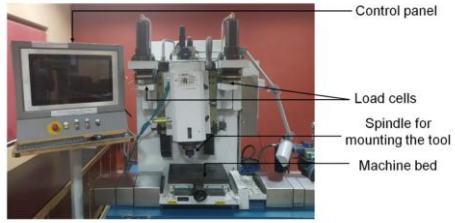

Fig. 1. FSW machine.

Dados de força e o torque são adquiridos usando uma célula de carga pré-instalada na máquina FSW, e o sensor de potência foi conectado externamente e integrado uma interface.

A taxa de aquisição de dados dos sensores de força e torque é de 10 Hz. Para haver sincronização entre as informações adquiridas usando sensores de força, torque e potência, os dados do sensor de potência também foram adquiridos a uma taxa de 10 Hz usando um cartão de aquisição de dados (NI 6211).

Um multiplexador 4: 1 controlado por tempo é criado na GUI com entradas como: valor do marcador, força, torque e dados de potência, e a saída deste multiplexador é conectada como entrada para o bloco de gravação TCP. O marcador é enviado como uma indicação antes da chegada de cada lote de dados. Todo o processo de soldagem foi monitorado remotamente.

D. Mishra et al. / CIRP Journal of Manufacturing Science and Technology 30 (2020) 1–11

Table 1
Process parameters.

ω (rpm)	600, 800, 1000, 1400, 1800, 2200, and 2600
v (mm/min)	40, 50, 60, 80, 100, 150, and 200

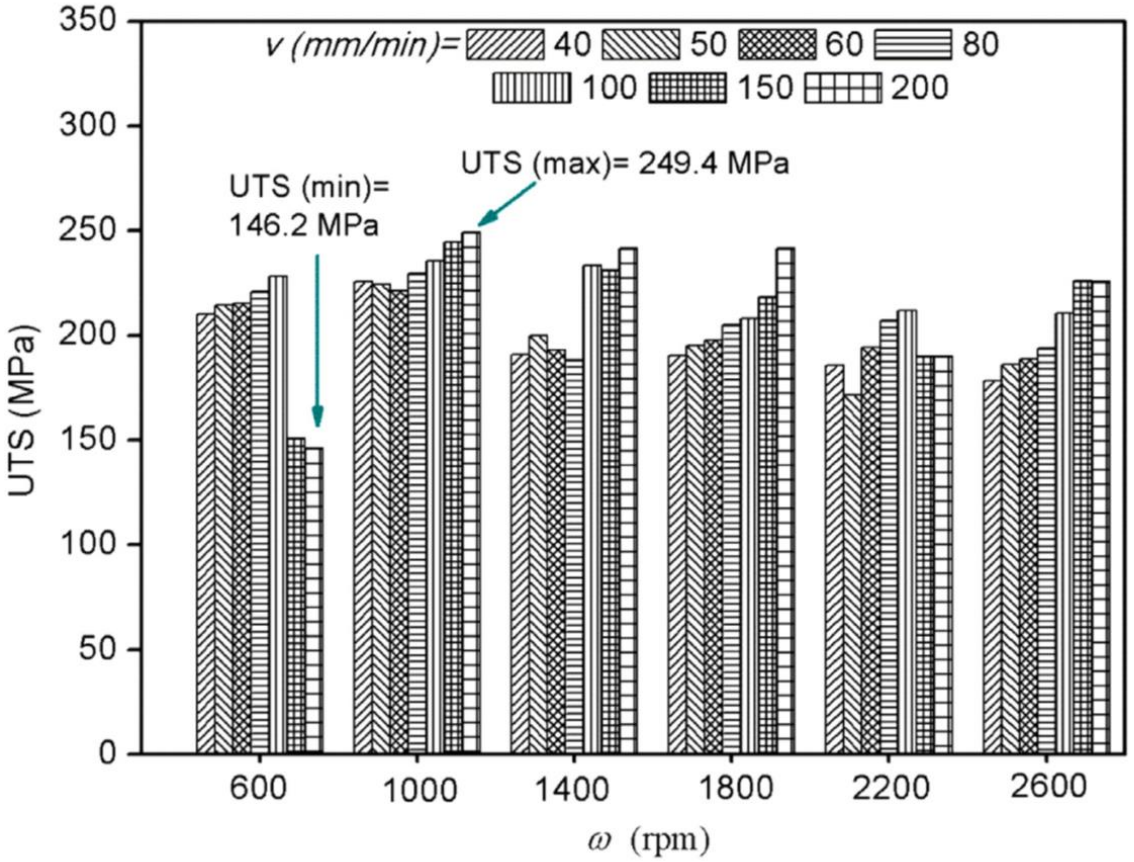

Fig. 2. UTS values of the welds fabricated with opted parametric combinations.

D. Mishra et al. / CIRP Journal of Manufacturing Science and Technology 30 (2020) 1–11

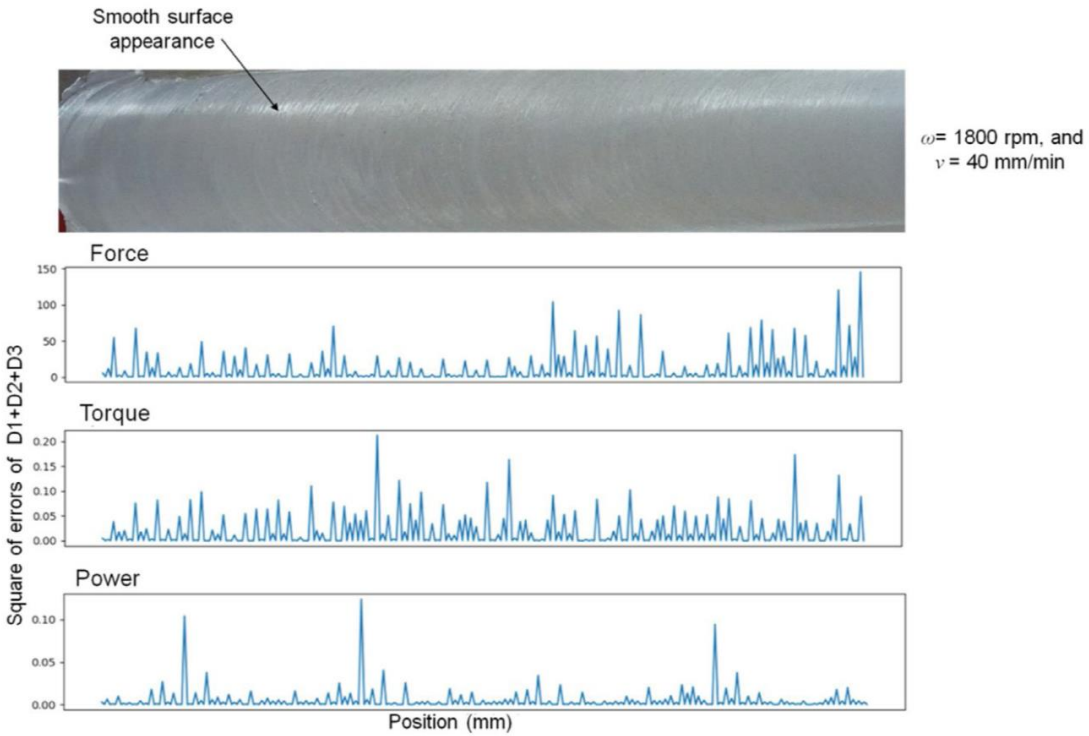

Fig. 6. Plot of detail coefficients extracted from the signals mapped with defect-free weld.

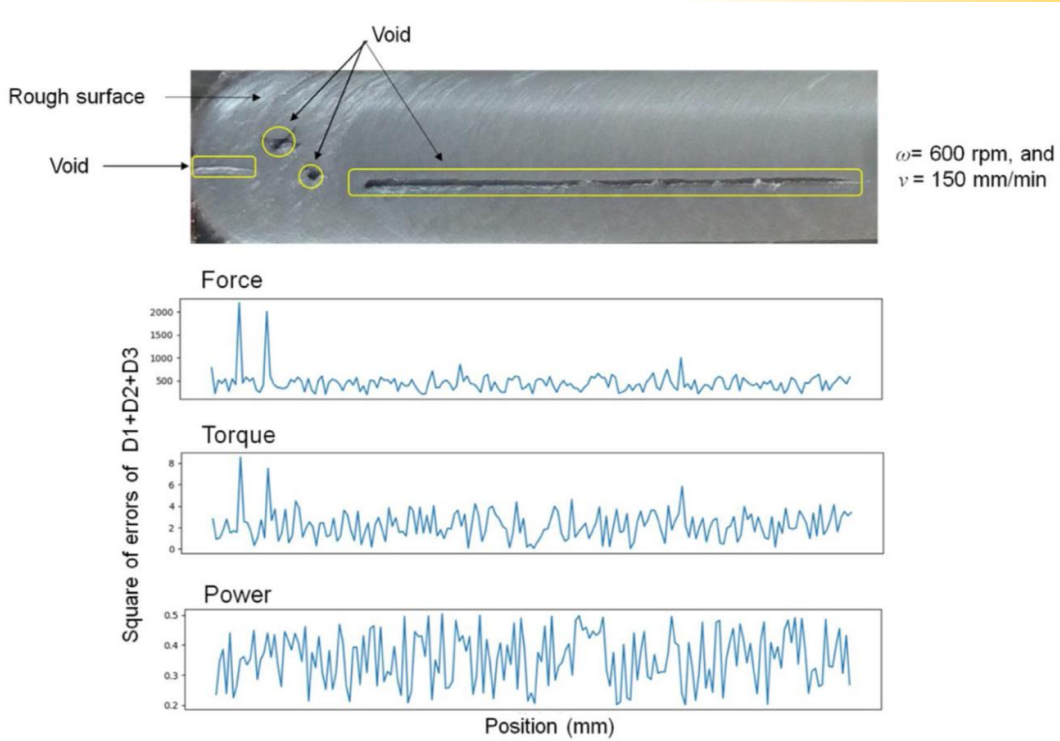

Fig. 5. Plot of detail coefficients extracted from the signals mapped with a defective weld.

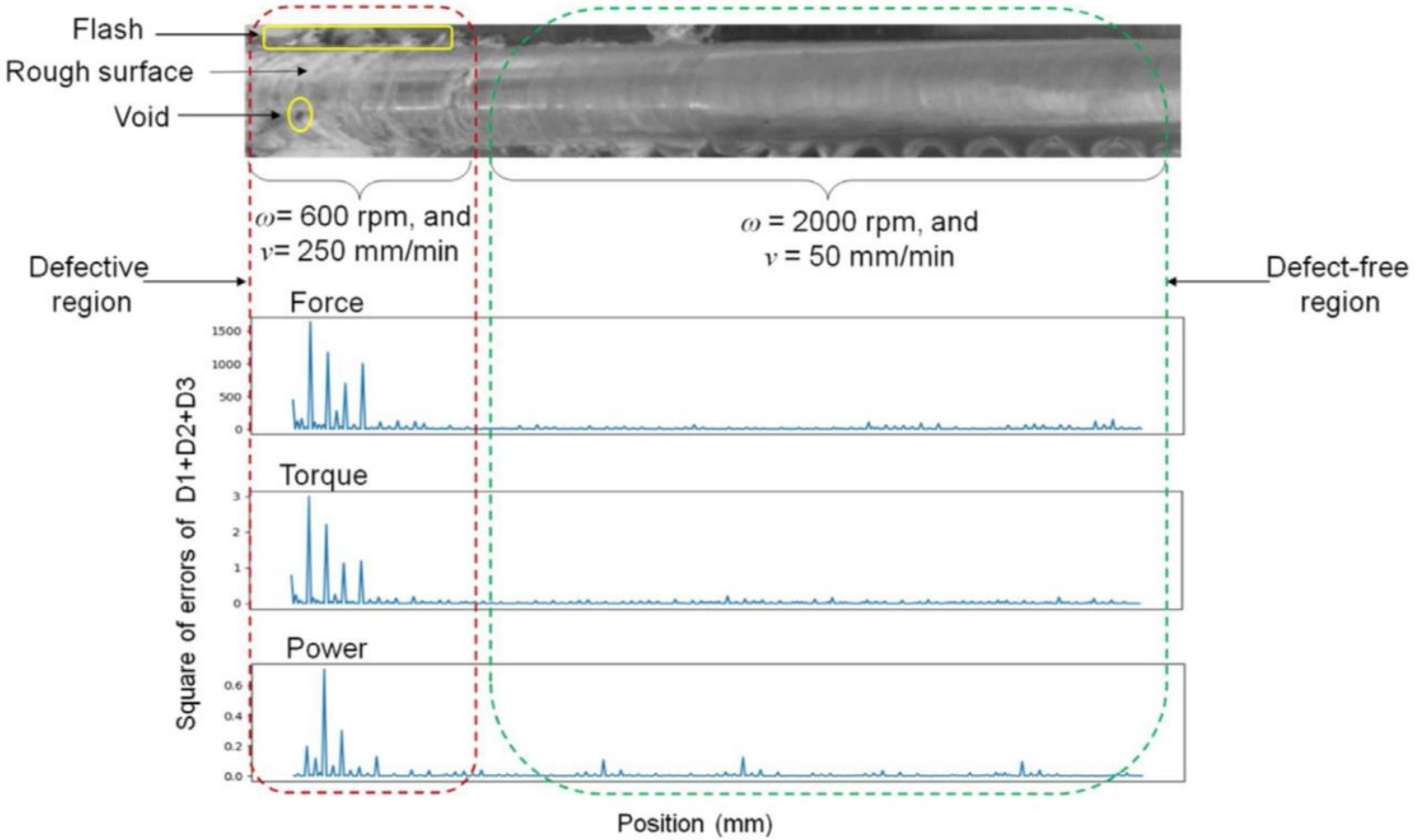

Fig. 4. Plot of detail coefficients extracted from the signals mapped with weld image having defective and defect-free regions.

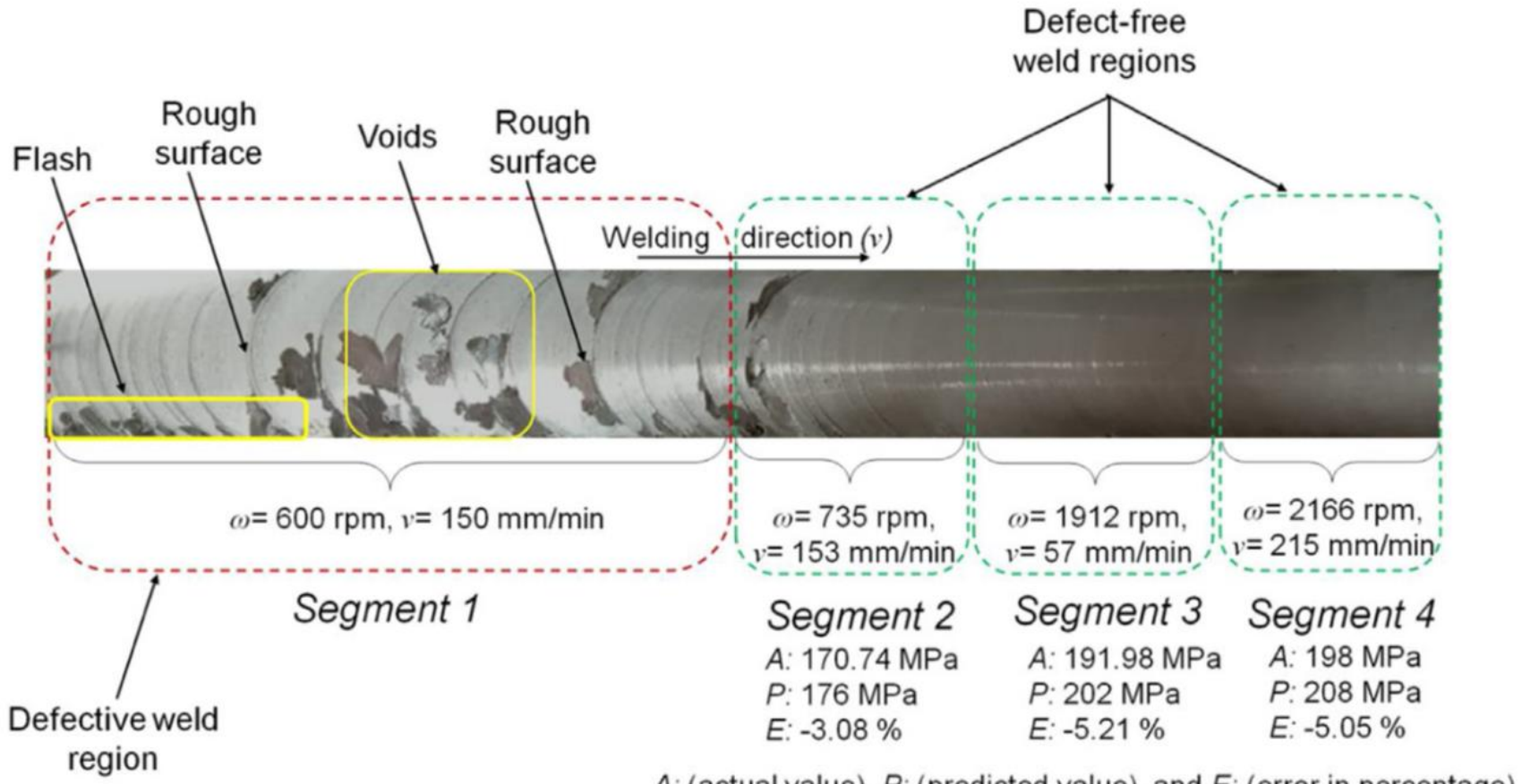

Fig. 11. Real time control of defects during welding with improper parametric combination.

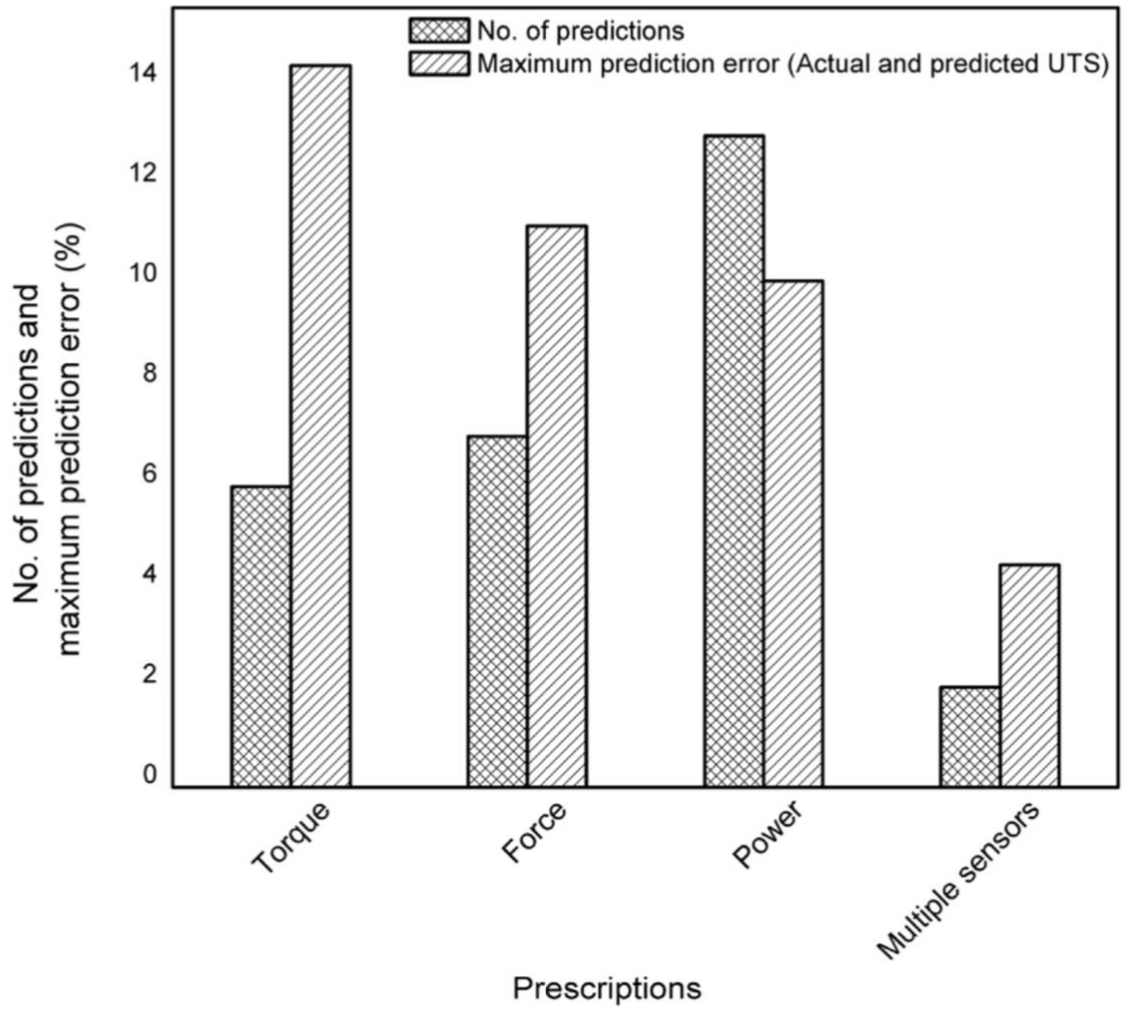

Fig. 15. Effect of multiple sensors over single sensor.

Conclusões

Uma nova técnica para monitoramento e controle remoto e em tempo real do processo FSW usando vários sensores foi apresentada neste artigo.

A técnica envolve computação em nuvem, o que torna o processo de controle mais eficiente, confiável e econômico.

Vários sensores foram utilizados e os resultados foram avaliados de forma única ou em conjunto. No futuro, outros sensores, como temperatura e vibração, podem ser considerados para extrair mais informações para controlar ainda mais o processo de soldagem FSW

Acknowledgments

Dr Newton Kiyoshi Fukumasu

Dr Vanessa Seriacopi

Prof. Roberto Martins de Souza

LFS - USP

CAPES, CNPq, FAPESP, Petrobras and Gerdau and BNDES (FUNTEC)

UC Davis - Prof. Castro